DEVELOPMENT OF MULTI-FUNCTIONAL STRUCTURES FOR SMALL SATELLITES

A Dissertation
Presented to
The Academic Faculty

By

Terry Stevenson

In Partial Fulfillment
of the Requirements for the Degree
Doctor of Philosophy in the
School of Aerospace Engineering

Georgia Institute of Technology

December 2018

DEVELOPMENT OF MULTI-FUNCTIONAL STRUCTURES FOR SMALL SATELLITES

Approved by:

Dr. Glenn Lightsey, Advisor
School of Aerospace Engineering
Georgia Institute of Technology

Dr. Brian Gunter
School of Aerospace Engineering
Georgia Institute of Technology

Dr. Claudio Di Leo
School of Aerospace Engineering
Georgia Institute of Technology

Mr. John Baker
Planetary Smallsat Office
Jet Propulsion Laboratory

Dr. Matthew Sorgenfrei
Intelligent Systems Division
NASA Ames Research Center

Date Approved: December 1, 2018

ACKNOWLEDGEMENTS

While this dissertation represents the culmination of my graduate research, there are many others who deserve a large share of the credit for making this work possible. First, I would like to thank Dr. Glenn Lightsey for being the best advisor and mentor a grad student could ask for. From the very beginning of my graduate studies you've trusted me with a shocking amount of expensive hardware, given me the freedom to pursue my research interests, and supplied the guidance to keep that pursuit on track.

I would also like to thank my undergraduate research advisors, Dr. Lori Magruder and Dr. Amy Neuenschwander, for giving me my first real exposure to research. I wouldn't be where I am now without the experience and guidance you gave me, although I probably do still use too many commas.

This work would also not have been possible without the constant support of Matt Sorgenfrei, who shepherded me through the long and at times arduous BioSentinel thruster project. Special thanks also go to Dayne Kemp for his invaluable assistance with the thruster's electronics.

Thanks also go to the Cupid's Arrow team: John Baker, Christophe Sotin, Tony Freeman, and many others. It was a pleasure working with you on such an interesting project, and I hope our paths cross again on future projects.

Grad school would have been a dull place without the other students of the Space Systems Design Lab and the Lightsey Research Group: Andrew Fear, Parker Francis, Byron Davis, Chris McBryde, Jason Swenson, Thomas Choi, Tanish Himani, Matt Wilk, Swapnil Pujari, Kip Hart, Alex Long, Julian Brew, and so many more. I will also be forever grateful to my former colleagues from UT Austin, Henri Kjellberg and Travis Imken, who taught me everything I know about CubeSats.

Last but not least, I would like to thank my family for their constant love and support throughout this journey, I could not have done it without you.

TABLE OF CONTENTS

LIST OF TABLES

LIST OF FIGURES

SUMMARY

Improvements in miniature electronics have allowed CubeSats and other small satellites to perform increasingly complex missions. In contrast to typical space missions, many small satellites are more limited by available volume than by mass, since they must fit into small deployment pods. This available volume can be used more efficiently by taking advantage of advanced manufacturing techniques, particularly 3D printing. Hollow elements can be printed into the structure that can be used to store and transport fluid. In this way, the structure of the satellite can become multifunctional; it still provides structural support, but can also encompass fluid handling systems, such as cold gas thrusters.

This concept was applied to produce a propulsion system for an interplanetary 6U CubeSat called BioSentinel. By printing the thruster from a ceramic-like material, the propellant tanks are able to fill more of the available volume than would have been possible with conventionally produced parts. Incorporating the nozzles and piping into the structure also reduces the number of pressure seals required. The BioSentinel thruster has been manufactured and tested, and will launch with the first flight of the Space Launch System in 2020. This technology was also applied to design a CubeSat structure that is entirely 3D printed, and incorporates a propulsion system into a metal structure. This improves the maneuverability of the spacecraft while also increasing volume efficiency, and allows the nozzle geometry to be optimized for specific missions. Finally, these techniques were applied to design a printed structure for a Venus atmospheric sampling probe called Cupid's Arrow. The probe has an integrated propulsion system and a separate fluid path for collecting and storing atmospheric gas samples. This development of multifunctional structures improves the state of the art in small satellite design and enables more volumetrically efficient space missions.

CHAPTER 1
INTRODUCTION

In the past ten years, small satellite capabilities have grown considerably, from nonmaneuvering Earth orbiting satellites to spacecraft capable of precision formation flying [1], interplanetary missions [2], and large scale constellations [3]. These advances were enabled in part by the miniaturization of electronics, which has allowed subsystems such as flight computers and radios to fit within these small satellites. However, CubeSats and other small spacecraft are still severely volume constrained, since they must launch as secondary payloads within prescribed physical limits. In many cases, these missions are limited more by their volume constraints than by mass constraints, in contrast to primary payloads, which are typically more constrained by mass limits.

1.1 CubeSats

A CubeSat is a popular type of small satellite originally developed at Cal Poly and Stanford. The most basic CubeSat size is called "1U" and is approximately 10 x 10 x 10 cm. CubeSats can be made in larger sizes, such as the common 3U size (roughly 10 x 10 x 34 cm), 6U, 12U, and even larger. The greatest advantage of CubeSats is the existence of standardized, compact deployment systems, such as the P-POD[4], ISIPOD[5], and others. The deployment scheme has been largely standardized between the different commercially-available deployers, with minor modifications needed for some[6]. Thanks to this standardization, a satellite need only conform to the CubeSat spec to be compatible with a large number of secondary payload opportunities, which greatly simplifies launch planning. To date, all CubeSats have been launched as secondary payloads, sharing the launch vehicle with other satellites.

With two exceptions, all CubeSats launched to date have remained in Earth orbit, which

has many advantages for spacecraft design. Aside from the Van Allen belts, the radiation environment is less severe than in interplanetary space, since the Earth's magnetic field shields spacecraft from cosmic rays and solar wind ions. The magnetic field also offers the potential for magnetically actuated attitude control by using the interaction of onboard electromagnets and the Earth's magnetic field to produce torque. Communications and mission operation are also simplified, since radios can use lower transmission power and higher data rates due to the shorter distances involved. CubeSats have been extensively proven in Earth orbit, with 294 launches in 2017 alone[7], and there is increasing interest in expanding their range beyond LEO. In 2018, two 6U CubeSats were launched as secondary payloads with the InSight Mars lander [2]. The CubeSats, called MarCO A and MarCO B, will provide a telemetry relay to Earth for InSight during its entry into the Martian atmosphere. In addition to MarCO, there are plans for 13 CubeSats to launch on the first flight of the Space Launch System, called EM-1 [8]. These satellites will be sent on different trajectories, some will orbit the Moon and others will be sent into interplanetary space. Carrying CubeSats as secondary payloads is likely to become more common among planetary science missions, and plans are already developing for secondary payloads to be carried aboard Europa Clipper [9].

1.1.1 Volume Limitations

Every spacecraft deployment scheme, from CubeSat rail pods to launch vehicle fairings, specifies a maximum allowable mass and volume of the payload. This can be used to calculate an average payload maximum density. This is not the density of any particular component of the spacecraft, but rather it is a representation of how compact the spacecraft must be in order to fit into the deployer. A satellite in a low density deployer can have features such as booms and fixed dish antennas that greatly increase the volume envelope of the satellite without greatly increasing the mass. A satellite in a high density deployer, however, will typically need to conform closely to the maximum volume enve-

Table 1.1: Payload volume and mass restrictions for a range of deployer sizes. CubeSat deployers given for NanoRacks and Planetary Systems Corp, ESPA ring uses standard 15" adapter, and Falcon 9 uses 5.2m fairing with in Full Thrust expendable mode.

	Nanoracks[10]	3U-PSC[6]	6U-PSC[6]	ESPA[11]	Falcon 9[12]
Volume (L)	3.41	4.80	10.15	418.5	145043
Mass (kg)	6.0	6.0	12	180	22800
Density (kg/L)	1.76	1.25	1.18	0.43	0.157

lope to fully utilize the allocated mass. Table 1.1 shows five representative deployer options for spacecraft: 3U CubeSats from NanoRacks and Planetary Systems pods, 6U CubeSats from Planetary Systems, attaching to an ESPA ring via Lightband, and flying as the primary payload of a Falcon 9 Full Thrust.

There is a clear trend of decreasing payload density with increasing payload mass; a 3U CubeSat has less than one tenth of the volume per allowed kilogram compared to a Falcon 9 primary payload. Because of this, small satellites (and CubeSats in particular) are typically more restricted by their volume limit than by their mass limit. While traditional spacecraft engineering focuses on making the vehicle as lightweight as possible, small satellites often struggle to be as compact as possible.

The volume restrictions given in the table are all for spacecraft deployed into low Earth orbit. This is the most accessible region of space, and requires the lowest amount of energy per unit mass to reach. Higher energy trajectories, such as geostationary orbit or interplanetary trajectories, have correspondingly tighter mass restrictions. For example, a Falcon 9 can deliver 22,800 kg to LEO, but can only deliver 8,300 kg to a geostationary transfer orbit (GTO) [12]. Since the payload fairing is the same size for a GTO and LEO launch, the volume restriction will be similar. Due to the very small number of CubeSats launched beyond LEO, there is currently no published standard for CubeSat mass restrictions for interplanetary trajectories. However, given the tighter mass restrictions faced by the primary payloads, it is likely that future interplanetary CubeSats will not only have to conform to the tight volume restrictions of the CubeSat spec, but will face more restrictive mass limits as well. This could potentially reverse the importance of the mass and volume limits

compared to LEO CubeSats, making the mass limits more restrictive. Any technology that can increase the compactness and reduce the mass of a subsystem is especially beneficial to these missions.

1.1.2 Miniature Electronics

The rise of small satellites has been enabled in part by improvements in consumer electronics, specifically in the miniaturized systems found in modern smartphones and laptops. Consumer demand is constantly driving these devices to consume less power, fit in smaller form factors, and have more capabilities, all of which are also desirable qualities for satellite electronics. Planet, a prolific operator of Earth-imaging CubeSats, has designed its 'Dove' satellites using primarily commercial off-the-shelf components (COTS), rather than space-grade electronics[3]. This was based on cost and performance, as the consumer electronics were found to be as reliable as systems designed and advertised for CubeSats, while being much less expensive. While consumer electronics hardware cannot provide the radiation tolerance or reliability needed for interplanetary or long-duration GEO missions, the Dove satellites have short enough orbit lifetimes that electronics failures have not been a significant issue [3]. With the increase in interest in small satellite missions beyond Earth orbit, new miniature electronics are being developed with improved radiation tolerance and higher reliability. The Sphinx CDH and Iris radio[13] are currently in interplanetary space aboard the MarCO CubeSats, and will be used on future deep space CubeSats.

1.1.3 Propulsion

Many miniature propulsion systems have been demonstrated on CubeSats, starting not long after the introduction of the CubeSat standard [14]. However, despite these technology demonstrations, small satellite propulsion has not yet become widespread. This is partly because most small satellites do not require propulsion. One important role of propulsion on larger spacecraft is for attitude control, but in low Earth orbit this can be achieved with

reaction wheels and magnetic torque rods. This configuration has the advantage of requiring no consumables, so it can be performed as long as the solar panels are functional. Propulsion systems can also be used for stationkeeping, relative maneuvering, or orbit reboosting, but these are also not commonly required by small satellites. Proximity operation demonstrations have been done by small satellites [1], and many concepts exist for larger formations of CubeSats [15, 16], but none have been implemented to date. Orbit reboost is also not typically needed on CubeSats, since their electronics are not designed to survive much longer than the orbital decay time.

However, the growing number of proposed interplanetary CubeSat missions and large scale small satellite formations are driving a need for more capable CubeSat propulsion systems. Interplanetary satellites cannot use magnetic torque rods for attitude control, and typically require propulsive ACS to unload momentum from their reaction wheels. Proximity operations, such as small inspector satellites, require even more maneuverability. If a satellite is required to point an instrument, such as an inspection camera, at a target while maneuvering around that target, it will likely require six independently controllable degrees of freedom (three rotational and three translational). Creating a propulsion system that can deliver this level of control in a CubeSat's small available volume is a challenge with traditional manufacturing techniques.

1.2 Additive Manufacturing

At the same time that miniaturized electronics have been improving the capabilities of small satellites, manufacturing techniques have also been improving, particularly 3D printing. 3D printing is a process developed largely in the past three decades, in which a part is built up layer by layer rather than machined away from a billet. The printing technology has improved such that it is no longer used simply to make plastic models; fully dense printed metal parts can now be made commercially. The part quality has also improved to the point that printed components are regularly used in final applications, rather than

just for prototyping or mold-making. This shift from flimsy prototypes to strong, end-user parts is reflected in a terminology shift: 3D printing was originally referred to as "rapid prototyping", and is now more commonly called "additive manufacturing".

Metal printing is especially useful for spacecraft components, since it allows the manufacture of strong structural components that can withstand the vacuum, extreme temperatures, and radiation of outer space. Metal printing allows a structure to be optimized in a way that would not have previously been practical, which saves precious mass by allowing the structure to be lighter for the same strength. It can also reduce the total part count of a system. For example, a partially or mostly-enclosed volume, with openings smaller than its internal cross section (for example, a pressure vessel) would typically be machined or rolled in multiple pieces and then welded or bolted together. The welds introduce possible defects that could weaken the structure, and bolting the pieces together requires additional space and mass for a gasket seal. A 3D printer could potentially produce the same part in a single continuous piece. Lowering part counts also simplifies integration, which reduces technician time, saving money and shortening the schedule.

1.2.1 Methods

Many different additive manufacturing technologies exist, covering a wide range of materials.

1.2.1 Fused Deposition Modeling (FDM)

Fused deposition modeling is one of the earliest 3D printing technologies, and is still widely used for prototyping and even some end-use parts. An FDM machine has an extrusion head capable of three axis travel, with a heating element fed from a filament spool that can precisely lay down melted material as it moves. The extruder head scans over the build area and deposits material corresponding to one z "slice" of the part, then moves up to the next layer and repeats the process. FDM printers are most commonly used for thermoplastics

like ABS, since they can be melted at relatively low temperatures, although it can be used with any material capable of being fused onto itself, even foods like chocolate.

1.2.1 Stereolithography (SLA)

Stereolithography builds a part from a photopolymer that is cured into a solid by an ultraviolet laser. A build plate is lowered a small depth into a vat of liquid photopolymer, and a wiper runs over the surface to ensure the plate is covered in a thin, uniform layer of the liquid. The UV laser scans over the build plate, curing the photopolymer along the scan path into a thin solid layer. The build plate is then lowered further into the vat, covering the cured layer in more resin, and the laser makes another scan to build the next layer [17, 18]. This process typically has higher scan speeds and can be run at higher resolutions than FDM, since a laser can be scanned quickly enough that the curing time of the photopolymer is the limiting factor, not the mechanical motion of an extruder head. The resolution in the horizontal axes is limited by the focusing spot size of the laser, and in the vertical direction by the depth increment of the build plate. Vertical resolution is typically smaller than horizontal resolution, since the build plate depth can be controlled very precisely. SLA is typically more expensive than FDM, due to the high cost of the scanning laser and the cost of the photopolymer. A wide variety of photopolymers have been developed for the SLA process with a range of material characteristics, from quasi-ceramic materials with high tensile strength and low elongation to break; to flexible thermoplastic-like materials. An example SLA machine is the ProX 800, with a minimum spot size of 125 μm, a vertical resolution of 20 μm, and a total build volume of 65 x 75 x 55 cm.

1.2.1 Powder Bed Fusion (PBF)

The most common type of metal printing system is Powder Bed Fusion (PBF). A PBF system deposits a thin layer of finely powdered material (metal, ceramic, or plastic) onto the build surface, then uses a laser or electron beam to heat and melt a small area of the

powder, which resolidifies into solid metal [19]. The beam scans through the slice of the model for that layer, much like the SLA process, and then another powder layer is applied. There are many types of powder bed processes, one example that has been used for metallic spacecraft components is Selective Laser Melting (also called Direct Metal Laser Sintering), in which enough energy is delivered to completely melt the powder, forming a "melt pool" under the beam spot. This results in fully dense metal parts with material properties very similar to extruded or cast materials. The powder bed process can be used for a large variety of materials; some of the metals that can be printed are aluminum alloys, stainless steel, cobalt chrome, nickel alloys, Inconel, and titanium alloys. A typical laser PBF machine is the EOS M 290 [20], designed to print aluminum (AlSi10Mg), titanium, and several types of stainless steel. It has a build volume of 25 x 25 x 32.5 cm, with a focus diameter of 100 μm and z layer thickness of 20 μm. The resolution is similar to an SLA printer, since the limiting factor in both cases is the laser spot size.

1.2.1 Directed Energy Deposition (DED)

A second printing technology that can be used for metal is Directed Energy Deposition (DED). In this process, the metal powder is sprayed onto the surface of the part into the path of the beam (either laser or electron). The beam melts the area under it, as well as the powder, which builds up material in that spot [21]. DED systems do not have to build a part up from scratch, so an existing part can have new features added to it by a DED machine. If the nozzle and beam emitter are on a five axis mount, features can be added to any exterior surface of a part, allowing repairs of broken components. Parts with only some AM-enabled features could also be machined and then post-processed in the DED system.

Directed energy deposition can also use multiple powder sprayers fed from different powder hoppers, allowing the material to be blended. This can be used to produce functional graded parts, such as a bar that is stainless steel on one end, Inconel on the other, and a smooth gradient of the two in between [22]. Parts that have different materials require-

ments in different regions can have a mix of different metal alloys to tailor each area of the part to its needs, without needing to join together multiple parts of different materials.

1.2.2 3D Printing for Spacecraft

Additive manufacturing is already being used to reduce the mass of spacecraft structural components. Each kilogram of mass launched to low Earth orbit costs roughly $20,000 [23], so reductions in structural mass can lead to large cost savings. An FDM 3D printer was designed for operation in microgravity, and is currently operating aboard the International Space Station. The printer has already been used to produce tools for use by the crew, circumventing the delay of producing the parts on Earth and delivering them via resupply missions.

The Juno spacecraft carried 3D printed metal parts into interplanetary space for the first time in 2011 [24]. The spacecraft carries four printed titanium brackets used to support a waveguide. The brackets were designed in such a way that they could be produced with conventional machining, and topology optimization was not used. The brackets were printed oversized by 2 mm in all directions so that the surface roughness could be completely machined away. Additive manufacturing was chosen for these brackets for two reasons: it greatly reduced the amount of machining necessary to produce the part, and it served as a test case for metal printing for future spacecraft. The brackets were secondary structure with relatively light loads, so they provided a good stepping stone to build confidence in applying additive manufacturing to spacecraft structures.

Similar secondary structural pieces were also designed for a Surrey Satellite Technologies mission, including a star tracker mounting bracket. In this case, topology optimization was used to take full advantage of the unusual geometries that could be produced by additive manufacturing to reduce the mass of the bracket without compromising its strength. These parts underwent a detailed test and verification campaign, as did the Juno components [25]. In addition, rocket engines made by Aerojet [26] and SpaceX [27] use metal

AM to reduce weight and part count.

1.3 Contributions

The combination of increasing access to interplanetary launches for CubeSats, the availability of suitable electronics, and the tight volume constraints they must operate within has created a growing need for improvements in CubeSat structural design. Additive manufacturing offers the potential for new, previously impossible structural geometries that can be used to create more compact spacecraft.

1.3.1 Design and Testing of a Printed ACS Thruster

An attitude control propulsion system was designed, manufactured, and tested for the BioSentinel spacecraft, a 6U CubeSat built by NASA Ames Research Center. The thruster was required to fit within a thin volume on one face of the satellite, an unfavorable shape for a pressure vessel, and required seven nozzles for attitude control and limited ΔV. These volume restrictions eliminated all commercially available systems, and a custom ACS thruster had to be designed. By 3D printing the majority of the thruster from a single piece of vacuum-compatible ceramic-like material, the propellant tanks were able to fill much more of the available volume than would have been possible with conventionally produced propellant tanks. Additionally, incorporating the nozzles and piping into this printed structure reduced the number of pressure seals that had to be made, saving volume and mass as well as reducing the number of potential propellant leaks. The thruster was built as a separate module that will be integrated into the spacecraft, much like a conventional thruster. However, the efficient use of volume that arose from 3D printing the thruster serves as a test case for the design of future multifunctional structure structures that incorporate propulsion systems. A small, low cost impulse test stand was constructed to test the thruster in vacuum for average thrust and specific impulse. Over the course of the two year project, three thrusters were produced: two engineering units and one flight unit. All three were ex-

tensively tested on the stand at Georgia Tech, and one engineering unit was tested at NASA Glenn Research Center. The flight unit has been delivered, and is expected to launch with the first flight of SLS, called EM-1.

Contribution 1: The design and testing of a cold gas ACS thruster for a NASA interplanetary CubeSat using 3D printing to create a volumetrically efficient system.

1.3.2 Multifunctional CubeSat Structure

The printed propulsion system technology was then extended to develop a 3U CubeSat structure that is entirely 3D-printed from aluminum and that incorporates an ACS propulsion system. This structure is designed for a demonstration mission, called the Structural Propulsion Unit Demonstrator (SPUD), and can be applied to inspector satellites or to small satellite rendezvous and docking. The use of a multifunctional structure, providing both structural support and propulsion, allows volumetrically efficient propellant storage as well as more flexible nozzle placement. Eight nozzles are fed from a common propellant tank through pipes routed through the structural rails of the CubeSat, allowing them to be placed anywhere on the structure. The nozzles are arranged to provide six independent degrees of freedom in order to give sufficient maneuverability for inspection or docking. The use of eight nozzles to provide six degrees of freedoms means that some component of the thrust vector of some nozzles will be wasted, directed opposite some component of thrust from a different nozzle. To mitigate this loss, SPUD was optimized for a reference mission, that of an inspector satellite. A large number of reference trajectories were generated, and the nozzle angle was optimized to minimize average propellant consumption across all trajectories.

Contribution 2: Extension of the printed thruster technology to a multifunctional CubeSat structure incorporating a propulsion system.

1.3.3 Multifunctional Structure for a Planetary Probe

Finally, this technology was applied to a JPL concept study for a Venus atmospheric probe called Cupid's Arrow. The probe will be launched as a secondary payload, and will perform at least two flythroughs of the Venus atmosphere, trapping gas samples from below the homopause for analysis by a mass spectrometer. Because secondary payload opportunities are very limited for interplanetary trajectories, the probe was designed to be as compact and lightweight as possible. In order to reduce the size of the probe, the structure will be printed with an integrated propulsion system for trajectory correction and attitude control. The propellant tanks are blended into the outer support structure for the heatshield, allowing the structural mass to serve two purposes. Similar to SPUD, the propellant pipes and nozzles are built into the structure of Cupid's Arrow, giving great flexibility in nozzle placement, and reducing the number of pressure seals that must be made in the propulsion system. The structure is also used to augment the mass spectrometer by storing samples of the atmosphere within hollow spaces in the support structure for the avionics. These samples are then fed to the instrument once the spacecraft is outside of the atmosphere. The use of these hollow spaces roughly triples the amount of gas that can be stored in a single pass, which will allow a better characterization of the noise level of the instrument. The use of a multifunctional structure in this design allows the mission to be flown in a smaller diameter, improving its changes of being selected as a secondary payload.

Contribution 3: Application of the multifunctional structure design to a Venus atmospheric probe concept to reduce the probe size and improve instrument functionality.

CHAPTER 2

DESIGN AND TESTING OF A PRINTED ACS THRUSTER

The first development of the multifunctional structure technology was the design of a small propulsion system for the NASA BioSentinel mission [28]. The majority of the thruster is a single piece of 3D-printed ceramic which takes advantage of the unusual geometries made possible by additive manufacturing to store propellant more efficiently. The propellant tanks, nozzles, and a majority of the pipes were all blended into this printed structure, reducing the number of pressure seals in the system and making it more compact. Two engineering units and one flight unit were produced between 2016 and 2018, and were tested both at Glenn Research Center and at Georgia Tech on a custom test stand. The flight unit was delivered to NASA Ames in June 2018, and is currently awaiting integration with the spacecraft. The BioSentinel thruster is currently the only 3D printed propulsion that has been designed for an interplanetary spacecraft, and when SLS launches will be the first 3D printed thruster launched beyond Earth orbit.

2.1 Cold Gas Thrusters

A cold gas thruster is a propulsion system that derives all of its energy from a propellant held under pressure [29]. There is no combustion, heating, or electromagnetic acceleration of the propellant, it is simply expanded through a nozzle. This makes cold gas thrusters relatively simple when compared to electric propulsion or combustion thrusters, but also less energetic, which limits their total impulse capability. Cold gas thrusters are an attractive option for small spacecraft for both attitude control and small ΔV maneuvers, since the lower stored energy of the thruster makes it easier to comply with secondary payload safety requirements[30].

Cold gas thrusters have been used on many CubeSat missions, beginning with the

Aerospace Corporation's MicroElectromechanical System-based Picosat Inspector (MEPSI) [31], deployed in 2006. The mission consisted of two satellites, one of which used a Xenon cold gas thruster to perform a 0.4 m/s ΔV maneuver. Since then, cold gas thrusters have been flown on several other CubeSats, including POPSAT-HIP1 [32] and CANX-4 [33]. Two identical thrusters were designed for the JPL INSPIRE CubeSats [34], which would have been the first CubeSats launched into interplanetary space, although they have not yet been manifested for a launch. The first interplanetary CubeSats, MarCO A and B, use cold gas thrusters for trajectory correction and attitude control [2].

2.2 BioSentinel

BioSentinel is a 6U CubeSat developed by NASA Ames Research Center to support future human exploration of interplanetary space by characterizing the interplanetary radiation environment and its biological effects. The spacecraft will carry living yeast cells and measure the rate of DNA double strand break events caused by radiation. DNA repair in yeast cells is similar to DNA repair in human cells, so the mission will provide useful information about the impact of deep space radiation on future human exploration missions. The spacecraft will also carry a conventional radiation sensor, developed by NASA Johnson Space Center, to collect linear energy transfer values for comparison with the biological data [35].

The spacecraft is scheduled to launch on Exploration Mission 1 (EM-1), the first flight of the Space Launch System, in 2019 or 2020. EM-1 will deploy the Orion spacecraft on a free return trajectory around the Moon, as a test of both the rocket and the capsule. The launch will also carry 13 secondary payloads, all of them 6U CubeSats, which will be deployed at multiple different points on the cruise to the Moon. BioSentinel will deploy from SLS on an Earth-escape trajectory, which will take it into an Earth-trailing heliocentric orbit where it will collect radiation data for a minimum of 6 months. For the majority of the mission, the spacecraft will be oriented with the solar panels pointed towards the Sun for

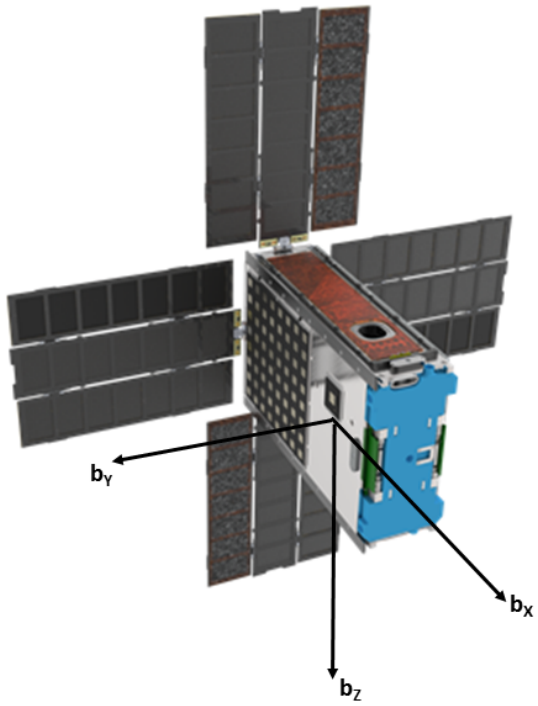

Figure 2.1: BioSentinel spacecraft with solar panels deployed. The blue object in the foreground is the 3D printed thruster.

maximum power collection, but it must rotate to point the X-band antenna towards Earth for communications.

A CAD image of the spacecraft is shown in Figure 2.1. The solar panels are shown in the deployed configuration, and the propulsion system is visible as the blue component on the +X face of the spacecraft. As a 6U CubeSat, the overall stowed size of the BioSentinel spacecraft is 36.6 x 23.9 x 11.6 cm. The yeast support module occupies roughly 4U, or about 20 x 20 x 10 cm, leaving only one third of the spacecraft volume for the bus subsystems, including the power supply, flight computer, Iris radio, and attitude control system. Three reaction wheels built into the XACT attitude determination and control (ADCS) module will be used for general pointing maneuvers, such as reorienting the spacecraft to point the antennas towards Earth or the solar panels towards the Sun. The reaction wheels will also be used to counteract the constant disturbance torque caused by solar radiation pressure. This will cause momentum to accumulate in the wheels, and every three days the

thruster will be used to unload this momentum to prevent saturation. In addition, the initial rate-reduction maneuver (called detumble) that must be performed after deployment from the launch vehicle will potentially require more momentum capability than the reaction wheels posses. The cold gas thruster will be used in both of these roles: immediately after deployment it will detumble the spacecraft, and periodically throughout the mission it will be used to unload momentum from the reaction wheels [36].

2.3 Requirements

A set of Level 4 (subsystem) requirements was developed by the BioSentinel project for the thruster. A selection of a few key requirements is shown in Table 2.1, all requirements are shown in Appendix A.

Table 2.1: Selected level 4 requirements for the BioSentinel thruster.

Requirement	Title	Description
Prop-2	Subsystem Mass	The Freeflyer propulsion system shall not exceed a total mass of 1.4 kg.
Prop-3	Subsystem Volume	The Freeflyer propulsion system shall not exceed a total volume envelope of 235 mm x 110 mm x 40.25 mm. The main body of the Freeflyer propulsion system shall have a maximum z-axis dimension of 210 mm.
Prop-7	Operating Pressure	The Freeflyer propulsion system maximum operating pressure shall be less than 690 kPa.
Prop-18	Storage Life	The Freeflyer propulsion system shall be designed for 8 months of storage in the loaded and pressurized configuration without greater than 10% loss of propellant mass.
Prop-22	Total Impulse	The Freeflyer propulsion system shall provide a total impulse over the life of the mission of at least 36 N-sec.

The first two requirements in Table 2.1 give mass and volume limits for the thruster. Of these, the volume limit was by far the most restrictive. The final design has a total fueled mass of 1285 grams, comfortably under the mass limit, but uses the entire allocated volume. This restrictive envelope required the thruster to make efficient use of the available

volume. Volumetric efficiency is a major strength of the printed thruster technology, and was the main reason such a system was chosen for this spacecraft. The volume limit as stated in the requirement does not capture the full complexity of the volume limitations, since it references a "main body" dimension separate from the maximum extents. This is because the thruster was able to occupy a non-rectangular volume, and extended into small available spaces where possible. These small spaces were considered to be outside the "main body" of the thruster, but still within the maximum extents. In practice, a CAD envelope was used to keep track of the thruster volume throughout the design process, and this requirement was rarely referenced.

Prop-7 was levied due to the secondary payload safety requirements [30], and was intended to allow the thruster to fly as a "sealed container". Such systems must be pressurized under 100 psia (690 kPa), but are only required to conduct finite element analysis to 2.5 times the maximum expected operating pressure (MEOP). Systems with greater internal pressure are classified as "pressure vessels" and are subject to more stringent fracture control requirements, including a proof pressure test of the flight unit to 1.5 times MEOP. Final clarification of the status of the thruster has not yet been received from the SLS safety board, but the proof test was conducted on the flight unit in the case that it is reclassified as a pressure vessel.

Prop-18 arose from the expected storage time of the spacecraft between final filling and launch. This requirements sets the maximum allowable leak rate of 3.5 mg/hour. Finally, Prop-22 comes from the BioSentinel ADCS simulation, and is the sum of the detumble maneuver and all expected desaturation maneuvers.

2.4 Propellant Selection

Early in the design process, it became clear that the volume limitations placed on the BioSentinel thruster were more constraining than the mass limit, so the thruster must be able to utilize the available volume as efficiently as possible. Because of this, volumetric

efficiency was an important factor in propellant selection. The most common measure of a propulsion system's propellant efficiency is the specific impulse, which is the exhaust velocity normalized by standard Earth sea level gravity (9.81 m/s^2. Specific impulse can be used to obtain the impulse capability per unit of propellant mass. However, specific impulse is a mass-basis efficiency. Since the BioSentinel thruster is more constrained by volume than by mass, a new parameter was defined to capture the performance of a propellant on a volumetric basis, rather than a mass basis. This parameter is called volumetric impulse (I_{vol}), and is defined with:

$$I_{vol} = \frac{J}{V_p} \tag{2.1}$$

where I_{vol} is the volumetric impulse, J is the impulse delivered, and V_p is the volume of propellant consumed in delivering that impulse. Volumetric impulse can also be stated in terms of the more familiar specific impulse:

$$I_{vol} = gI_{sp}\rho \tag{2.2}$$

where g is the standard acceleration due to gravity [9.81 m/s^2] I_{sp} is the specific impulse, and ρ is the mass density of the propellant. Clearly volumetric impulse will be high for propellants with high storage densities and high specific impulse. However, those two properties are often inversely related. Table 2.2 shows seven of the propellants that were considered for the BioSentinel thruster, sorted by molecular weight.

The propellant densities are given at the BioSentinel maximum operating temperature of 50°C, since the tanks must be sized for the minimum propellant density expected. Three of the propellants are not saturated two-phase mixtures at 50°C, two of them (SF_6 and CO_2) are supercritical, and one (Nitrogen) is a gas. All three of the exceptions were computed using 10 MPa max pressure. The specific impulse was calculated assuming a tank temperature of 25°C and a nozzle area ratio of 204 (the design nozzle area ration) exhausting into a perfect vacuum.

Table 2.2: Volumetric efficiency of potential propellants. Densities are of liquid at 50°C under saturation conditions, except Nitrogen (†), which uses vapor density at 10 MPa; and SF_6 and CO_2 (*), which use supercritical density at 10 MPa.

Name	M [g/mol]	I_{sp}[s]	ρ [kg/m^3]	I_{vol} [N-s/L]
R-236fa [37]	152.04	46.9	1270	584.1
SF_6[38][39]	146.06	47.6	1109.5*	517.9
R-134a [40]	102.03	49.3	1102.3	532.9
Butane [41]	58.12	73.1	542.34	388.8
CO_2 [42]	44.01	67.6	384.33*	254.8
Ammonia [43]	17.03	106.7	562.9	589.0
Nitrogen [44]	14	77.6	102.5†	78.0

There is a general trend apparent in the table of increasing I_{sp} and decreasing density as molecular mass decreases. The heavy fluorinated gases have poor I_{sp} due to their high molecular weight, but high storage density gives them good volumetric impulse. At the other end of the scale, Nitrogen has a good I_{sp}, but the inability to store Nitrogen as a saturated liquid gives it poor storage density. The largest outlier in this trend is ammonia, which has both an unusually high I_{sp} and liquid density, which combine to give it the highest I_{vol} of all candidate propellants. Interestingly, water has an I_{sp} of 102.7 s and a liquid density of 990 kg/m^3 at 50°C, which greatly exceeds even ammonia in volumetric impulse, although its low vapor pressure would give it impractically low thrust. Ammonia was ultimately rejected over safety concerns; it is toxic above 50 ppm and would have required extensive gas recovery and handling safety procedures to be used in a university lab. With ammonia eliminated, R-236fa has the highest volumetric impulse, only slightly below ammonia. It is also non-toxic, non-flammable, commercially available, and can be stored at relatively low pressures (5.84 bar at 50°C), which simplifies the process of approval for secondary payloads.

2.4.1 Propellant Sizing

As discussed above, the BioSentinel GNC team developed a spacecraft simulation for the entire nominal and extended missions, each lasting 6 months, for a total extended spacecraft life of 12 months. The total impulse of 36 N-s specified in the Prop-22 requirement

was derived from the maximum expected impulse required for the detumble maneuver and all momentum unloading maneuvers throughout the mission, and includes margin. The primary disturbance torque on the spacecraft is solar radiation pressure, which causes momentum to accumulate in the reaction wheels that must be unloaded with the thruster.

The chosen propellant, R-236fa, has a volumetric impulse of 584.1 N-s/L, so a 36 N-s system requires only 62 cm^3 of main tank volume. The first rough design of the tanks showed that this could be easily exceeded. This would potentially allow a less volumetrically efficient propellant to be used instead of R-236fa, with a higher I_{sp} and thus lower mass. However, since the design was still well below the 1.4 kg mass limit, the decision was made to maximize the total impulse capability of the thruster, even if it greatly exceeded the requirement. This was done primarily to make the design as reusable as possible. One of the goals of the project was to develop a thruster that could be used on other 6U CubeSats, and a higher impulse capability would make the thruster more attractive to other potential missions.

The final design allows 220 grams to be stored in the main tank, providing 95.4 N-s of impulse, 265% of the requirement. Given this large margin and the risks associated with overfilling the tank, the BioSentinel flight unit will only be filled with 200 grams of the propellant, providing 86.7 N-s. This gives a roughly 10% ullage margin in the tank even at the maximum temperature of 50°C. This margin allows the filling process to be less precise (with up to 20 grams of error) without endangering the thruster. Assuming the maximum allowable leak rate of 3.5 milligrams per hour, a storage time of 8 months between final propellant loading and launch, and a maximum mission duration of 12 months (6 months nominal plus 6 months extended), the thruster will lose 51.24 grams due to leaks over the life of the mission. This leaves 148.76 grams for operations, capable of providing 64.5 N-s of impulse, still well above the 36 N-s requirement.

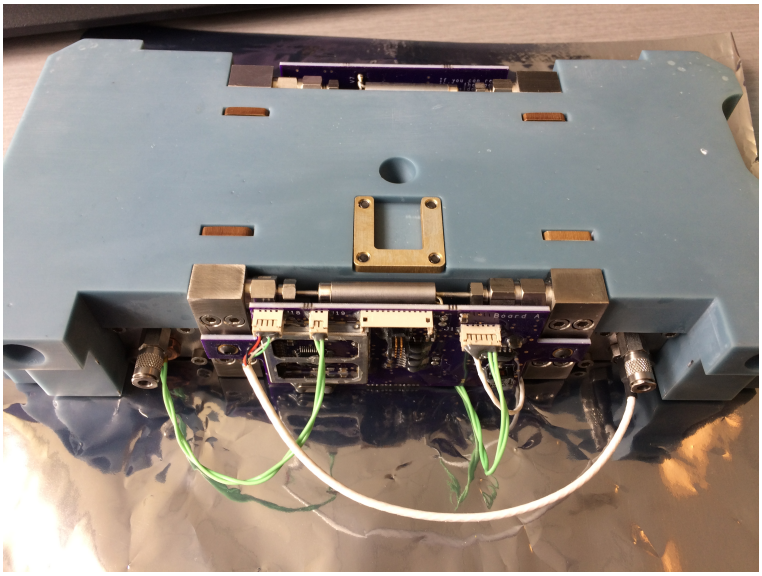

Figure 2.2: Assembled BioSentinel thruster, flight unit.

2.5 Design

In order to make efficient use of the available volume, the thruster is designed around a single piece of 3D printed material, encompassing the propellant tanks, feed pipes, nozzles, O-ring grooves, and attachment points for the spacecraft. The assembled thruster is shown in Figure 2.2. The light blue material is the 3D printed structure, and the metal pieces are stainless steel manifolds that are sealed to the structure.

The 3D printed structure was printed with a particle composite material called Bluestone [45], printed with stereolithography (SLA). Bluestone is a ceramic-like material, with a high stiffness and low elongation to break compared to other SLA materials. The deciding factor in choosing Bluestone was its large acceptable temperature range, with a heat deflection temperature of 267°C. It was printed by a ProX 800, an SLA machine with a build volume of 65 x 75 x 55 cm, and a minimum scanning resolution of 125 μm.

The printed part is hollow, with the interior volume used for the propellant tanks. The use of 3D printing to produce a hollow structure enables complex tank geometries that would not have been feasible in a machined part, which allows the thruster to utilize the allocated volume more efficiently than a machined structure. All interior volumes are open

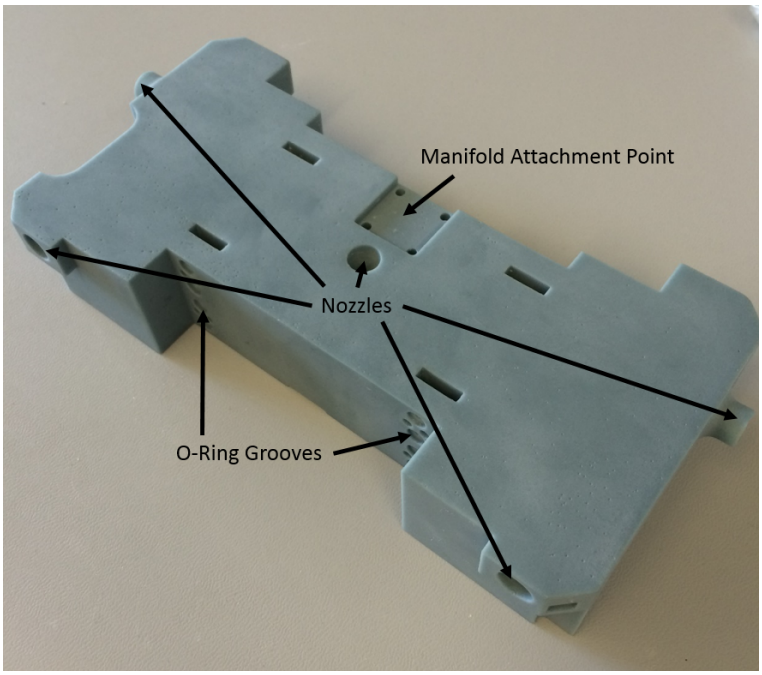

Figure 2.3: Printed structure with no attachments.

to the outside so that the uncured resin can be drained from the thruster after printing. The piece was printed at an angle, which eliminated shallow overhanging surfaces and allowed the structure to be printed without any internal support structure, which would have been impossible to remove given the limited tool access to the interior. External supports were cut and wet sanded flush, and the entire structure was thermally post-cured to improve tensile strength and temperature range. The printed structure with no attachments is shown in Figure 2.3.

Tests with Bluestone showed that it can be tapped to accept a helical insert, potentially allowing components to be screwed into the structure directly. However, in roughly one quarter of the tests, installing the inserts caused some of the internal threads to snap, unacceptably weakening the inserts. This is likely due to the brittleness of the Bluestone material, but could have been due to installation error. In addition, helical inserts cannot be easily sealed, since they have a large outer surface area. Instead of threading into the printed structure, thread sealed components such as sensors and filling valves were installed into stainless steel manifolds. These manifolds were then sealed to the printed structure with

O-rings seated in printed grooves. All manifolds were sealed via a "face seal", a method of sealing two parallel planes together around a certain location. Likewise, the eight solenoid valves were divided between two manifolds, each one face sealed onto the structure. The normal force required to seal these manifolds was provided by small nut plates inserted into the structure. Machine screws passing through printed holes compressed the structure between the nut plates and the manifold.

2.5.1 Internal Features

As discussed above, the interior of the printed structure is hollow, and is filled with propellant. The interior is separated into two propellant tanks, a "main tank" for holding the bulk of the propellant, and a "plenum" for vapor expansion. This is done because the propellant is stored as a saturated liquid-vapor mixture. If the nozzles were fed directly from this mixture, droplets of liquid could be ingested into the nozzle, causing rapid changes in density and reduced performance. Instead, the propellant is expanded into a vapor in the smaller tank, and the nozzles are fed from this tank. As the vapor is depleted it is periodically repressurized by the main tank through a refill valve. Both tanks are instrumented with pressure and temperature sensors so that the propellant state can be known at all times. A schematic tank arrangement is shown in Figure 2.4.

The size of the main tank and the maximum spacecraft temperature set the maximum propellant load of the thruster. The liquid phase of the propellant becomes less dense at higher temperatures, causing a greater portion of the tank volume to be occupied by liquid. If at any point the tank is entirely filled with liquid, any further increase in temperature will cause the propellant pressure to sharply increase, a phenomenon called hydraulic lock. With a main tank volume of 176 cm^3 and a liquid density of 1270 kg/m^3 at 50ºC [37], the maximum mass loading is 223 grams. In order to allow some margin, the propellant load of the thruster was set to 200 grams. This would theoretically allow it to reach 79ºC before experiencing hydraulic lock, although the thruster was never tested at temperatures greater

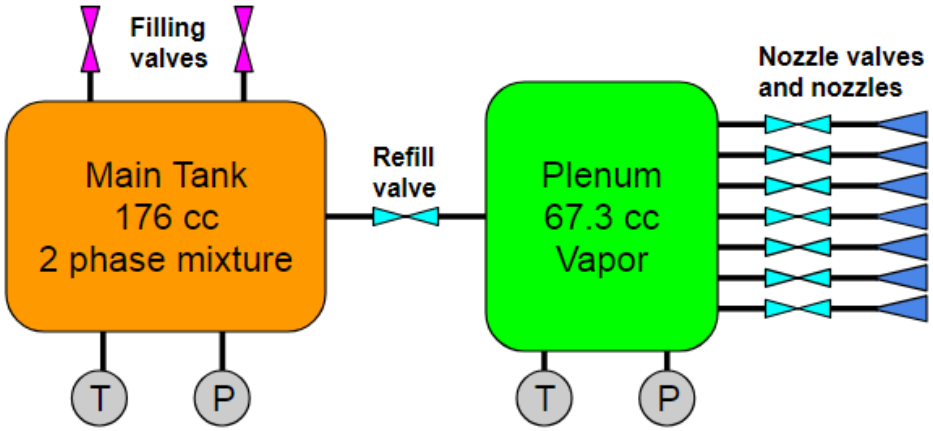

Figure 2.4: Schematic of thruster propellant tanks and pipes.

than 45ºC. The saturation pressure at that temperature is 12.2 bar, well above the maximum expected operating pressure of 5.8 bar but below the design burst pressure of 17 bar.

Since the seven nozzles are all fed from the plenum, its volume determines the amount of time the thruster can be operated before the system must stop to refill the plenum. A larger plenum allows more impulses before a refill is required, but also reduces the volume available to the main tank, and thus the total impulse of the thruster. In consultation with the BioSentinel project management and ADCS team, the plenum was given a volume of 67.3 cm^3, which allows approximately 2 seconds of operation before requiring a refill.

A cutaway view of the printed structure is shown in Figure 2.5, with the plenum shown in green and the main tank in orange. The plenum appears discontinuous in the figure due to its complex geometry, and there is no cutting plane that would show it as a single tank, but all green sections are connected.

The nozzles and propellant pipes are also printed into the structure of the thruster, allowing them to interface directly with each other and the tanks without requiring pipe-to-tank or pipe-to-nozzle pressure seals. Reducing the number of pressure seals saves mass and volume, and reduces the number of potential leaks in the system.

Figure 2.6 shows a cutaway of the nozzle across a plane of symmetry, as well as a

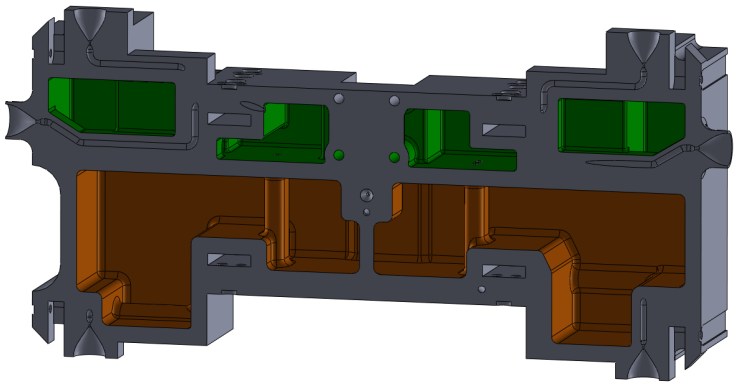

Figure 2.5: CAD cutaway of the printed structure, showing the plenum in green and the main tank in orange.

magnified image of the nozzle, showing the throat of the nozzle. This throat is the smallest interior feature, with a diameter of only 0.7 mm.

A good way to visualize the interior features of the printed structure is with a transparent CAD view with negative elements highlighted. One such view is shown in Figure 2.7, with the plenum and its associated pipes in green, the main tank in orange, and the nozzles and nozzle pipes in purple. The plenum and main tank are roughly divided along a horizontal plane, as seen in the figure. The manifolds are arranged such that they are all on the Y- face (the top face in the figure). This minimizes the disruption to the tank volume by allowing them to all use the same cutout volume. Four of the five manifolds impinge on the plenum volume, in order to preserve as much main tank volume as possible.

2.5.2 Manifolds and Sensors

There are five stainless steel manifolds that interface with the printed structure: two valve manifolds, two main tank manifolds, and one plenum manifold. The valve manifolds contain four valves each, along with a driving circuit board. The valves are attached to the manifolds via threaded compression fittings, and each valve has an upstream 5 μm filter to prevent particles from lodging in the valve.

The two main tank manifolds each have a quick disconnect filling port used for loading

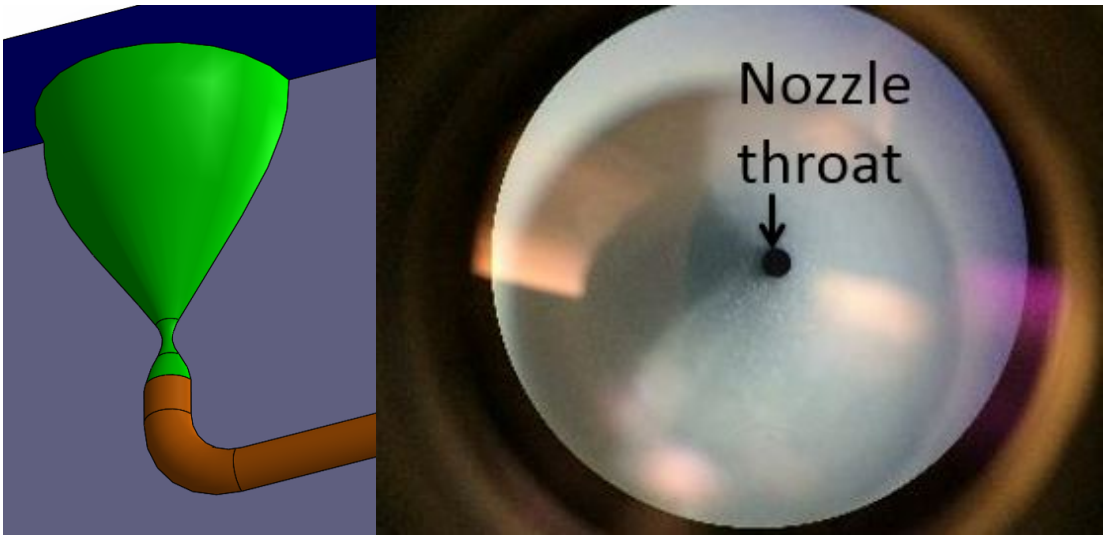

Figure 2.6: Left: nozzle cutaway, showing converging-diverging section (green) and feed pipe (orange). Right: magnified image of an as-printed nozzle.

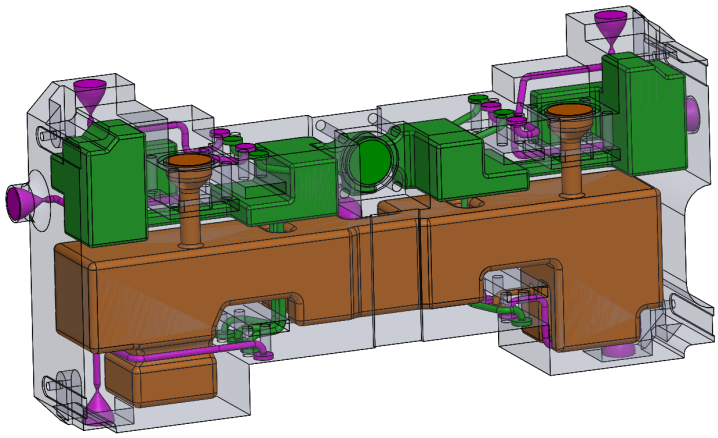

Figure 2.7: Transparent CAD, showing plenum (green), main tank (orange), and nozzles (purple).

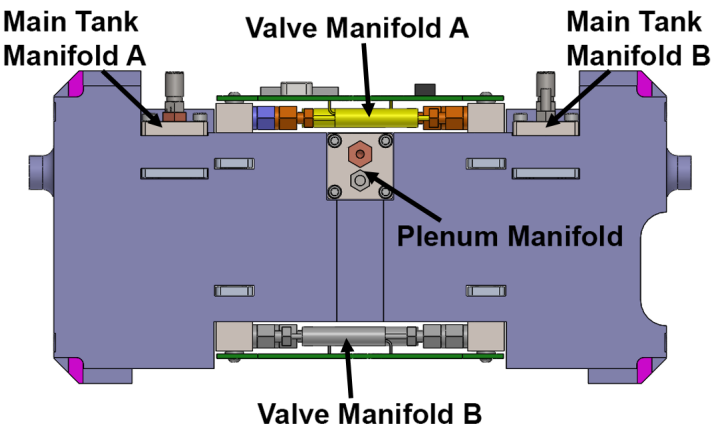

Figure 2.8: Thruster manifold locations.

propellant into the main tank. Each manifold also has a sensor, one has a ThorLabs TH10K thermister and the other has a Meas-Spec EPIH pressure transducer. The plenum manifold contains one TH10K and one EPIH. The four sensors allow the state of the propellant in both tanks to be known at all times, and are used to determine when the plenum should be refilled. Figure 2.8 shows a CAD image of the five manifolds installed on the thruster.

The manifolds are attached to the printed structure via face sealing O-rings, seated in grooves printed into the structure. Sealing force is provided by fasteners that run through printed holes in the structure and thread into helicoil plates. A total of 19 pressure seals are made between the manifolds and the 3D printed structure: one each from the three tank manifolds and eight each from the two sensor manifolds.

2.5.3 Electronics

Each valve manifold also holds a circuit board that contains the driving electronics for the valves. The board is screwed to the manifold by two 2-56 fasteners and soldered to the leads of the valves. The boards are labeled “PCB-A” (Y- face) and “PCB-B” (Y+ face), and are connected together with a soldered ribbon cable. Figure 2.9 shows the valve manifolds before they were integrated onto the structure.

Each board contains the driving electronics for the four valves on its manifold. PCB-A

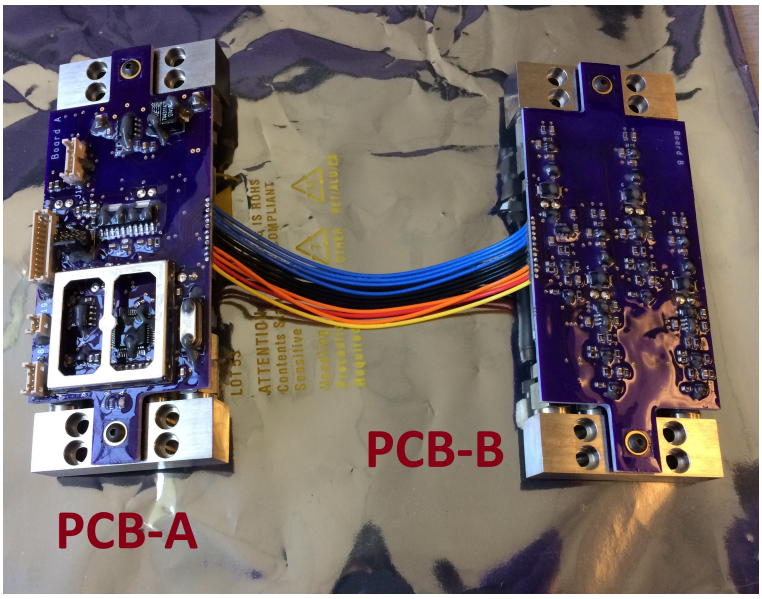

Figure 2.9: Valve manifolds before integration, showing manifold A (left) and manifold B (right). Note the headers and RF shield on manifold A.

also contains control electronics for the thruster and signal conditioning for the sensors. A block diagram of this arrangement is shown in Figure 2.10.

Control is provided by an LPC1549 microcontroller using a Cortex-M3 processor with 36 kB of memory and 256 kB of flash memory. The processor cannot write to its flash memory, which is only used for storing the firmware, so it is unable to save data past a power cycle. The processor communicates with the spacecraft over a 57.6 kbaud RS422 serial link, receiving commands and replying with acknowledgment and telemetry. The sensor signal conditioning consists of wheatstone bridges for the thermisters and op-amps for thermisters and pressure sensors. The output of these are fed into the A/D inputs on the microcontroller. An external oscillator is used to improve frequency stability over the range of temperatures expected by the spacecraft. There are three voltage regulators on PCB-A, which supplies conditioned power to PCB-B. A switching regulator converts the unregulated battery input (12-21V) to the 9V needed to operate the valves. Two linear regulators convert the regulated 5V input to 3.3V for the microcontroller and other electronics, and 1.8V for the valves.

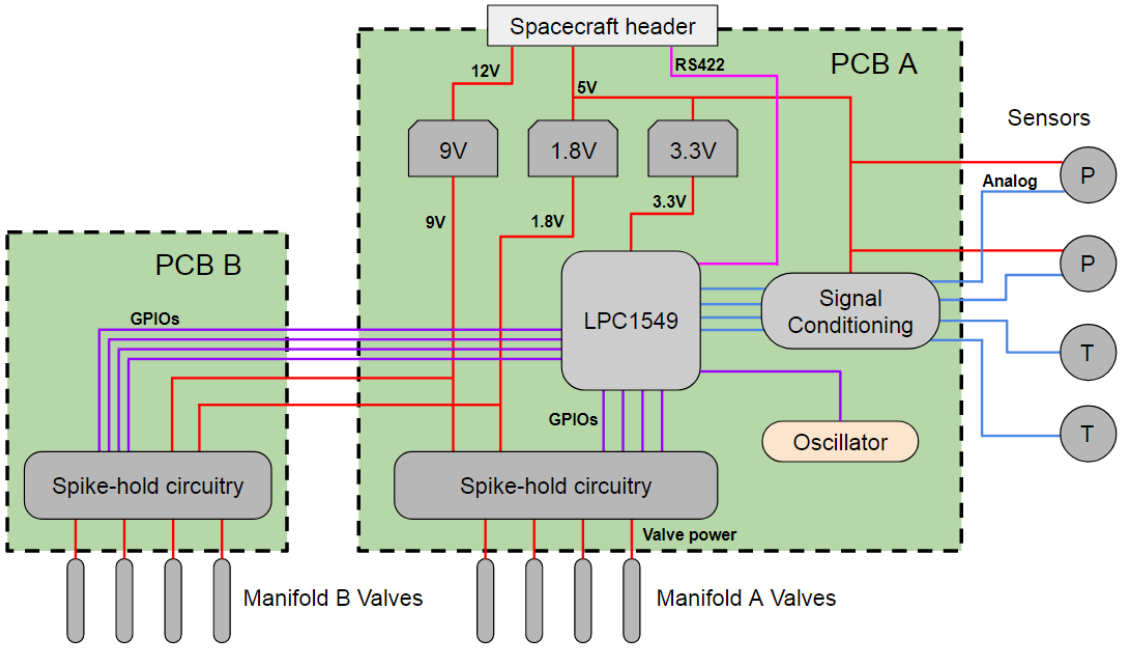

Figure 2.10: Block diagram of thruster electronics, showing power (red), analog (blue), and digital (purple) connections. The boards themselves are the same dimensions.

The microcontroller continuously monitors the pressure in both propellant tanks. When the pressure in the plenum drops below a defined percentage (command-configurable but defaults to 80%) of the main tank pressure, the refill valve is opened automatically. All incoming commands to open nozzle valves are ignored until either 10 seconds have passed or the plenum pressure recovers to 95% of the main tank pressure. In the event that one of the pressure sensors is damaged, the thruster can be switched into a "dead-reckoning" mode. In this mode, autonomous refilling is based on accumulated nozzle open time, rather than pressure sensor feedback. When five seconds of valve open time has been accumulated across all nozzles, the plenum is refilled for four seconds. Finally, the plenum can be refilled manually by commanding valve 8 to open. Under no circumstances is the refill valve held open at the same time as any of the nozzle valves. While the thruster could potentially increase its duty cycle by refilling while nozzles are open, this was disallowed due to the risk of a processor latchup. If the microcontroller froze while the refill valve and one or more nozzle valves were open, the main tank could potentially lose all of its propellant

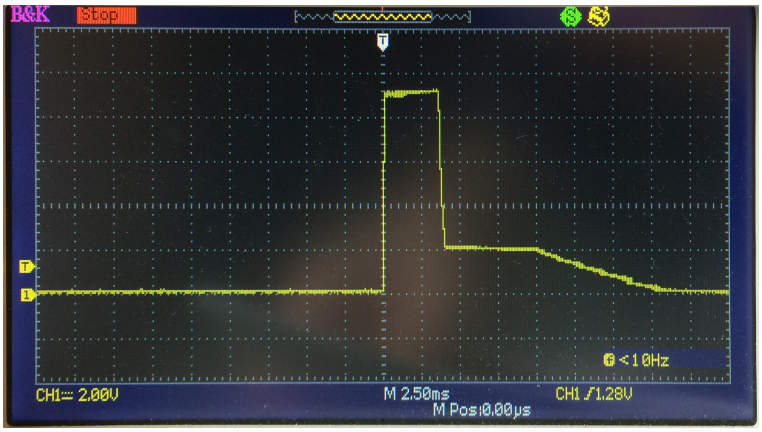

Figure 2.11: Oscilloscope capture of spike-hold voltage for a 10 millisecond pulse. Note that this was captured with no valve attached, so the voltage drains slowly when both switches are closed. With a valve attached, the final drop-off is sharp.

before the problem was identified and fixed.

The microcontroller receives commands from the flight computer at a maximum rate of 5 Hz over the serial line. The command packet contains a vector of valve open times; for example, a command to open valves 2 and 3 for 50 milliseconds. The command packet also contains a flag that can place the thruster into dead reckoning mode, and a field to change the plenum refill threshold. All command packets, regardless of content, generate a telemetry response, which contains the most recent pressure and temperature measurements, accumulated open time for each valve since the last power cycle, the current plenum refill threshold, and the software version.

The valves require a "spike-hold" voltage pattern, where a high voltage (9V) is applied for 3 milliseconds, then a lower voltage (1.8V) is applied as long as the valve must be held open [46]. This was achieved with two high-side voltage switches, one connected to 9V, the other to 1.8V. The low voltage switch is driven directly by a general purpose input/output (GPIO) from the microcontroller, which is held at logic high to hold the valve open. To produce the spike voltage, a transistor network is used to detect a rising edge on the GPIO and produce a 3 ms logic pulse. This is supplied to the 9V switch to produce the spike. The voltage profile produced is shown in Figure 2.11.

2.5.4 Filling System

A custom propellant filling system was designed for the thruster. The system must be able to fill the thruster with liquid at a moderate pressure, and must be inexpensive, fast, and easy to operate. Previous filling systems relied on opening a gas connection between the thruster and a propellant dewar located at a higher elevation, and used the gravity-induced pressure difference to cause liquid propellant to condense in the thruster. This system was functional, but was also slow, and it was difficult to determine when the thruster was filled. A conventional refrigerant extraction pump was considered too expensive and too risky, as it could potentially overpressurize the thruster and damage it. Complicating matters, both connections on the propellant dewar were on the top of the bottle, and the dewar was far too heavy to invert or even lift, so the gravity fill method would not be possible without significant effort.

The final version of the BioSentinel filling system used an intermediate bottle, filled from the main dewar using suction. The bottle was evacuated using a small Venturi-style pump, then connected to the liquid fill line of the dewar. The suction created by the vacuum draws liquid into the bottle, which can then be sealed off and weighed to determine the mass of propellant that was extracted. If the bottle was overfilled it could be vented down to an appropriate mass. The bottle is then positioned above the thruster and connected to both fill ports, allowing liquid to flow into the thruster and gas to flow out. This process is illustrated in Figure 2.12.

This has two advantages over filling the thruster with vacuum suction directly. First, there is no risk of overfilling the thruster itself, since it is filled from the bottle, which is massed before and after filling. Second, if the bottle is underfilled, it can be drained into the thruster, evacuated, and refilled from the dewar. If the thruster is filled directly, it cannot be evacuated a second time since it would already be full of propellant from the first filling. In addition, the vacuum suction method causes the propellant temperature to drop significantly as it flows out of the dewar. A metal fill bottle is better able to conduct

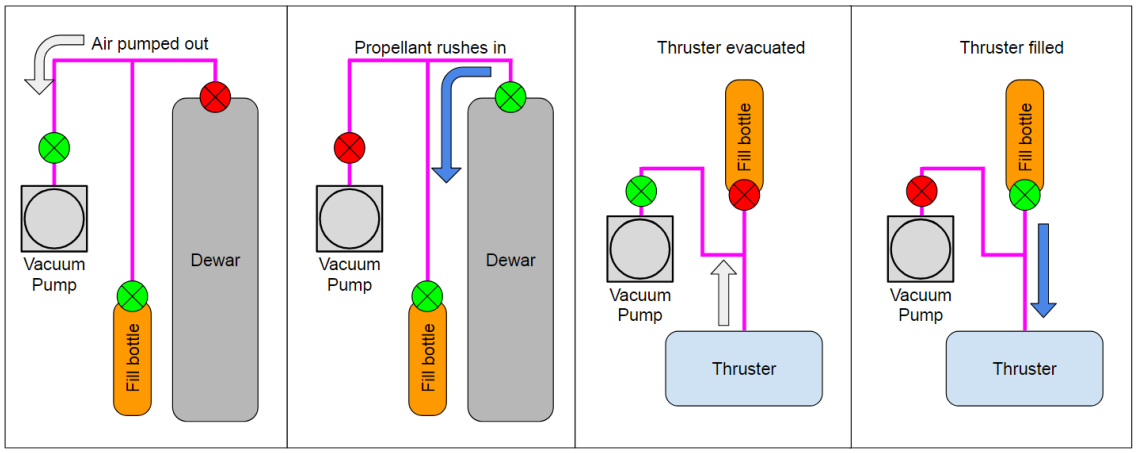

Figure 2.12: Thruster filling procedure.

heat to the propellant to warm it compared to the relatively insulating Bluestone, and there is no risk of accidentally damaging the thruster by getting the Bluestone too cold. Finally, the propellant fill bottle is smaller and more easily maneuvered than the dewar and vacuum pump setup, so the bottle can be filled and then easily brought into a clean room to avoid removing the flight unit from a clean environment.

2.6 Expected Performance

Before the structure was printed, simulations were conducted on the printed structure to ensure that it could withstand the maximum internal pressure of the propellant and to ensure that the system performance would be acceptable.

2.6.1 Tank Pressure

The safety requirements handed down from the SLS secondary payload program required the thruster to be designed to withstand 2.5 times its maximum expected operating pressure (MEOP). The maximum pressure is derived from the spacecraft maximum temperature of 50ºC. Since the tank is sized such that the main tank is always in a saturated state, the main tank maximum pressure is the saturation pressure at 50ºC: 584.2 kPa.

A finite element analysis of the printed structure was performed in Ansys. An inter-

nal pressure of 1460.5 kPa was applied in two scenarios: main tank alone and main tank and plenum. The plenum alone was not studied, since the plenum cannot be pressurized above the main tank. In the main tank only scenario, the maximum von Mises stress in the printed material was 43.27 MPa. In the scenario with both tanks pressurized, the maximum von Mises stress was 43.44 MPa, effectively the same as the main tank alone. In both cases it was substantially lower than the tensile and flexural strength of thermal post-cured Bluestone (66 MPa and 124 MPa, respectively) [45]. The large difference between the maximum von Mises stress at 2.5x MEOP and the yield strength suggests that the wall thickness could be reduced, saving mass and potentially increasing the tank volume. However, the tank walls are already only 3 mm thick in most places, and thinning them further would risk build failures. Since the thruster's predicted total impulse already exceeded the requirements, additional tank volume was not required, and the extra safety factor was left in place.

Stress plots are shown in Figures 2.13 and 2.14 for the main tank and both tanks simulations, respectively. The plots are shown projected onto the interior surfaces of the tanks, where the areas of highest stress are located, with the exterior surfaces shown in wireframe. The point of maximum stress was the same in each of the simulations, located on an interior corner of the main tank where a large flat surface meets perpendicular surfaces. The low stresses in the plenum are due to its unusual shape and lack of large continuous flat surfaces, which strengthens the shape, although it does make the tank less efficient volumetrically than the main tank. If the tank were redesigned for a higher pressure, this corner could be rounded to a larger radius to reduce the stress concentration, but as it is already well below the requirement, this was unnecessary.

The simulation constrained the model along the four mating faces that connect the thruster to the spacecraft structure, and a uniform internal pressure of 1460 kPa was applied to all interior faces in the tanks. Two of the four mating surfaces are highlighted in Figure 2.15, which also illustrates the mesh used for the simulation. The remaining two mating

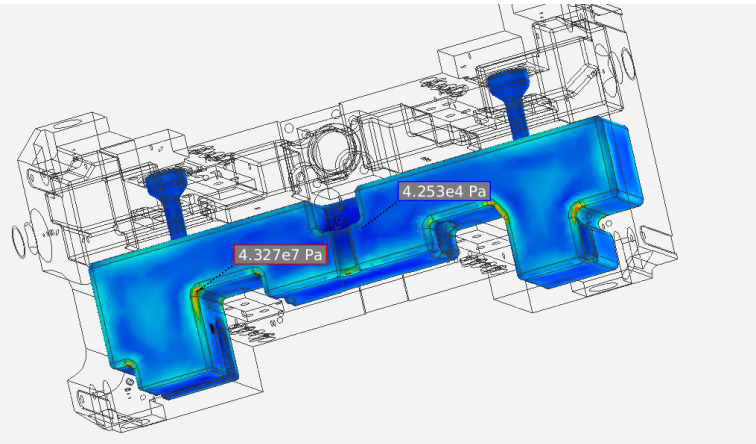

Figure 2.13: View of interior main tank surfaces (exterior surfaces in wireframe) showing von Mises stress during main tank pressure sim, max and min stress points are labeled.

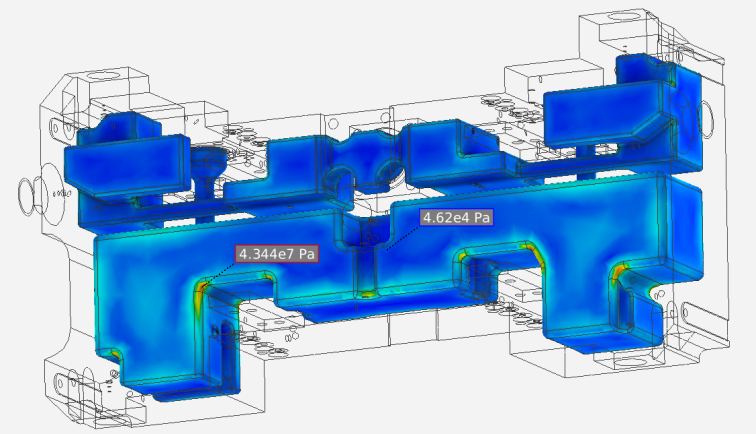

Figure 2.14: View of interior tank surfaces (exterior surfaces in wireframe) showing von Mises stress during pressure sim of both tanks, maximum and minimum stress points labeled.

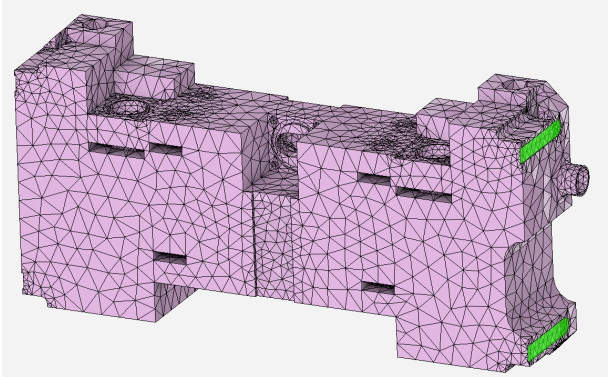

Figure 2.15: BioSentinel thruster FEA mesh, showing constrained faces in green.

surfaces are on the opposite face to the two shown.

Due to the non traditional manufacturing method and the potential for uninspectable manufacturing defects, the SLS safety panel also required that the flight unit thruster undergo a proof pressure test, in which the thruster is pressurized and held above the MEOP to demonstrate survivability. This test was carried out successfully, and is described in further detail below.

2.6.2 Performance Model

A simulation was developed to predict the performance of the thruster before it was printed. A detailed computational fluid dynamics simulation for the nozzles was not carried out, as an extensive testing campaign was already planned. Isentropic flow relations were used to make rough predictions for the performance.

The thrust produced by an ideal nozzle in vacuum is [47, 48]:

$$T = \dot{m} v_e + P_e A_e \tag{2.3}$$

where T is the thrust, $\dot{m}$ is the mass flow rate from the nozzle, V_e is the exhaust velocity, P_e is the exhaust pressure at the exit plane, and A_e is the area of the exit plane. The first term is the thrust derived from the momentum of the exhaust, the second is the thrust derived from the pressure of the exhaust on the exit plane. This equation assumes that the

flow is completely parallel at the exit plane, which is a moderately good assumption for converging diverging nozzles. The specific impulse can be calculated from the thrust and the mass flow rate with:

$$I_{sp} = \frac{T}{g\dot{m}} \tag{2.4}$$

where I_{sp} is the specific impulse and g is the standard acceleration due to gravity (used to normalize I_{sp} to a time unit).

The mass flow rate at the exit plane must be equal to the mass flow rate through the throat for a steady state nozzle, so the mass flow rate will be computed at the nozzle throat:

$$\dot{m} = v^* \rho^* A^* \tag{2.5}$$

where ρ^* is the density at the throat, v^* is the velocity at the throat, and A^* is the cross section area of the throat. The throat Mach number in a supersonic nozzle is 1, so the throat velocity is simply the speed of sound at the throat. The speed of sound in a calorically perfect gas is:

$$a = \sqrt{\gamma RT} \tag{2.6}$$

where γ is the ratio of specific heats, R is the specific (not universal) gas constant, and T is the absolute temperature. The assumption of constant thermodynamic properties throughout the flow is necessary, since those properties are not available for the propellant. Since it is a cold gas system, there is not as large of a temperature range as in a combustion system, although there is still a temperature drop through the nozzle.

The density at the throat can be found using the ideal gas equation:

$$\rho^* = \frac{P^*}{RT^*} \tag{2.7}$$

where P^* is the pressure at the throat. P^* and T^* can be found using the isentropic compressible flow equations:

$$P = P_0 \left(1 + M\frac{\gamma - 1}{2}\right)^{\frac{-\gamma}{\gamma-1}} \tag{2.8}$$

$$T = T_0 \left(1 + M\frac{\gamma - 1}{2}\right)^{-1} \tag{2.9}$$

Where P_0 and T_0 are the stagnation pressure and temperature, and M is the Mach number. Eqs 2.8 and 2.9 can be used to find the conditions both at the throat and at the exit plane of the nozzle. The Mach number at the exit plane of an isentropic nozzle is simply a function of geometry:

$$\frac{A}{A^*} = \left(\frac{\gamma + 1}{2}\right)^{-\frac{\gamma+1}{2(\gamma-1)}} \frac{1}{M}\left(1 + \frac{\gamma - 1}{2}M^2\right)^{\frac{\gamma+1}{2(\gamma-1)}} \tag{2.10}$$

where A is the cross sectional area of the nozzle at the location specified, A^* is the cross sectional area at the throat, γ is the ratio of specific heats, and M is the Mach number at the location specified. This equation can be iteratively solved for M given a specific area ratio, such as the exit plane to throat ratio.

The stagnation conditions in Eqs 2.8 and 2.9 are the conditions at the nozzle, so the pressure loss through the valve must be considered. The Lee Company (the manufacturer of the valves) provides a guide for calculating the flow through the IEP valves, including estimates of pressure losses [49]. This guides uses a Lee Company flow restriction model called the "Lohm laws", which define the Lohm (Liquid Ohm) as a unit of flow resistance. In a gas, the Lohm restriction in a fully subsonic flow allows a mass flow rate of:

$$\dot{m} = \frac{2K f_T \sqrt{P_2 \cdot \Delta P}}{L} \tag{2.11}$$

where $\dot{m}$ is the mass flow rate in kg/s, K is a flow constant for the gas (0.152 kg/s), f_T is a temperature adjustment factor equal to 239K divided by the absolute temperature

in Kelvin, P_2 is the pressure downstream of the restriction, ΔP is the pressure drop across the restriction, and L is the flow resistance in Lohms. For restrictions with high enough pressure ratios to cause sonic (choked) flow, the flow rate is:

$$Q = \frac{K f_t P_1}{L} \tag{2.12}$$

where Q is the volumetric flow rate and P_1 is the upstream pressure. These two equations do not model high speed subsonic flows well, Eq 2.12 only covers M=1, and Eq 2.11 assumes the flow is incompressible. This is not a problem in the thruster simulation, however, since the flow through the valves is always sonic, so only Eq 2.12 is needed in most cases. The plenum refill does transition between subsonic and sonic, since the refill valve pressure ratio can be significantly lower than the pressure ratio across the nozzle valves. Because of this, the plenum refill flow model uses both Eq 2.11 and Eq 2.12.

Having sonic flow in the valves is not ideal from a performance perspective, since it reduces thrust (down from 240 mN for no flow resistance), but it was not feasible to improve this. Switching to higher flow valves would have improved thrust, but an extensive search was unable to find higher flow rate valves in a similar form factor, and larger valves would have reduced the tank volume available, and thus reduced the total impulse. Since the specific impulse is not affected as strongly by the flow resistance, it does not have a strong effect on total impulse, so there was not sufficient motivation to change the valves.

Eq 2.12 was solved together with Eq 2.5 to determine the mass flow rate through the nozzle, from which thrust and I_{sp} were calculated. The model predicted a thrust of 48.1 mN from each nozzle and a specific impulse of 46.9 seconds. Since the model makes several favorable assumptions, these predictions were expected to be higher than the true values. These assumptions are:

- The flow is isentropic
- R-236fa is ideal and calorically perfect

- Nozzle exit flow is perfectly parallel to the nozzle axis
- Thruster operates in a perfect vacuum
- There are no pressure drops in the system other than the one in the valve
- The flow is steady state

Ultimately, the measured thrust was found to be substantially lower than the model predicted (20 mN vs 48 mN), although the specific impulse estimate was quite close to the true value found for long pulse durations (between 44 and 46 seconds). This can be explained by higher-than-modeled flow restriction, which reduces thrust much more than specific impulse. A flow restriction of 9500 Lohms reduces the predicted thrust to 20 mN, and only reduces the predicted specific impulse to 46.7 sec. The most likely contributor to higher-than-expected flow restriction is the 5 micron filter that is placed upstream of each valve. These filters are necessary to prevent valve blockage, but if higher thrust was necessary, larger diameter filters could potentially be used with the same filter size to allow a higher flow rate.

2.7 Development Overview

A total of three thrusters were produced for the project, two engineering units and one flight unit.

The first engineering unit (EDU1) was built and tested in April and May of 2016, and tested on the Georgia Tech test stand in late May. In June and July 2016 it was tested at NASA Glenn Research Center, which confirmed the results from Georgia Tech. It was then sent to NASA Ames, where it passed further electronics and acceptance tests to ensure it conformed to the dimensional requirements of the spacecraft. It was intended to undergo a subsystem-level vibration test, but the test fixture failed during the test, causing damage to the printed structure. While the pressurized sections of the tank were not compromised, the

attachment system was, preventing it from undergoing vibration testing a second time. The thruster was then returned to Georgia Tech in September 2016 for additional performance testing. EDU1 was also used as a testbed for software changes before operating them on EDU2 or the flight unit.

EDU2 was built between November 2016 and January 2017, although it failed several leak tests before a problem with a leaky valve was diagnosed. Given the close agreement between the Georgia Tech and GRC results for EDU1, it was decided that EDU2 would only undergo performance testing at Georgia Tech. This was completed in January 2017, and it was shipped to Ames in February 2017. EDU2 underwent an environmental stress screening (ESS) test, in which the thruster was subjected to alternating high (45ºC) and low (0ºC) temperatures in a thermal chamber while operating the propellant valves.

During this test one of the valves failed, drawing normal electrical current at the operating voltage but failing to open. It was returned to Georgia Tech in April for valve replacement and additional testing, before returning to Ames in May 2017. EDU2 was integrated with the EDU BioSentinel spacecraft for a fit check, and underwent spacecraft-level vibration and environmental testing.

The flight unit was assembled in May 2017, and passed its first leak test. Extended performance testing was conducted at Georgia Tech in June and July 2017 to test a wider range of conditions than EDU1 or EDU2 had experienced, and it was shipped to Ames in August 2017. While at Ames, one of the pressure sensors failed, with a maximum output at all times. The thruster was returned to Georgia Tech in October 2017. The replacement pressure sensor arrived in December, and was installed. Additional electronics changes were made to resolve a GPIO spike issue that was observed on EDU2 and the flight unit. As part of this change, new circuit boards with additional valve protections were made. The valve power source was delayed relative to the microcontroller, so that no valves could be opened in the first 100 milliseconds of operation. This solved the GPIO spike issue, and after another testing campaign, the thruster was returned to Ames in June 2017. The

flight unit underwent acceptance testing and ESS, and has not had any additional problems to date. The thruster will be stored separately from the spacecraft bus until approximately six months before launch, at which time it will be filled and integrated with the rest of the spacecraft.

2.8 Test Stand

A thruster test was built to support testing of the BioSentinel thruster at the SSDL [50]. The stand is capable of measuring small impulses, and was used to verify the performance of the system, both in impulse and specific impulse. The stand was designed to be low-cost and simple to operate in order to fit within the budget and personnel constraints of a university lab. The stand was used for all testing that took place at Georgia Tech, on both engineering units and the flight unit, and measured roughly 150,000 impulses of various pulse widths.

2.8.1 Vacuum Chamber

Since the exit velocity of the propellant is dependent on the pressure ratio of the tank to ambient pressure, all performance testing must be carried out in vacuum. The test stand was built to fit inside the SSDL's vacuum chamber, a small cubic chamber built by LACO Technologies, shown in Figure 2.16. The chamber uses two pumps: a LACO W2V40 rotary vane roughing pump and a Laybold Turbovac 350ix turbomolecular pump. It is capable of reaching a nominal base pressure of 10^{-6} Torr at room temperature when the chamber is empty and clean. The pressure is measured by an INFICON Gemini MPG500 dual Pirani/Cold Cathode pressure gauge. The small internal volume of the chamber limits the maximum size of the test stand, but also allows it to be pumped down to vacuum relatively quickly; a typical vacuum cycle takes 20 minutes to reach 10^{-5} Torr from 1 atmosphere.

Figure 2.16: SSDL Vacuum Chamber.

2.8.2 Test Stand Design

The test stand is a torsional pendulum design [51], in which a horizontally rotating arm is used to determine the impulse applied. Its design is based on a similar stand designed and built at NASA Glenn Research Center [52] to test pulsed plasma thrusters, which have a similar thrust profile as the BioSentinel thruster (low thrust magnitude for a short period of time). The reference minimum impulse bit the stand was designed to measure is a 40 mN thrust lasting 3 milliseconds, an impulse of 120 μN-s.

Measuring the time varying thrust profile of this impulse would be nearly impossible with a pendulum-style test stand. Such stands are best modeled as second-order systems, with a period given by:

$$T = 2\pi\sqrt{\frac{I}{\kappa}} \tag{2.13}$$

where T is the period, I is the mass moment of inertia about the axis of rotation, and κ is the torsional spring constant of the system. This period is a useful characteristic for determining how quickly the system can follow an input. If the input occurs on a timescale

significantly smaller than the period, it will not be captured. In order to measure the reference impulse, the stand would require a sub-millisecond period. Since decreasing the mass moment of inertia of the stand is limited by the mass of the thruster itself, the stiffness of the system must be greatly increased, which reduces the magnitude of the oscillations and thus the resolution of the stand. If the stand was completely massless, with only the mass of the thruster on a 0.5 meter arm contributing to the moment of inertia, the spring constant would have to be 1.184×10^7N-m/rad in order to achieve a 1 millisecond period. A 40 mN thrust would deflect this arm by only 850 pm (8.5×10^{-10} m), or roughly half the diameter of a DNA helix.

Instead of attempting to measure such small displacements, the stand was designed with a period several orders of magnitude longer than the thrust duration, approximately 10 seconds, which allows a stand with low stiffness and a relatively large oscillation amplitude. The long period causes the stand to respond to a thruster pulse as if it were an instantaneous impulse. This means it can only measure the total impulse, and cannot recover the entire thrust profile. However, since the spacecraft itself also responds to the thruster's pulses as if they were instantaneous, the impulse measurement is more relevant.

The stand consists of a fixed aluminum frame that supports an arm that rotates in the horizontal plane. A schematic view of the stand's rotating components is shown in Figure 2.17, and those components are highlighted on a photo of the test stand installed in the SSDL vacuum chamber in Figure 2.18. The stand arm (orange) is free to rotate in the horizontal plane about a vertical axle (blue). The thruster is attached to the arm on the right side, oriented to produce thrust in the horizontal plane perpendicular to the arm, and the other end of the arm is counterweighted for balance (green). The deflection of the stand arm is measured by a Linear Variable Differential Transformer (LVDT), shown in cyan. The LVDT core is attached to the rotating arm, and the housing is attached to a bracket on the stationary frame. LVDTs are designed to measure linear motion, but since the overall rotation of the stand is small (less than one degree in either direction) the small

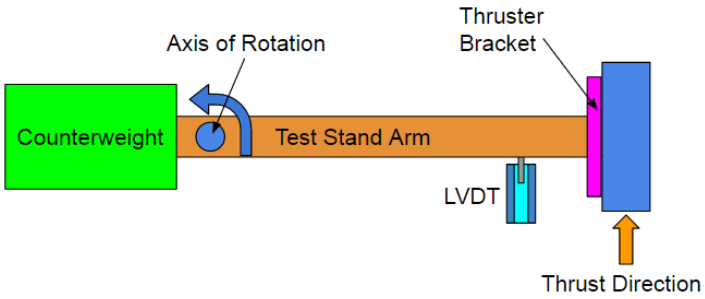

Figure 2.17: Schematic of test stand's rotating components.

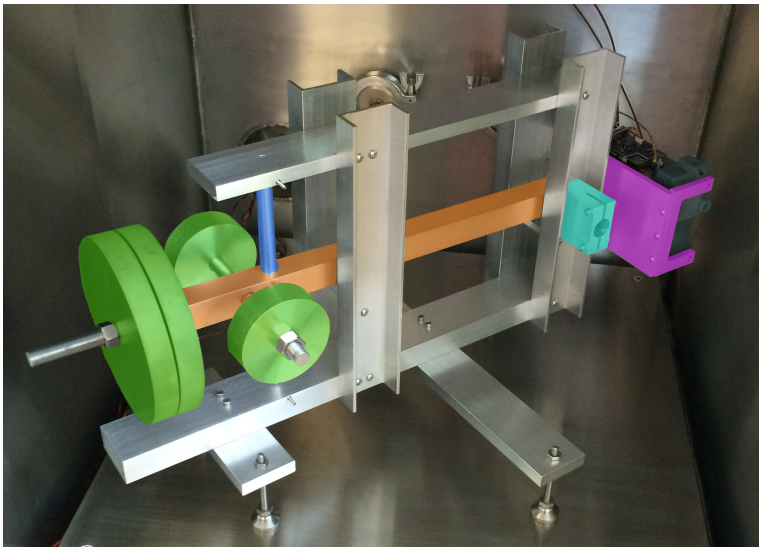

Figure 2.18: Test stand in the SSDL vacuum chamber, showing swing arm (orange), counterweights (green), rotational axis (blue), LVDT bracket (cyan), and thruster bracket (purple).

angle approximation is usable here. The thruster is placed as far from the axis of rotation as possible in the limited available volume to increase the moment delivered to the stand. The arm has a maximum angular travel of ±0.6°.

The blue vertical axle is connected to the stationary frame at the top and bottom by flexural pivots. Each flex pivot consists of a pair of concentric cylindrical sleeves connected by leaf springs. The sleeves can rotate relative to each other up to 30 degrees, and there is no sliding contact between the sleeves. This makes the flex pivots nearly frictionless, with especially low static friction. The lack of sliding contact allows them to operate with no lu-

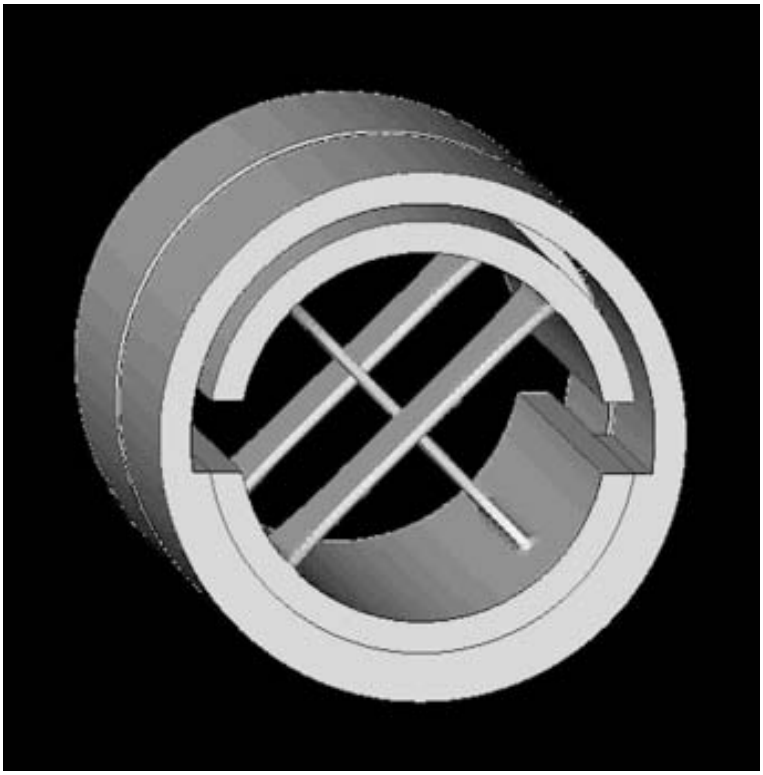

Figure 2.19: CAD image of a flex pivot, showing internal leaf springs [53].

brication, which simplifies their use in vacuum, since most common bearing lubricants are not vacuum compatible. Additionally, the leaf springs provide a built-in restoring torque, eliminating the need for separate torsion springs. A CAD image of a flex pivot is shown in Figure 2.19.

The stand arm counterweights are three metal discs, two aluminum and one steel, with tapped center holes screwed onto threaded rods. This allows their position to be finely adjusted, then locked in place with hex nuts. The center of mass of the arm is set to be approximately 2-4 cm away from the axis of rotation in the direction of the thruster, rather than perfectly balanced. This allows the frame's leveling feet to be used to set the zero point of the stand, which would otherwise have to be set via careful tuning of the flex pivot's installation angle. This deliberate imbalance simplifies operation of the stand, but also introduces additional restoring torque to the system which must be accounted for.

The LVDT used is a MacroSensors DC-750-125 with a range of ±3.175 mm. An LVDT

requires no contact between the housing and core, so no additional friction is introduced in the system. The coil voltage is measured at 1000 samples per second by a National Instruments USB-6002 DAQ.

2.8.3 Test Stand Dynamics

The test stand arm is a damped oscillator, the motion of which is approximated over a small angle as:

$$I\ddot{\theta} + c\dot{\theta} + 2k\theta + mgx_{COM}\psi\theta = 0 \tag{2.14}$$

where I is the mass moment of inertia, θ is the rotational displacement of the stand arm in the horizontal plane, c is the damping coefficient, k is the spring constant of one of the flex pivots (doubled because there are two such pivots on the axle), m is the mass of the rotation components, g is the local acceleration due to gravity, x_{COM} is the location of the rotor's center of mass relative to the axle, and ψ is the angle between the stand arm and the horizontal plane in the zero position. The first three terms are the standard terms for a second order angular system, and the fourth term accounts for the additional restoring torque provided by the deliberate center of mass offset discussed above. The angle ψ and the center of mass location are difficult to precisely measure in practice, so the last two terms can be combined into a single restoring torque term with an effective spring rate:

$$I\ddot{\theta} + c\dot{\theta} + k_{eff}\theta = 0 \tag{2.15}$$

$$k_{eff} = 2k + mgx_{COM}\psi \tag{2.16}$$

Equation 2.15 is then divided by the moment of inertia and the terms are consolidated to obtain the conventional pendulum equation of motion:

$$\ddot{\theta} + \frac{c}{I}\dot{\theta} + \frac{k_{eff}}{I}\theta = 0 \tag{2.17}$$

$$\ddot{\theta} + 2\zeta\omega_n\dot{\theta} + \omega_n^2\theta = 0 \tag{2.18}$$

where ζ is the system damping ratio and ω_n is the natural frequency. The characteristic solution to these equations of motion is:

$$\theta(t) = Ae^{-\zeta t}\cos(\omega t + \phi) + b \tag{2.19}$$

where A is the amplitude at t=0, ϕ is the phase of the oscillation at t=0, and b is the mean, or bias, of the oscillation. Note that Eq 2.19 is only valid when there are no external forces acting on the stand, since it was obtained by integrating the free oscillation equation of motion in Eq 2.18. This means that the solution is only valid when the stand is oscillating freely, not while thrust is applied.

2.8.4 Test Stand Operation

The test stand does not have any active damping elements, so the only damping in the system comes from the friction in the flex pivots and the cables that run to the thruster. Due to the low damping of the system and the high sensitivity of the LVDT, the oscillations from a typical impulse are detectable for approximately fifteen minutes before decaying into the background noise. To achieve a higher pulse rate during testing, the thruster is pulsed more often than this, so that the stand is still oscillating from a previous impulse when the next impulse is produced. The two oscillations are separated when processing the data, as detailed in the next section. The actual pulse rate is chosen to avoid resonance with the period of the stand, which would cause the amplitude to increase and saturate. This is dependent on the mass properties of the thruster being tested; when testing the BioSentinel thruster the stand period was 10.2 seconds, so a pulse spacing of 65 seconds was chosen.

The stand is capable of operating autonomously once the thruster is installed and powered, which allows long tests of thousands of impulses to be run without constant super-

vision. A Matlab program is used to control the tests and coordinate data collection and thruster operation. The script continuously reads LVDT measurements from the DAQ using the NI Matlab plugin, sends commands to the thruster over a serial connection, and reads thruster telemetry back on the same serial connection. A configuration file is provided to the Matlab script to define the number of impulses and their durations. After each pulse the raw LVDT measurements, as well as telemetry (pressure, temperature, and thruster health data) are saved. The data processing requires post-test mass results, so it must be post-processed, not run in real time.

2.8.5 Test Stand Data Processing

Because the thrust duration is significantly shorter than the period of the test, the thrust can be modeled as an instantaneous impulse. As discussed above, the stand's equation of motion (Eq 2.19) is only valid when the stand is oscillating freely with no external forces. Since the impulse is instantaneous, Eq 2.19 is applied piecewise around the impulse:

$$\theta = \begin{cases} A_1 e^{-\zeta t}\cos(\omega t + \phi_1) + b & t < t_f \\ A_2 e^{-\zeta t}\cos(\omega t + \phi_2) + b & t \geq t_f \end{cases} \tag{2.20}$$

where A_1 and A_2 are the amplitudes before and after the impulse, and ϕ_1 and ϕ_2 are the phases before and after the impulse. These piecewise equations are fit to the displacement data collected before and after the impulse using a least squares batch method. The two equations are required to be equal at $t = t_f$, the moment of impulse, since the angle of the stand must be continuous. The discontinuity in angular velocity is estimated here as a change in amplitude and phase, with the other parameter remaining constant.

In order to fit Eq 2.20 eight parameters must be estimated: A_1, A_2, ζ, ω, ϕ_1, ϕ_2, b, and t_f. Of these, four are relatively simple to estimate. ω and ζ are properties of the stand, and do not change greatly from one test to the next. They are still estimated with each impulse to account for slight changes in the stand properties due to mass loss of the

thruster as propellant is consumed, but because the change is small the initial value in the estimator is close to the true value. The bias estimate starts with the average value of the peaks and troughs, which is close enough to also converge quickly. The time of impulse t_f (approximated as instantaneous) is controlled by the Matlab script, although it is still estimated to account for the possibility of latency between the command and the execution. Due to the simplicity of the thruster electronics, this has never been observed in testing. The amplitude initial value is the peak to trough distance at the beginning of the series and immediately after the impulse, and the phases are estimated using the time between the start of the series and the first peak.

Figure 2.20 shows deflection data captured from a typical test. The blue series is the raw angle data computed from the LVDT voltage, and the red line is the best fit from Eq 2.20. The impulse occurs at approximately 18 seconds, and manifests as a sharp change in angular velocity. The impulse is timed, as discussed previously, so that the pulse acts against the current motion of the stand, avoiding resonance and saturation. The apparent increase in the noise of the measured deflections at the peaks and troughs is simply an artifact of the plot, the noise level is not dependent on the stand arm position.

A typical best-fit will have an R^2 of 0.999 or better, the processing script requires an R^2 of 0.99, or the impulse is discarded. The most common reason for an impulse being discarded is saturation of the stand, causing the arm to bounce off of one or both of the physical limits. This can occur if the pulse timing allows resonance, or too much impulse is delivered.

Once the equations are fit, the angular velocity change across the impulse must be determined. This is done by differentiating Eq 2.19 to obtain:

$$\omega = \frac{d\omega}{dt} = -A\zeta e^{-\zeta t}\cos(\omega t + \phi) - A\omega e^{-\zeta t}\sin(\omega t + \phi) \tag{2.21}$$

The estimated parameters are used in Eq 2.21 at $t = t_f$ to obtain the angular velocity

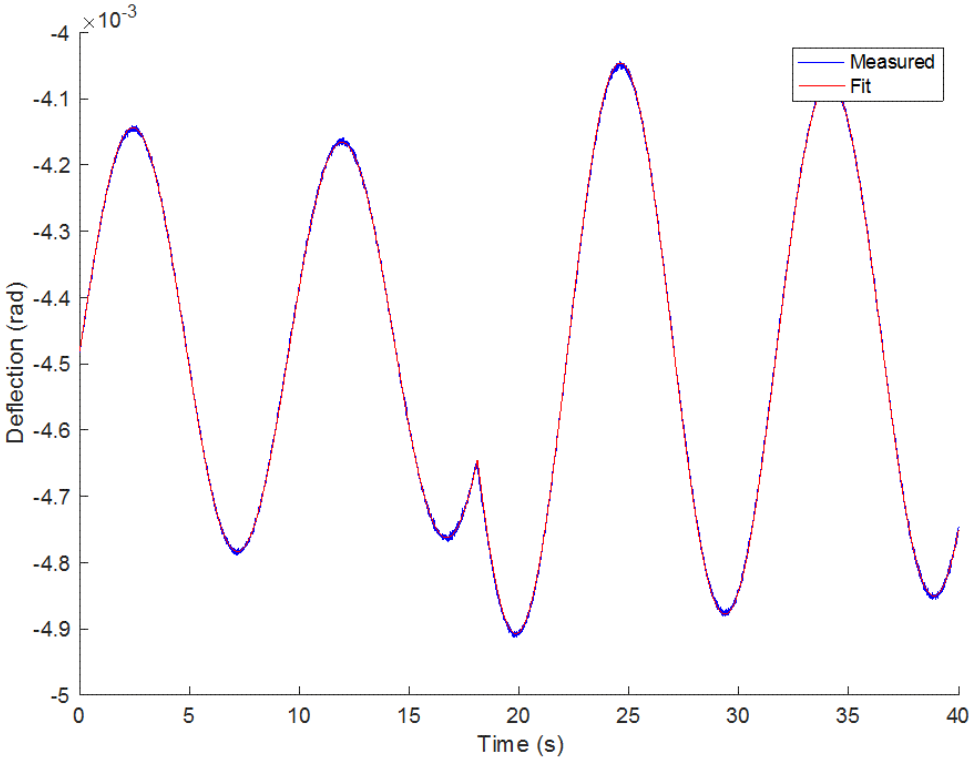

Figure 2.20: Plot of raw deflection data for a typical pulse, showing measured (blue) and batch fit (red) arm deflections.

immediately before and after the impulse. The angular velocity change is used to determine the impulse delivered using:

$$J = \frac{I\Delta\omega}{L_T} \tag{2.22}$$

where J is the estimated impulse, I is the mass moment of inertia of the stand, $\Delta\omega$ is the angular velocity change across the impulse, and L_T is the distance along the stand arm from the axis of rotation to the thruster nozzle.

2.8.6 Test Stand Uncertainty

Uncertainty characterization is an important part of test stand data processing. The uncertainty in the impulse estimate can be found with:

$$\sigma_J^2 = \sigma_I^2 \left(\frac{\Delta\omega}{L_T}\right)^2 + \sigma_{\Delta\omega}^2 \left(\frac{I}{L_T}\right)^2 + \sigma_{L_T}^2 \left(\frac{I\Delta\omega}{L_T^2}\right)^2 \tag{2.23}$$

where σ_J, σ_I, $\sigma_{\Delta\omega}$, σ_{L_T} are the uncertainties in the impulse, mass moment of inertia, angular velocity change, and thruster nozzle location.

The uncertainty in the mass moment of inertia is the most significant of the three error sources. The MOI of the stand arm itself is determined by CAD predictions, scaled by the measured mass of each part. This carries the assumption that the materials used are of uniform density and are free of manufacturing defects. The parts were made of typical aluminum and steel stock, and were closely inspected after machining to locate defects. The only defect found (and extra hole drilled in the horizontal arm) was modeled in CAD to incorporate into the MOI estimate. The mass and mass distribution of the empty thruster were also taken from CAD scaled by measured mass. Since the thruster is geometrically more complex and contains many internal features that cannot be measured there is more uncertainty in this. The largest contributor to MOI uncertainty is the distribution of propellant within the thruster tanks, primarily due to the thruster's location at the end of the test arm, far from the axis of rotation. Due to the complex geometry of the main tank there

are multiple locations where the liquid propellant can be. The nature of the installation process on the test stand prevents the thruster from being turned in such a way to drain the propellant into a known location. The propellant is assumed to sit at an equal level in all such locations, and is assumed to be consumed at a rate proportional to the commanded impulse. For example, a test series involving 1000 equal pulses that experienced a loss of 2 grams would assume that each pulse results in a loss of 2 mg of propellant. Typical tests have mass moment of inertia uncertainties between 2% and 6%, depending on how much propellant is loaded.

The angular velocity change uncertainty is determined using the covariance matrix calculated during the batch estimation. The uncertainties in the estimated terms are applied in a standard error propagation equation to obtain the uncertainty in the angular velocity. Due to the long measurement time and high quality of the fit these uncertainties are typically low, between 0.1% and 1%.

The thruster location uncertainty is the lowest contributor, since it can be measured directly. The maximum uncertainty in the along-arm direction of the thruster nozzle is ±0.4mm. Most of this is due to the clearance between the thruster mounting holes and the attachment fasteners, the rest is uncertainty in the true length of the stand arm and bracket.

The final uncertainties are dependent on the pulse duration. Pulses on the scale of 1 mNm-s typically have 3-6% final uncertainty, while shorter pulses on the scale of 200 μNm-s have uncertainties between 15-20%.

2.9 Test Results

Each thruster underwent an eight week test campaign to verify the system's performance [54]. After assembly and electronics testing, leak tests were conducted in vacuum at low, ambient, and high temperatures to characterize the propellant loss rate. These tests were conducted first, since when the leak rate was found to be too high the thruster was usually disassembled to fix the leak. This invalidates all previous performance testing, so doing

the leak tests first reduced the number of repeated tests that were needed. In the case of the flight unit, it was subjected to a proof pressure test after the initial leak tests, and then underwent another round of leak testing. The engineering units did not undergo the proof pressure test. Performance tests were conducted to determine the impulse and specific impulse of the thrusters. Finally, one of the engineering units (EDU2) was subjected to vibration and environmental stress screening tests at NASA Ames.

2.9.1 Leak Rate

The leak rate requirement of the thruster was derived from the expected shelf waiting time of the system after final fill and before launch. This gives a maximum allowable mass loss of 20 grams over 8 months, from requirement PROP-18 (see Table 2.1). This in turn defines a maximum allowable leak rate of 3.5 mg/hour. To measure the leak rate, the thruster is first outgassed in a vacuum chamber for one hour. This removes condensible volatiles like water from the surface of the thruster, which could interfere with the results of the test. The thruster is then removed from the chamber, massed, and returned to the chamber for at least 72 hours. The thruster is removed from vacuum and massed again to determine the average mass loss rate. These tests are conducted at room temperature, -10°C, and +50°C; all three tests are required to have a propellant mass loss rate under 3.5 mg/hour. EDU1 and EDU2 both failed their first leak tests. Replacing EDU1's main tank O-rings fixed the leak, but EDU2 was found to have a broken valve weld. Once the valve was replaced, the leak rate dropped below the 3.5 mg/hour requirement. The flight unit was measured to have an upper bound leak rate of 1.6 mg/hr.

Although there were many failed leak tests throughout the project, none of them were caused by the printed structure. Most of the leaks were the result of poorly seated O-rings. These could not be specifically identified, but in cases where removing a manifold and replacing O-rings fixed a leak, it was assumed to be the cause. In two cases leaks were caused by broken welds on the solenoid valves, likely caused by improper installation of

the swage fittings during assembly. In one case the leak was caused by a stuck filling valve. All of these cases were most likely the result of integration being done in a university lab by a relatively inexperienced graduate student. It is likely that the leaking issues would have been worse if the thruster was a conventional design, since more more pressure seals would be required.

2.9.2 Proof Pressure Test

Despite the large factor of safety applied in the design phase, there was still a risk of uninspectable printing defects inside the tanks, so the flight unit was subjected to a proof pressurization test. The thruster was connected to the regulator of an air compressor via a long, high pressure hose with oil/water filters and a calibrated pressure gauge. The hose was attached to one of the thruster fill port valves with a quick disconnect, similar to the propellant loading system. The test was carried out in a large room, and the thruster was contained in a shatterproof plastic box during the test, loosely constrained so that it could vent the air in the event of a burst. The large volume of the room would buffer the pressure increase and prevent hearing damage, and the box would catch the fragments, allowing reconstruction and possible diagnosis of the initial failure location. The system was pressurized to 690 kPa, approximately 18% over the MEOP. This factor was chosen because it was the maximum regulator pressure of the portable compressor that was available for the test. Since it was above MEOP, BioSentinel management and SLS safety deemed it acceptable.

A block diagram of the proof test hardware is shown in Figure 2.21, and a picture of the setup is shown in Figure 2.22.

The proof pressure test was concluded without any visible damage to the thruster. A leak test was performed immediately before and after the proof test and found no measurable increase in leak rate. The pre-test leak rate was 1.39 ± 0.14 mg/hr and the post-test rate was 1.49 ± 0.14 mg/hr, both well under the requirement of 3.5 mg/hr. The system's impulse

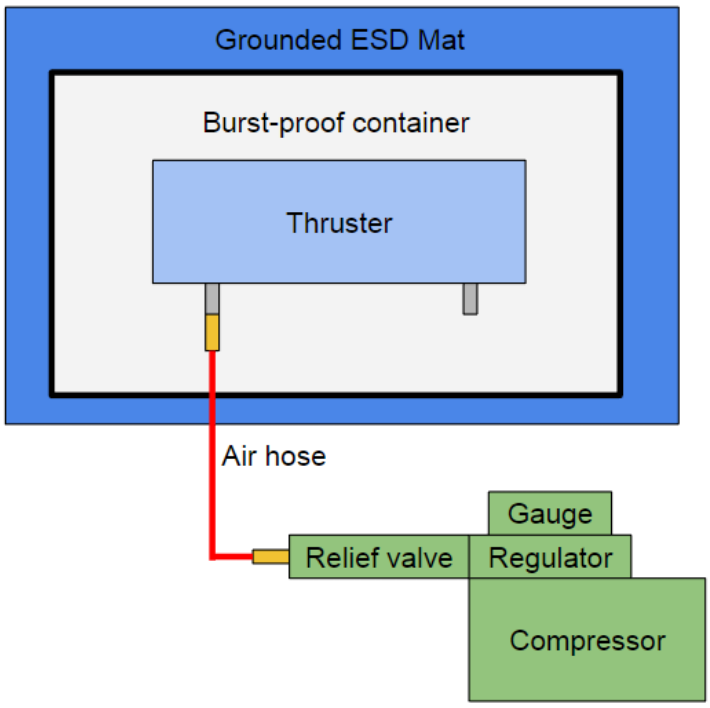

Figure 2.21: Block diagram of proof pressure test hardware.

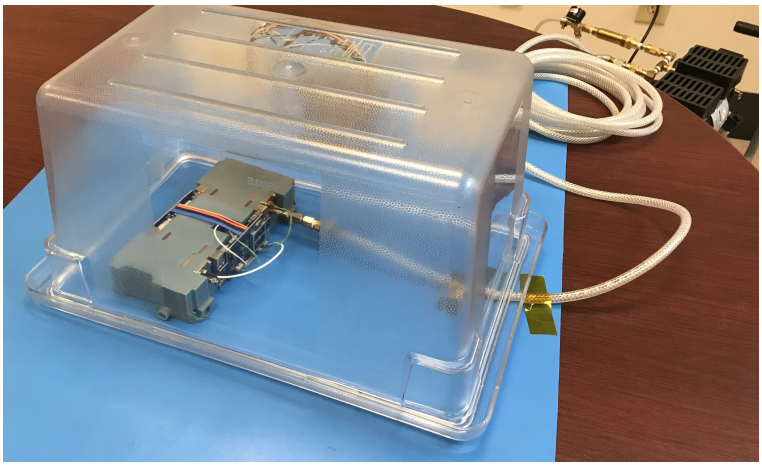

Figure 2.22: Proof pressure test hardware, showing thruster under shatterproof box, with the high pressure hose running to the compressor (upper right).

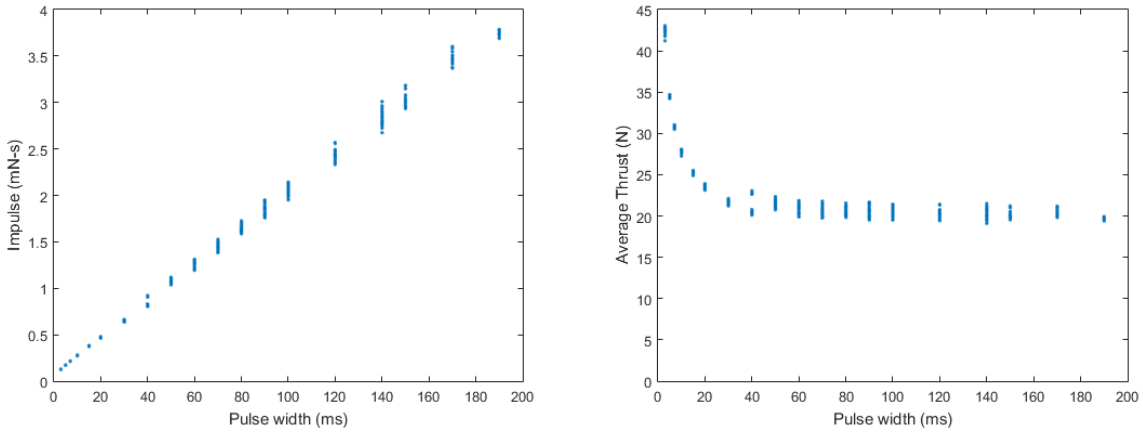

Figure 2.23: Plot of delivered impulse (left) and average thrust (right) as a function of pulse width.

behavior and specific impulse were also retested and found to be normal, indicating there was no damage to the structure.

2.9.3 Impulse

Next, the impulse of the system was tested for all seven nozzles. In these tests, the thruster produced 20 pulses each at 20 different pulse widths, ranging from 3 milliseconds (the minimum possible) to 200 milliseconds (the maximum expected in operations), for a total of 400 pulses. Figure 2.23 shows the results of a typical test. The plot on the left shows the impulses measured by the test stand, a roughly linear trend is clearly visible between impulse and pulse width, as expected. The impulse is then divided by commanded pulse width to obtain an average thrust value, shown in the figure on the right.

A relationship can been seen between average thrust and pulse duration, with higher average thrust at pulse times shorter than approximately 20 milliseconds. This is caused by the opening and closing delays in the valve. The solenoid valves have a spring-loaded armature that is pulled back by the coil's magnetic field, and it takes a finite amount of time to move. When the valve is commanded to open for a certain time t, it requires some time to open, and some time to close. While the armature is moving, the mass flow rate, and hence the thrust, will be reduced roughly proportional to how far the armature has moved. If the

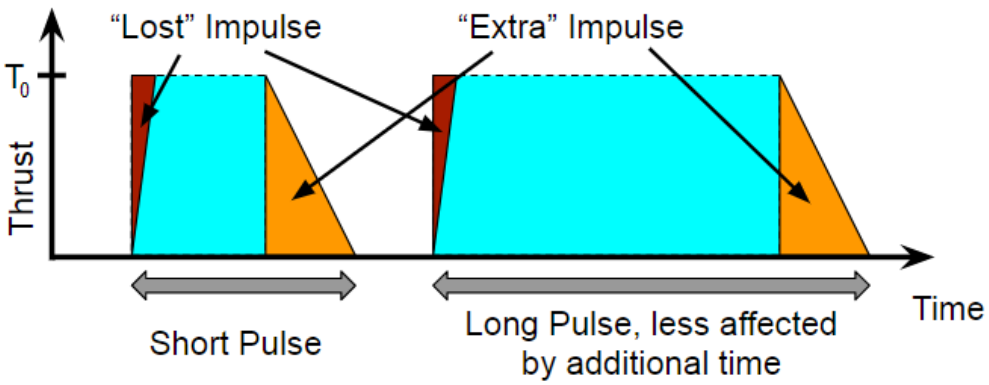

Figure 2.24: Simplified diagram of thrust as a function of time for a short and long pulse.

closing time is longer than the opening time, each pulse will gain some "extra" impulse, since they are open for longer than the commanded time. This is illustrated in Figure 2.24.

This is a simplified model, which assumes a linear relationship between armature motion and thrust, as well as a constant armature speed in opening and closing. However, regardless of the shape of the thrust curve, if the valve's opening and closing profiles are consistent, it can simply be modeled as additional impulse. This model is shown in Figure 2.25; the plot on the left shows the best fit line of the impulse measurements intersecting the $\Delta t = 0$ line at 74.7 μN-s, and the plot on the right showing the expected average thrust curve if each pulse was given an additional 74.7 μN-s. The slope of the fit line in the left hand plot is equal to the asymptote of the right hand fit line, and is the steady state thrust (20 mN).

This steady state thrust is substantially lower than the 48.1 mN predicted. This is most likely due to higher-than-predicted pressure losses in the system, as discussed previously. This reduction in thrust is acceptable in this application, since total impulse was unaffected.

2.9.4 Burn-Refill Testing

During testing, the plenum was refilled after each pulse to ensure the impulse would be as consistent as possible. However, in flight it will nominally be operated on an autonomous

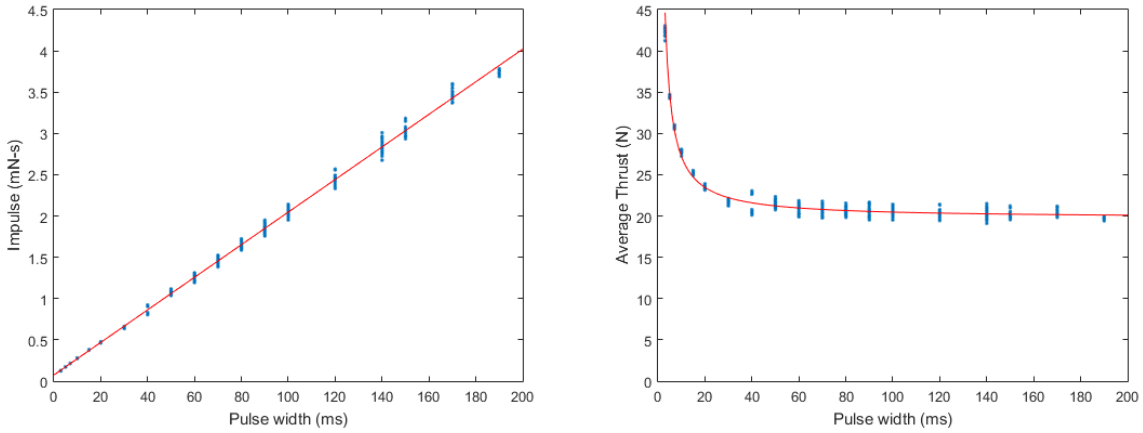

Figure 2.25: Plot of impulse (left) and average thrust (right) with fit lines at 74.7 μN-s extra impulse.

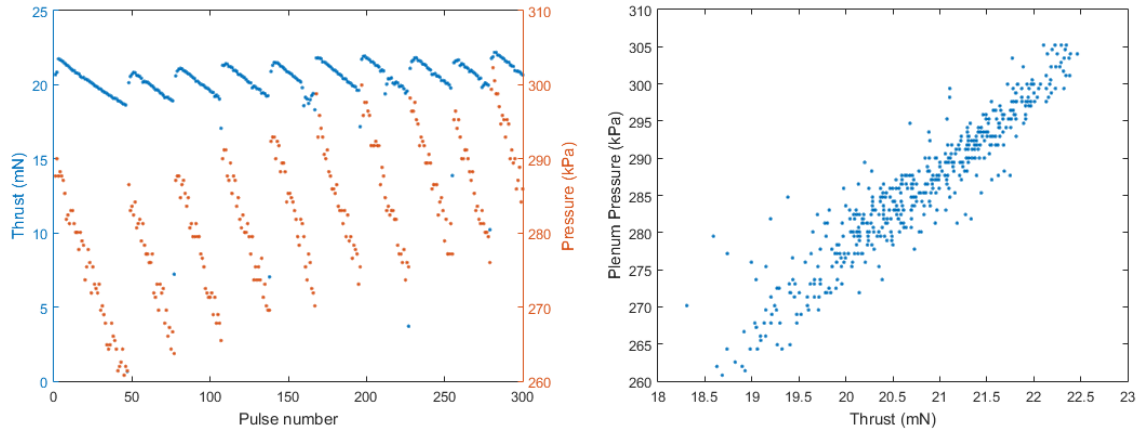

Figure 2.26: Left: Plot of pulse average thrust (blue) and plenum pressure (kPa) over 300 pulses. Right: Plot of same pulses, plenum pressure against thrust.

burn-refill cycle monitored by the pressure sensors. Some testing was done to verify this behavior, the results of which can be seen in Figure 2.26.

The figure shows the first 300 pulses of a 6000 pulse test. As the thruster is operated, the plenum pressure falls until it is less than 80% of the main tank pressure, at which point it is refilled back up to 95% of the main tank pressure. The thrust is roughly proportional to the plenum pressure, as can be seen in the second plot of Figure 2.26. The overall pressure rise seen across all 300 pulses is caused by the thruster warming up. Since these were the first 300 pulses of the series, the thruster was turned on shortly before they were conducted.

Since there is only a weak thermal path from the thruster to the test stand, the small amount of power dissipated by the electronics is enough to raise the propellant temperature slightly.

2.9.5 Specific Impulse

Specific impulse is a measure of the propulsive efficiency of a thruster, and is calculated from the sea level equivalent weight of fuel expended and the impulse achieved:

$$I_{sp} = \frac{J}{mg_o} \tag{2.24}$$

where I_{sp} is the specific impulse, J is the impulse achieved, m is the propellant mass consumed, and g_o is the standard acceleration due to gravity (9.806 m/s^2). The BioSentinel thruster has a low mass flow rate, and requires a relatively long valve open time to experience a measurable mass loss. Since the stand can only measure small impulses, the thruster is pulsed thousands of times, and the cumulative mass loss and cumulative impulse are used to determine an average specific impulse. The temperature of the system is monitored throughout the test, and a consistent pulse duration is used. In order for the test stand to collect sufficient oscillation data between pulses, the thruster produces an impulse once every 65 seconds, so the tests can take hours or days to complete. This slow overall mass loss rate allows the thruster to stay at ambient temperature, and gives a specific impulse measurement that is nearly unaffected by adiabatic cooling. If large maneuvers are required during the mission, this cooling will reduce I_{sp} and must be taken into account.

Initial testing at a range of pulse widths revealed a possible link between the pulse duration and the average specific impulse, however, further testing has shown this to be an artifact caused by the background leak rate of the system. EDU-1 was tested with a range of pulse durations between 3 and 150 milliseconds, with 1200 pulses each. The thruster underwent 72-hour leak tests before and after these specific impulse tests, which found leak rates of 1.81 mg/hr and 1.53 mg/hr, so an average leak rate of 1.67 was used to compute the mass lost to leakage. The duration of each test was controlled, lasting 24 hours each, with

Table 2.3: Specific impulse testing results at different pulse widths, showing predicted amount of mass lost due to leak. All tests involved 1200 impulses.

Test (hrs)	Pulse (ms)	Total Impulse (N-s)	Mass Loss (g)	Leak (g)	I_{sp} (s)
24	3	0.1556 ± 0.0058	0.39 ± 0.02	0.04	45.3 ± 1.72
120	5	0.2134 ± 0.0079	0.67 ± 0.02	0.20	46.3 ± 1.37
24	5	0.2029 ± 0.0076	0.49 ± 0.02	0.04	46.0 ± 1.78
24	10	0.3524 ± 0.0131	0.84 ± 0.02	0.04	44.9 ± 1.81
24	20	0.6196 ± 0.0231	1.47 ± 0.02	0.04	44.2 ± 1.82
24	50	1.4999 ± 0.0558	3.36 ± 0.02	0.04	46.1 ± 1.92
48	100	2.9188 ± 0.1086	6.54 ± 0.02	0.08	46.1 ± 1.92
24	150	4.5633 ± 0.1698	10.03 ± 0.02	0.04	46.6 ± 1.96

two exceptions. The 100 millisecond series was run for 48 hours because of a scheduling conflict. There were two 5 ms series, the first was run with a pulse spacing five time longer than normal, causing the test to last 120 hours instead of 24. This was done so that two series would be identical except for total duration. The two series did indeed have similar total impulse, and the longer series had a higher total mass loss. When adjusted using the average leak rate of 1.67 mg/hr, the mass loss was almost exactly canceled out, leaving the two I_{sp} estimates within the margin of error. The results of all eight tests are shown in 2.3.

The I_{sp} values all fall within the range of 44-47 seconds. Using the lowest value of 44.2 seconds, with a propellant load of 200 grams, the thruster can deliver a total impulse of 86.7 N-s, well above the Prop-22 requirement of 36 N-s. With the maximum safe loading of 220 grams, it is capable of a total impulse of 95.4 N-s. The first value is more relevant to the BioSentinel project, since the flight load will not exceed 200 grams, but the second value is used as the system's max capability.

2.9.6 Environmental Testing

The second engineering unit (EDU2) was subjected to GEVS level vibration testing in order to increase confidence in the 3D printed structure. The behavior of Bluestone under high vibration was relatively unknown, since the material had not been previously tested at these conditions. The test was conducted with a full flight load of 200 grams of R-236fa to simulate the conditions of the thruster during launch. EDU2 was tested for leak rate before

and after the vibration test, and no detectable increase in leak rate was found. EDU2 was also put through an environmental stress screening test (ESS), involving multiple cycles in a thermal chamber between 0ºC and 45ºC, with the valves actuating at each temperature extreme during each cycle. This test caused a failure in one of the nozzle valves, which was replaced, and a second ESS was passed with no component failures. The flight unit also underwent ESS and passed with no component failures.

2.10 System Volumetric Efficiency

As discussed previously, the volume limitations on the BioSentinel thruster were more constraining than the mass limitations, so the volumetric efficiency of the thruster was an important design parameter. Like the definition of propellant volumetric impulse (Eq 2.1), a system volumetric impulse can be defined using the volume of the entire thruster, not just the propellant:

$$J_{vol} = \frac{J_{total}}{V_{envelope}} \tag{2.25}$$

where J_{vol} is the system volumetric impulse, J_{total} is the total impulse of the thruster, and $V_{envelope}$ is the envelope volume of the thruster, or the volume in the spacecraft that must be allocated. The BioSentinel thruster's total envelope is 890.4 cm^3, and it has a total impulse capability of 95.4 N-s with a 220 gram load, giving a system volumetric impulse of 107.1 N-s/L. This compares well with other similar thrusters. Table 2.4 shows a comparison of the BioSentinel thruster with three others: the Palomar thruster by VACCO; CNAPS, a thruster built for the CAN-X mission by the University of Toronto; and the GomSpace Nanoprop 6U. All of these are CubeSat cold-gas and warm-gas ADCS thrusters with multiple nozzles and integrated electronics. It is noteworthy that the BioSentinel thruster is smaller than the other three systems, so a lower efficiency would be expected given a constant wall thickness, and it also must use a less spherical shape, which should also lead to

Table 2.4: Comparison of system volumetric efficiency between BioSentinel and similar thrusters.

	BioSentinel	Palomar [55]	CNAPS [56, 33]	Nanoprop 6U [57]
			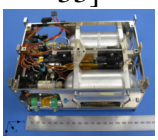	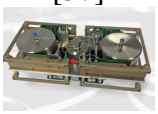
Volume (cm^3)	890.4	1073.5	1575.0	1000.0
Nozzles	7	8	4	4
Impulse (N-s)	95.4	85.0	81.4	80.0
J_{vol} (N-s/L)	107	79	52	80

decreased efficiency.

Although the BioSentinel thruster performs better than these systems on a volumetric basis, that does not mean it is a superior system in every sense. In systems that are more limited by mass than available volume, the volumetric impulse metric is less relevant. In addition, 3D printing for spacecraft is still a relatively new technology, and the use of AM to produce the thruster has led to additional safety reviews, complicating the secondary payload approval process.

2.11 Conclusions

This project employed the capabilities offered by additive manufacturing to produce a volumetrically efficient attitude control thruster for a 6U CubeSat. While the thruster is a separate module from the rest of the spacecraft, the use of 3D printing allowed for a reduction in part count and a larger propellant capacity by merging propellant tanks, piping, and nozzles into a single piece of printed material with complex internal geometry to make the most use of the allocated volume. Additionally, this system is modular and self-contained, and could be installed in other 6U CubeSats without modifying the design. This design serves as a starting point for the work done on multifunctional structures, by demonstrating the improved volumetric efficiency of such a design, and by showing that a physical, "flyable" system can be produced with additive manufacturing.

While the BioSentinel thruster project is complete, there is still future work to be done on this technology. Another thruster, also primarily 3D printed, was recently designed at Georgia Tech for an Air Force Research Labs mission called Ascent. Like BioSentinel, the other thruster was also designed around a nonstandard volume envelope, and used the available space efficiently. Future modular thrusters could make use of metal printing to allow higher pressure propellants. There are also upgrades to be made to the test stand, adding a calibration hammer would allow the stand to recalibrate itself during a test, reducing setup time and potentially allowing longer tests. Motorizing the leveling feet would also allow longer tests, by allowing the stand to rebalance itself as the mass of the thruster changes.

CHAPTER 3
EXTENSION OF THRUSTER TECHNOLOGY TO AN INTEGRATED CUBESAT STRUCTURE

The technology developed for the BioSentinel thruster was then extended to design a CubeSat structure that contains an integrated propulsion system, called the Structural Propulsion Unit Demonstrator (SPUD). This improves on the use of thruster modules in two ways. First, it is volumetrically more efficient, since it does not require any attachment points to the structure, and can make use of the structure for piping and nozzle placement. Second, it allows greater flexibility in the placement of nozzles than a thruster module, allowing the nozzle location and angle to be optimized for a specific purpose. The satellite was designed as a 3U inspector CubeSat, and a set of reference trajectories were generated based on this mission. The nozzle geometry was then optimized for this mission profile, to demonstrate how such a system can be tailored to minimize propellant consumption.

3.1 Reference Mission

SPUD is designed as a 3U CubeSat, chosen because of the popularity of the 3U form factor [7]. The system could easily be scaled either down to 1U or 1.5U, or up to 6U or larger, or to a non-CubeSat form factor. However, the extensive heritage and availability of COTS subsystem components for the 3U size made it a reasonable choice for a demonstration mission. Two reference missions for CubeSats requiring precise 6-DOF maneuverability were used in the design of SPUD: an inspector mission, and a docking mission.

An inspector is a small satellite that maneuvers around a larger object and observes it with some form of imaging system, which could be visible spectrum or IR cameras, or an active system such as LIDAR. This could be used to diagnose problems with larger satellites, such as a malfunctioning GPS or geostationary communications satellite, without

requiring the expense of a crewed servicing mission. It could also be used for routine inspection of space stations, replacing the more expensive and dangerous EVAs. Finally, it could be used to inspect asteroids and other space objects for scientific or economic purposes. In all of these cases, the inspector satellite must be capable of translating around the target object while pointing its sensors at various points on the target. An ideal inspector satellite would be able to translate arbitrarily while maintaining pointing of its sensors, so the propulsion system must be capable of generating thrust in any direction in the body axes. This requires three independent degrees of translational freedom. Likewise, the spacecraft must be able to rotate while translating, requiring three independent rotational degrees of freedom.

Inspector satellites have been demonstrated in space, starting with AERCam, a NASA inspector demonstration deployed from STS-87 in 1997 [58]. AERCam used 12 nitrogen gas thrusters to achieve 6 degrees of freedom, and was flown remotely by the Shuttle's pilot. It used two cameras to inspect the exterior of the shuttle, and was covered in Nomex padding to cushion against any accidental impacts. AERCam's operational life was limited by its primary batteries and its limited supply of nitrogen. With a more volumetrically efficient propellant, a longer mission would be feasible. Recently, missions have been proposed to develop inspector satellites in CubeSat form factors [59], using the availability of low cost CubeSat parts to reduce inspection costs.

The second possible use of a 6-DOF CubeSat is for rendezvous and docking. Although it has not yet been demonstrated, many such missions have been proposed [60], and potential docking mechanisms have been studied [61]. In order for such mechanisms to be practical, at least one of the satellites will require 6-DOF maneuverability in order to ensure the docking mechanisms are aligned both spatially and rotationally.

The maneuverability requirements on the satellites in these two cases are similar, since both situations involve precise proximity operations. Both cases require independent control of attitude and position, and benefit greatly from 6-DOF control, although 4-DOF con-

trol is theoretically sufficient. SPUD was designed to be adaptable to either mission, with a payload volume that could accommodate either the imaging equipment of an inspector satellite or with a docking mechanism.

3.1.1 Meeting the CubeSat Spec

In order to have the widest available range of launch opportunities, SPUD was designed to be compatible with PPOD, NanoRacks, and ISIPOD deployers. While there are some differences between these three standards, they are not mutually exclusive, and a single design can be compliant with all three. The fourth common standard, from Planetary Systems Corporation [6], is not compatible with the other three, since it uses tabs instead of rails to constrain the satellite inside the deployer. This standard has not been adopted as widely for 3U, although it is popular for 6U, so the 3U SPUD was designed to use a rail pod.

One of the requirements in the CalPoly spec (3.2.15) is that the primary structure and rails be made from Al 7075, 6061, 5005, or 5052. None of these alloys are compatible with existing metal printers, so a waiver will be necessary to gain approval for AlSi10Mg. The material properties of this alloy are similar to Al 6061, a common material for aerospace applications, with a density of 2.67 g/cm3 and a yield tensile strength of 240 MPa. However, since the CubeSat spec requires the structure to be one of the listed alloys, a waiver will still be necessary. A second waiver will be necessary for approval of the pressurized propellant tanks, although they will remain below 100 psia, which simplifies the approval process [30]. These non-conformities are unavoidable for any printed satellite that includes a propulsion system. All other requirements of the CubeSat spec can be met, including hard anodization of the rails and anti-corrosion coatings on all other exposed surfaces.

3.2 System Design

Figure 3.1 shows SPUD with and without its body-mounted solar panels, along with the body frame coordinate axes. The propulsion system is located near the center of the space-

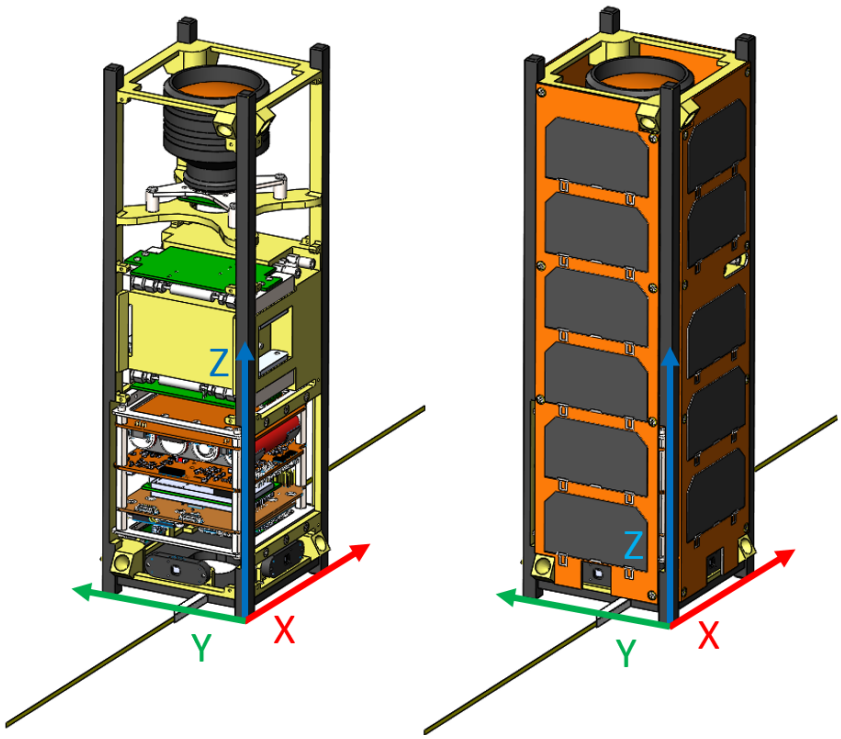

Figure 3.1: SPUD with solar panels (right) and without (left), showing body frame coordinate axes.

craft, with the imaging system aimed in the +Z direction and the avionics at the opposite end.

A detail view is shown in Figure 3.2 with internal components labeled. The deployable UHF whip antenna, sun sensors, and avionics are in the leftmost module, the propellant tanks and valves occupy the center, and the payload camera occupies the rightmost module.

The system has a CBE mass of 3.098 kg, increased to 3.264 kg with contingency. This translates to a 22.5% mass margin even under the most restrictive 3U CubeSat mass limit of 4 kg. The large mass margin validates the decision to focus on the volumetric efficiency of SPUD, rather than its mass efficiency, since the spacecraft has much more room to grow in mass than in volume. A full mass budget is shown in Appendix C.

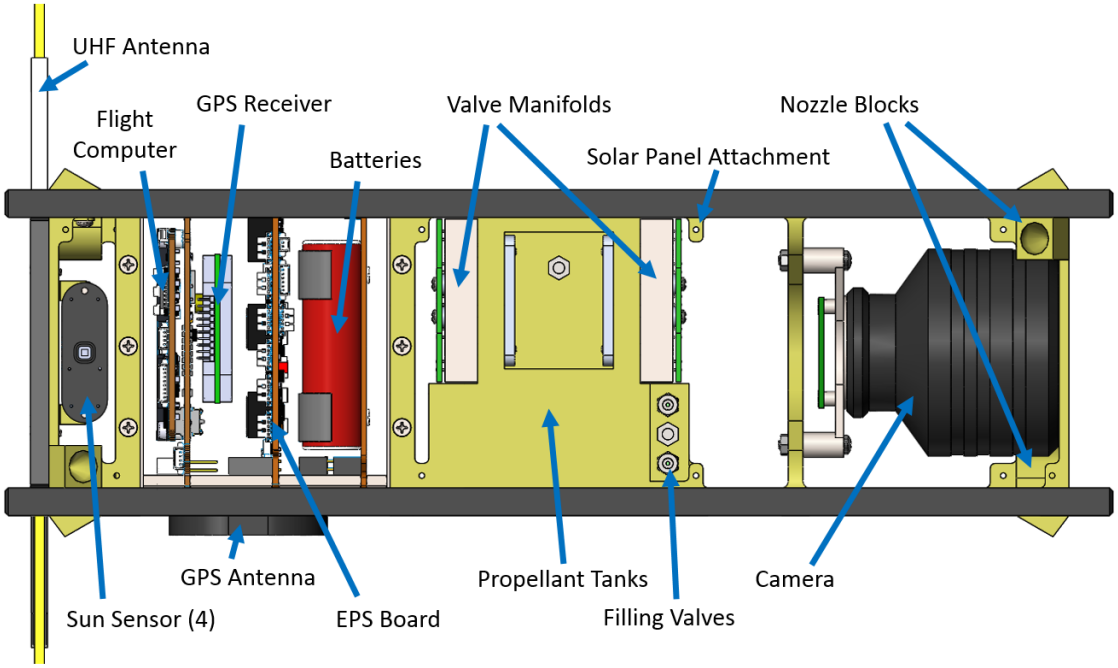

Figure 3.2: SPUD internal components.

3.2.1 Avionics

As with previous SSDL CubeSats, the avionics stack was designed to be integrated separately from the spacecraft so it could be tested in parallel with the propulsion system/structure. The avionics are COTS components, using the PC104 standard to maximize the number of compatible components. The stack is attached above and below to milled aluminum brackets with holes tapped for 4-40 helicoils. Printed clear holes in the structure align with these tapped holes, and the stack is secured to the structure with 20 fasteners, 10 on each bracket. The CubeSat rails on the -X face are narrowed to accommodate the stack and its brackets for installation, but such gaps are allowable under all three specs followed. The stack is shown separated from the structure in Figure 3.3, with the twenty fasteners removed from the structure. The avionics stack is oriented to place the batteries, the heaviest stack component, close to the center of mass to aid in balancing against the relatively low mass payload.

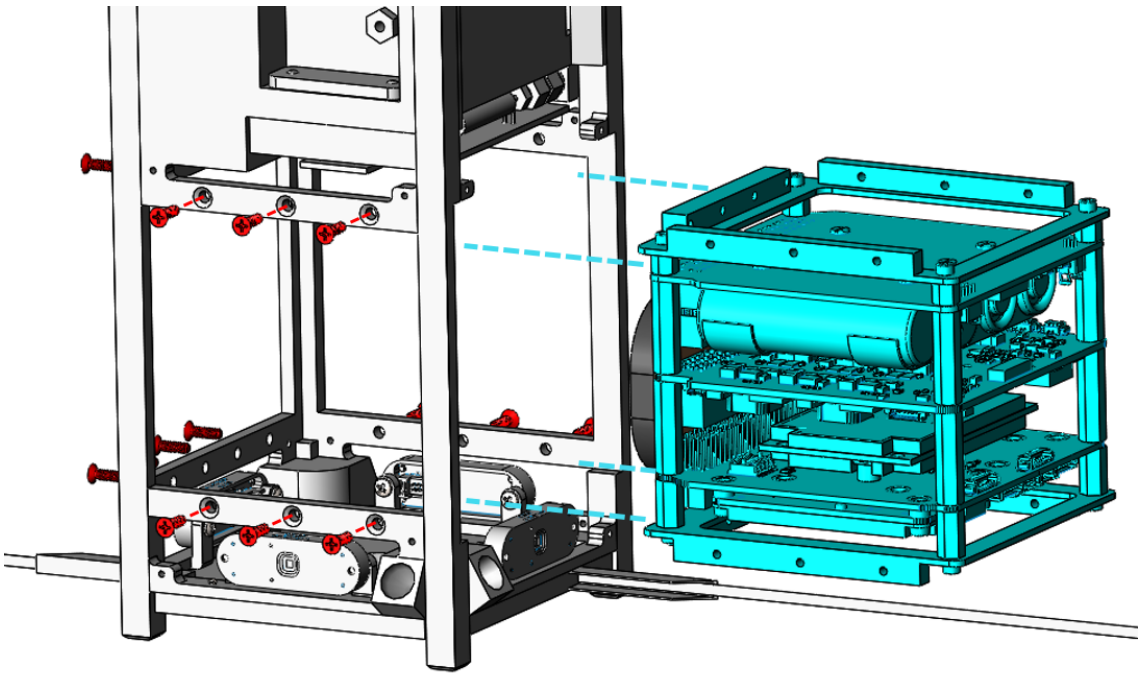

Figure 3.3: SPUD avionics stack (cyan) separated from the structure (gray) and stack fasteners (red).

3.2.2 Solar Panels

Similar to the avionics stack, the solar panels were designed conservatively to minimize complexity of the spacecraft. Four panels are mounted on the +/- X and Y faces, all four are body mounted with no deployables. However, the panels only extend 2.4 mm from the rail surface, well under the 6.5 mm allowed by the CubeSat spec, which allows room for deployable panels in future iterations of the design.

The cells are packed at a lower density than in previous missions, with no overlap between cells. This simplifies assembly of the panels and reduces the risk of damage, but also reduces power production. A total of only 21 cells are used, with no Z panels, and SPUD will have less electrical power than most comparable 3U CubeSats. However, power consumption will also be reduced. SPUD's ACS consists only of the thruster, which consumes an average of 80 mW. This is far less than the consumption of a reaction wheel/magnetorquer system, which was estimated at 2.5 Watts for similar pointing require-

ments. In total, SPUD is estimated to consume an average of 2.48 W when operating, a full power budget is shown in Appendix D. It will be capable of operating for 12 hours using its batteries alone, and will generate an average of 5 W when in sunlight. Properly oriented, it can generate a maximum of 8.4 W for faster charging.

3.2.3 Payload Bay

Approximately 1/3 of the satellite in the Z+ direction is devoted to the payload, with a 112.5 mm height in the Z direction. With the exception of the CubeSat rails and the two Z+ nozzle blocks, the volume is completely open for payloads, with 100 mm extents in X and Y. The printed structure can be modified to add supports for payload components to the structure. This was done in the SPUD reference mission to add supports for the imaging system. SPUD is designed with the separation switches on the -Z rail feet, but if the 3U+ "tuna can" volume is needed for the payload, the separation switches can be moved to the Z+ face to allow the tuna volume to be used there. This could be especially useful for a docking mission, since the docking mechanism could protrude beyond the rail feet. Such a mechanism has already been designed [62], and SPUD was designed to be compatible with it. The system requires 1/2 U (50 mm stack height) in addition to the tuna can, leaving 62 mm of addition volume for other payload.

3.2.4 Structure Simulations

Finite element analysis was performed to design the propellant tanks to the required factor of safety. As with BioSentinel, SPUD will be governed by NASA secondary payload regulations, and must be designed to 2.5X maximum expected operating pressure (MEOP). The maximum operating temperature will be 50ºC, giving a corresponding R-236fa saturation pressure of 584 kPa [37], and a required design pressure of 1460 kPa. The structure was simulated in Ansys AIM with 1460 kPa applied in both the main tank and plenum, resulting in a maximum von Mises stress of 20.1 MPa, well below the 230 MPa yield strength

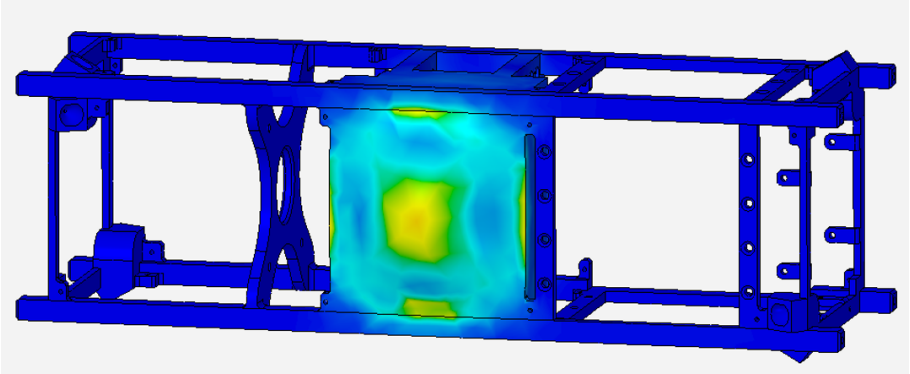

Figure 3.4: Von Mises stress plot of the structure under 2.5X MEOP.

of printed AlSi10Mg [63]. While this safety factor may seem excessive, the structure was designed to be adaptable to higher pressure propellants, such as ammonia, that could provide higher volumetric efficiency. Ammonia would be stored at 50ºC at a pressure of 2.034 MPa, requiring a rated pressure of 5.085 MPa, and increasing maximum von Mises stress to 70.8 MPa.

3.3 Propulsion System

The multifunctional nature of SPUD comes from the integration of its propulsion system with the structure. Printing the thruster within the structure confers three main benefits to the system. First, similar to the BioSentinel thruster, the use of 3D printing allows unusual geometries in the propellant tanks to maximize usage of the available volume. This advantage is inherent to any printed system. Integrating it within the structure also allows the propulsion system to share volume with necessary structure, such as the CubeSat rails. Hollow structural elements are desirable to lighten the structure, so using these hollow spaces as propellant pipes serves two functions. Finally, this allows the nozzles to be placed anywhere on the structure, since the piping can be run throughout the structure. This allows the nozzles to be placed far from the center of mass to increase torque, without requiring separate piping that would impinge on space available to the stack. The thruster tanks, valves, sensors, and electronics are all located near the center of the spacecraft. Placing the

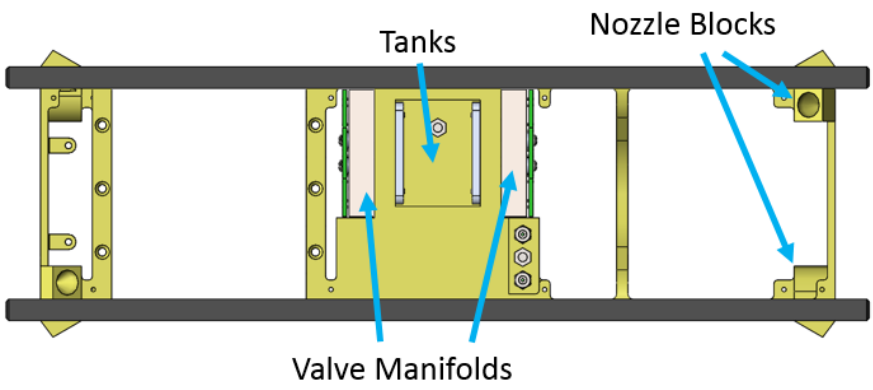

Figure 3.5: SPUD with only propulsion system components attached, showing propellant tanks and valve manifolds in the center and nozzles at the two ends.

propellant near the center of mass minimizes the amount of CM shifting that will occur as propellant is consumed. It also places the valves roughly equidistant from all nozzles, so that piping length is similar for all nozzles. Figure 3.5 shows a side view of SPUD with only propulsion system components shown. The propellant tanks and valve manifolds are in the center, with the nozzles located at either end.

R236fa has been selected as the propellant for SPUD, largely to draw on heritage from BioSentinel. The propellant is safe and has a low storage pressure, making it ideally suitable for a low-risk demonstration mission. R-236fa has also been demonstrated to be volatile enough to not leave residue on nearby surfaces. This is especially important for SPUD's inspection camera, which has a large lens that must remain clear for imaging the target.

3.3.1 Nozzle Geometry

There are eight nozzles on the SPUD structure which can be combined to give 6 independent degrees of freedom (3 rotational, 3 translational). The nozzle thrust directions are shown in Figure 3.6 on a preliminary SPUD structure. The left hand image shows all eight nozzle directions. The thrust vectors in blue are the four nozzles closest to the camera, and the vectors are angled away from the camera by 29º. The red vectors are on the far side of

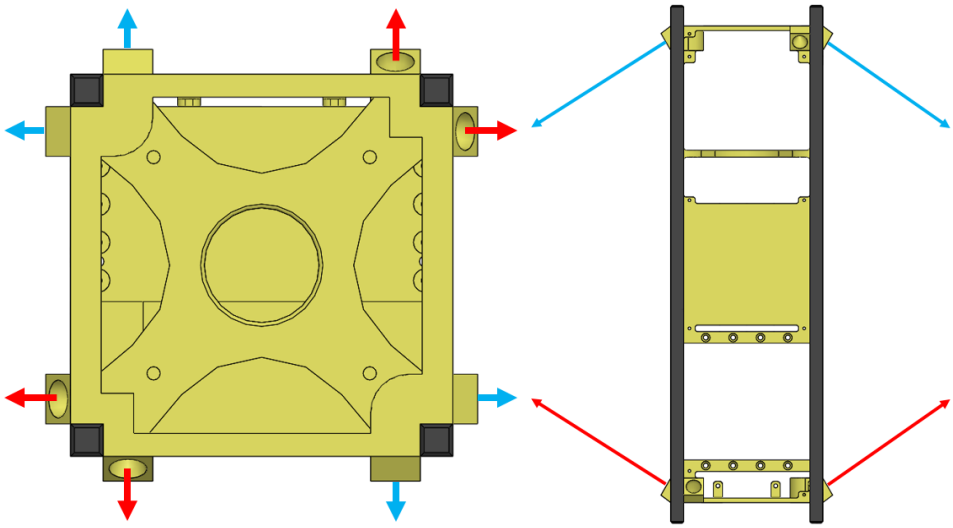

Figure 3.6: Thrust directions on a preliminary SPUD structure, shown from Z direction (left) and X direction (right).

the spacecraft, and are angled towards the camera by 29º. The image on the right shows the structure from the X direction, showing the 29º angle of the nozzles. This angle was determined through an optimization process described below.

The nozzles are located in pairs in four locations at diagonally opposite corners of the structure. The piping runs through the CubeSat rails to reach the nozzles. A closer view of two of these nozzle blocks is shown in Figure 3.7. The nozzles are angled within the blocks, pointing towards the X-Y plane at a 29º angle. The nozzle blocks protrude from the X and Y faces of the spacecraft by 6 mm, less than the maximum allowable protrusion of 6.5 mm in the CalPoly spec, which is the most restrictive of the three.

By using combinations of two or four of these nozzles, the spacecraft can rotate or translate on all three axes independently. These combinations are shown in Figure 3.8. These are balanced about the center of mass, so a translation maneuver will not lead to a rotation or an off-axis translation. Multiple maneuvers could be combined even if the nozzles overlap by duty cycling the nozzles. For example, a +X translation requires nozzles 2 and 7, and a -Y rotation requires nozzles 4 and 7. To combine these into a single maneuver, nozzles 2 and 4 would be operated at 50% duty cycle and nozzle 7 would be operated at

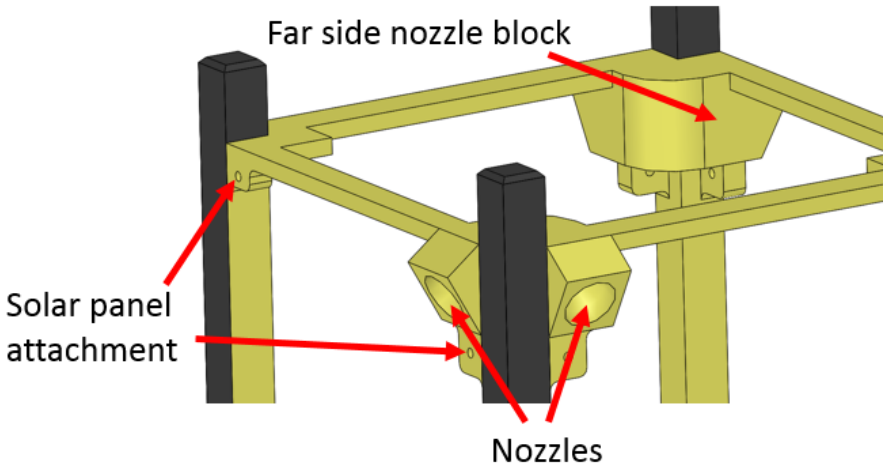

Figure 3.7: SPUD +Z end, showing two nozzle blocks at diagonal corners.

100%.

3.3.2 Propellant Tanks

As with BioSentinel, two propellant tanks are necessary, one main tank to store the propellant as a liquid/vapor mixture, and a plenum to expand the propellant into vapor before piping to the nozzles. There are two refill valves to repressurize the plenum, allowing a higher duty cycle and providing a backup in case of valve failure. If a single nozzle valve fails, the mission could potentially continue in a degraded operations mode. However, if there was only a single refill valve, its failure would end the mission, since all eight nozzles would be disabled. A schematic diagram of the tanks is shown in Figure3.9, with both propellant tanks, their sensors, and all 12 valves (10 solenoid, 2 filling).

The main tank has an internal volume of 262.5 cm^3. With a maximum operating temperature of 50ºC, and thus a minimum propellant liquid density of 1.27 kg/L, the tank can store up to 333 grams. The plenum has a volume of 98.1 cm^3, which allows approximately 6 seconds of continuous thruster operation before the plenum pressure drops to 80% of main tank pressure and must be refilled. Both tanks are instrumented for pressure and temperature so that propellant consumption can be monitored for mission planning and tank

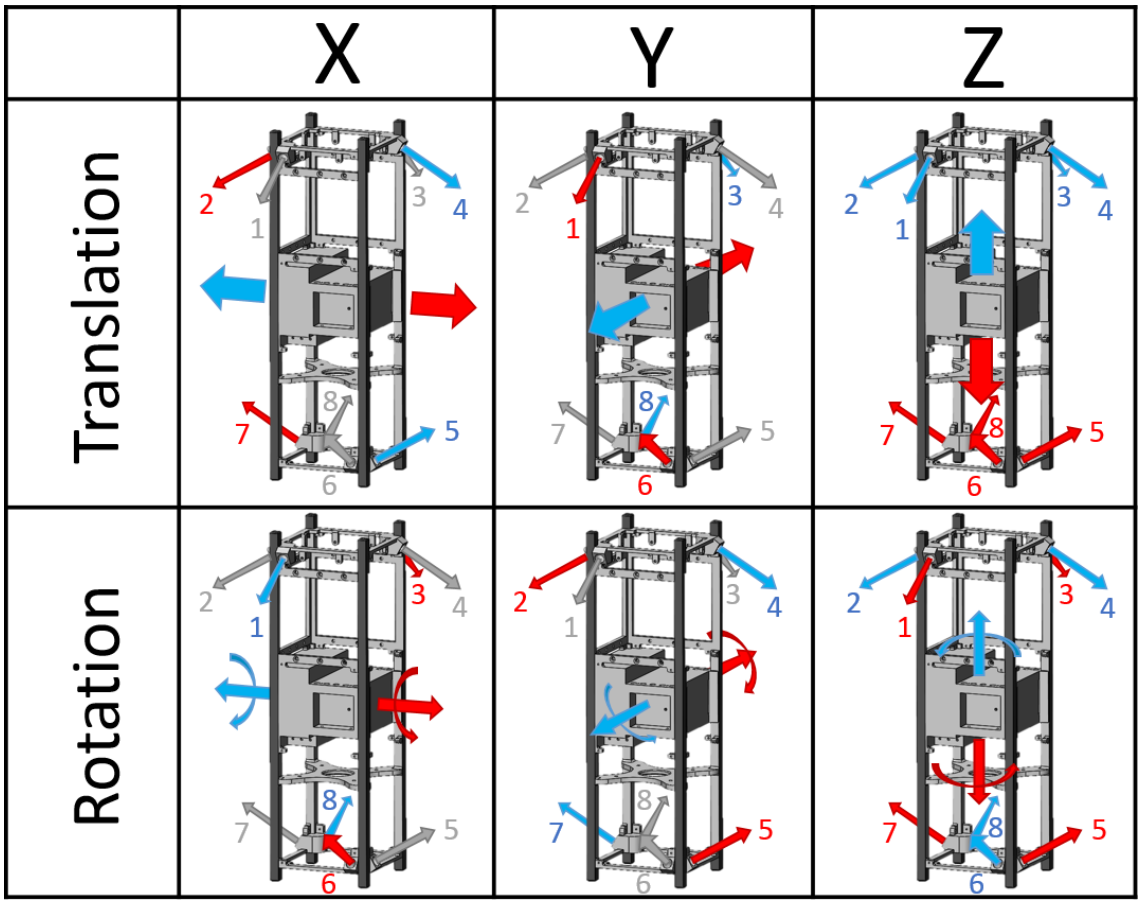

Figure 3.8: SPUD nozzle combinations to achieve each of the 6 degrees of freedom. Large arrows show direction of motion, small arrows show which nozzles must be used. Blue represents positive rotation/translation, orange represents negative.

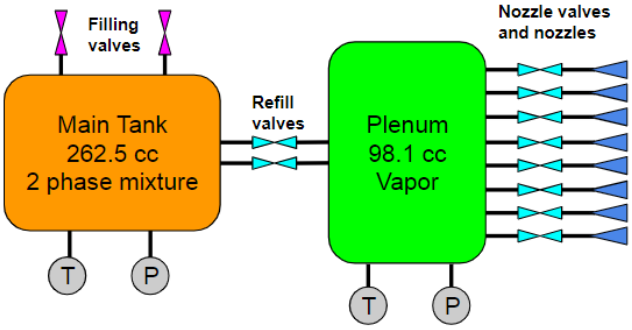

Figure 3.9: SPUD propulsion system schematic, purple valves are manual, cyan valves are solenoids.

refilling.

The tank geometry can be visualized more easily as a negative, shown in Figure 3.10. The printed structure and the negative are shown side-by-side from the same angle for comparison. The main tank and its connected piping are in orange, the plenum and connected piping are in green, and the nozzles and piping are in purple. The small cylinders in rows of five that terminate each pipe are the O-ring grooves that seal against the valve manifolds. This volume will be mostly filled by the O-rings, and is not counted towards the volume of each tank. The plenum is placed between the two valve manifolds for ease of access, since all ten valves connect to the plenum, and only two connect to the main tank.

3.3.3 Volumetric Efficiency

The volumetric efficiency of SPUD is more difficult to define than the efficiency of a modular thruster. A standalone system has a clear volume that it occupies within the spacecraft, but a multifunctional system is blended into the rest of the spacecraft, and cannot easily be separated. If the volume is taken to simply be the volume of the structure itself and the volume of all internal cavities (tanks and pipes), the system has a volume of 889 cm^3. However, this includes the volume of the CubeSat rails (required by the spec) as well as the supporting structure designed for the imager, the avionics stack, the sun sensors, and the solar panels, which should not be counted against the efficiency of the propulsion system. If these structural elements are excluded, leaving only the nozzle blocks and tank assembly, the volume occupied drops to 788 cm^3. This is the difference in volume between SPUD and a similar printed structure with identical avionics and payload, but no propulsion system.

Instead of using the exact volume of the system, the internal volume of the CubeSat that is not available to other system could instead be used. This is still relatively complicated to compute, however. The tank assembly (including sensors, fill ports, valves, and electronics) occupies 80 mm in the center of the satellite. This volume is completely unavailable to other systems, and if the volume is considered to extend to the edges of the CubeSat rails,

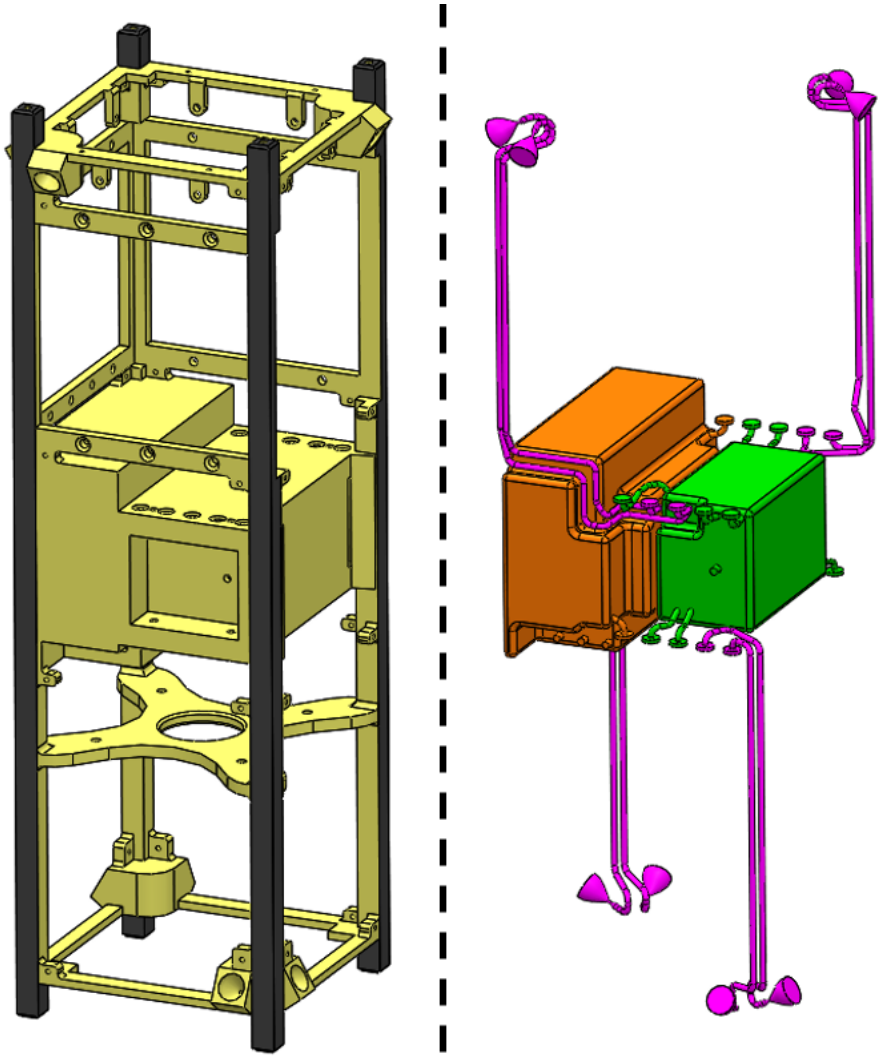

Figure 3.10: SPUD printed structure and negative from the same angle, showing main tank (orange), plenum (green) and nozzles (purple).

Table 3.1: Comparison of system volumetric efficiency between SPUD and modular thrusters. The range of efficiencies of SPUD reflect the range of possible volume interpretations.

	BioSentinel	Palomar	CNAPS	NanoProp	**SPUD**
Volume (cm^3)	890.4	1073.5	1575.0	1000.0	**829-889**
Nozzles	7	8	4	4	**8**
Impulse (N-s)	95.4	85	81.4	80.0	**125.6**
J_{vol} (N-s/L)	107	79	52	80	**141-151**

it occupies 800 cm^3. This does include some volume within the rails, but since that volume is used for propellant storage, it was counted towards the propulsion system. Adding the rectangular volume that the nozzle blocks occupy (the smallest rectangle that contains them) gives a propulsion system volume of 828.6 cm^3, which is the best representation of the volume an equivalent modular system would require. This gives a volumetric efficiency of 151 N-s/L. The more conservative "complete structure" estimate of 889 cm^3 gives an efficiency of 141.2 N-s/L. A comparison of this with the other propulsion systems from Table 2.4 is shown in Table 3.1.

SPUD has additional advantages not captured in this comparison. It provides 6-DOF control, balanced about the center of mass, and it has nozzles located as far from the CG as possible to maximize torque for rotational maneuvers. The large improvement of SPUD's volumetric efficiency over that of the BioSentinel thruster is due to several factors. As discussed previously, allowing the propulsion system to share volume with the structure improves volumetric efficiency, but the SPUD tank assembly is also a more efficient shape than the 4 cm wide rectangular solid of BioSentinel. The SPUD tank volume is closer to spherical than the BioSentinel volume, which reduces the volume share of the tank walls. SPUD is also printed from aluminum, which has a higher tensile strength than Bluestone, allowing thinner walls. Finally, the ability to tap aluminum allows sensors to thread directly into the structure, saving space that would otherwise be used for manifolds.

3.4 Manufacturing

Metal printed parts require post-processing before they are usable, and SPUD was designed to facilitate this processing. The structure was designed with a view towards its printing orientation and support structure, the inspection and testing of the part, removal of unmelted powder, machining of critical features, and corrosion resistance coatings.

3.4.1 Printing Orientation

In a powder bed AM printer, the orientation of a feature has a large impact on its surface quality. Faces located on the top (in the build direction) of solid metal are fully supported from below, and have a lower surface roughness and higher density. These faces are called "upskin". In contrast, faces on the underside of parts, called "downskin", have poor surface finish. During printing, these faces are supported from below by unmelted powder rather than solid metal. When the melt pool is created, some of the molten metal sinks into the powder, which decreases the part density near the surface and causes higher surface roughness. Downskin effects are worse at shallow angles where more of the layer is supported only by powder, and in very shallow angles it can cause the build to fail. At angles steeper than about 45°, downskin can be self-supporting and surface roughness is less severe. This geometry is shown in Figure 3.11. The part depicted in the figure would likely fail while printing the top section due to the shallowness of the downskin angle unless supports were printed below it.

Downskin is geometrically unavoidable, but there are steps that can be taken to reduce its negative effects. Printed supports can prevent the build from collapsing during printing, and also act as thermal pathways to reduce warping. These supports can then be removed with a mill after printing. Surfaces can also be designed with extra thickness to be machined away, removing the rough downskin surface to expose the higher density interior and provide a good surface finish. Critical exterior faces, such as the CubeSat rails, will

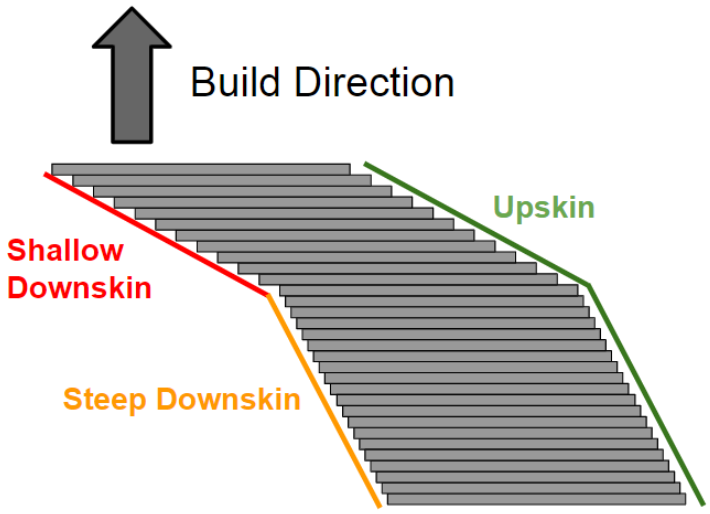

Figure 3.11: Illustration of three different surfaces in a part: upskin (green), steep downskin (yellow) and shallow downskin (red).

be printed oversized and machined down to the 100 mm spec. This will also provide a smoother surface for the anodization.

However, interior features may not be accessible for milling, meaning that any printed support material must be left inside the part, and the surface cannot be milled smooth. Any support material inside the tanks will reduce the volume available to the propellant, so a build orientation was chosen to eliminate the need for internal supports entirely. While the supports are useful for thermal load control, they are only absolutely necessary in two cases. The first is the shallow downskin discussed above, if the face is unsupported, it may collapse during printing, ruining the part. The second is when a local minimum is present. As the part is being printed, a local minimum's first appearance in a layer will be completely isolated from the rest of the part. The melt pool in that location would be completely unsupported, have no highly conductive thermal path available, and no way to maintain its location when the next layer of powder is spread, inevitably pulling the small layer away from its intended location. Because of this, all local minima in the design must be supported from below, and if a local minimum exists inside one of the propellant tanks, its supports cannot be removed. The local minimum problem is illustrated in Figure 3.12.

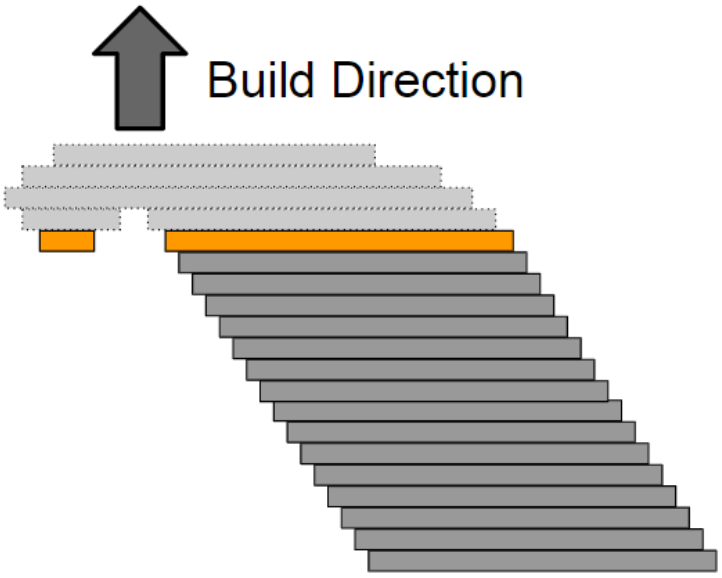

Figure 3.12: Illustration of local minimum problem. The dark gray layers are already printed, the light gray layers are not yet printed, and the orange layer is being printed.

The orange layer currently being printed will ultimately be part of the same component, but in this layer it is split into two separate pieces, one of which is unsupported.

SPUD was designed to be printed with a build direction 45º from the spacecraft Z axis, equally between the X and Y axes. The structure was designed such that all internal and inaccessible faces were free of local minima and were no shallower than 45º. While the interior of the propellant tanks will still have higher surface roughness than the exterior, since it cannot be milled, its walls will be self-supporting and free of support material. This build angle is illustrated in Figure 3.13, showing three cross sections at the printing angle, the red highlighted areas indicate the current printing layer.

3.4.2 Powder Removal

Powder bed printers lay down dense layers of powder across the entire build volume with each layer printed. After the part is complete, it is embedded in a dense block of powder. The powder can be easily wiped away from the outside, but the interior features must be designed to facilitate removing this densely packed powder. Completely enclosed volumes

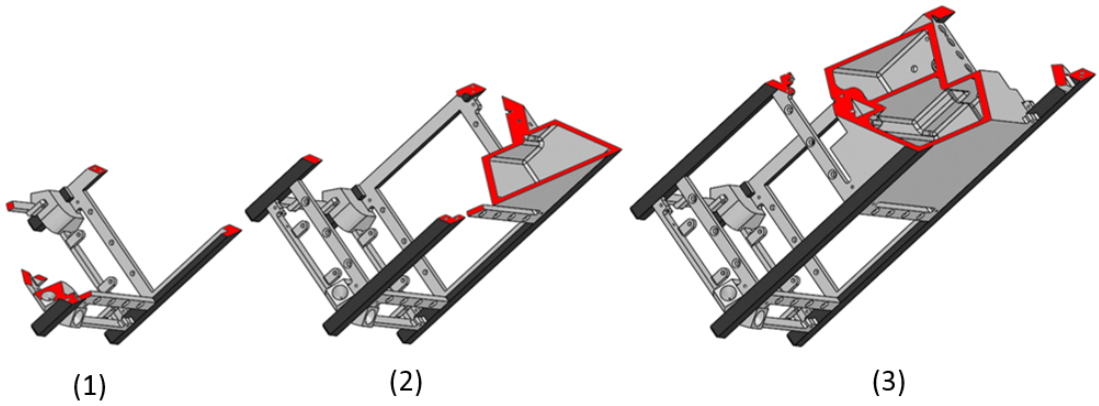

Figure 3.13: Three SPUD printing cross sections (red) at different build stages.

must be avoided for this reason, since powder removal will be impossible. SPUD's propellant tanks were designed with a total of six openings, two in the plenum and four in the main tank, in addition to the propellant piping. Each tank has two openings each for pressure and temperature sensors, and the main tank has two additional openings for fill valves. These openings were placed on opposing sides of the structure to facilitate cleaning the powder from the tanks. The piping can be cleaned with ethanol and compressed air to loosen the powder and drain it. The eight nozzles and their associated piping will be flushed "backwards" from the flow direction, with ethanol introduced into the nozzle and the powder drained back into the plenum and out of the sensor holes. This will minimize the amount of powder being forced through the throat of the nozzle during cleaning and avoid any possible erosion that would cause.

3.4.3 Inspectibility

An important factor in the design of any spacecraft component is inspectibility. All structural parts must be examined for defects that could compromise their strength, and this can be a challenge for printed parts [64]. Parts produced with conventional removal machining are inherently more inspectible than printed parts, since all machined faces must necessarily be exposed from some direction in order to be machined. The only way unobservable

defects could exist in a part is if they were present in the stock the part was produced from. A printed part, however, can have many areas that are obscured from outside inspection, such as the interior of propellant tanks. If the printing process introduces voids, which can be caused by insufficient powder density under the melt pool, the voids could potentially be undetectable.

The problem of detecting defects in a printed part is similar to the well-established problem of detecting defects in welded parts. CT scanning is typical in the inspection of welded parts, and has been used for printed parts as well [25]. SPUD will undergo CT scanning to detect voids and other defects after powder removal and before any other post-processing. In addition, a spare structure will undergo a burst test to validate the FEA results and increase confidence in the pressure vessel.

3.4.4 Machinability

SPUD was designed to minimize the complexity of the post-printing machining in order to reduce the cost of producing the structure. The majority of the features are designed to be usable with only minimal processing, although for cosmetic reasons the exterior will be all be sanded and polished if possible. In addition to the milling required to remove the external support material and reduce downskin roughness, some milling is necessary to meet required tolerances. The first features are the CubeSat rails, which have a specified tolerance of +/- 0.1 mm [4]. This tolerance is not realistic for such a large feature in the "raw" part, so the part will be printed 1 mm oversized on all sides, with 102 mm designed from rail to rail. This will then be milled down to 100 to achieve the 0,1 mm tolerance. The avionics module will also be milled to ensure a proper fit against the milled brackets, which are designed with 0.13 mm of clearance between the brackets and structure. The module will accessible to an end mill via the slots in the rails designed to fit the brackets. The interior faces in the avionics module will likewise be printed oversized, protruding into the module, and milled to the correct size. Finally, the nozzles themselves could possible

require machining. While previous printed nozzles have not had issues with deformation, large circular openings can have difficulty with droop, turning the cross section of the nozzle elliptical. If this happens, the nozzle will be returned to its correct shape on a CNC mill. Only the expanding section of the nozzle will be accessible for machining, however, the converging section's exact geometry is less important to the nozzle efficiency [47].

In addition to the milled surfaces, 41 holes in the structure must be tapped to accept helical inserts, since modern AM machines cannot print precisely enough to produce small threads. These holes will be printed slightly undersized, then drilled to the correct diameter and tapped with a mill. 31 of the holes are mounting points for the solar panels (2-56), 4 are for antenna connection (2-56), and the remaining six are for propellant tank sensors and filling valves (6-32, 10-32, and M3). All 41 holes are easily accessible from the outside.

Figure 3.14 shows the areas of SPUD that require machining after support and downskin removal. The CubeSat rails are in black, nozzle exit faces in red, and avionics module in cyan. Tapped holes are indicated with green arrows. All tapped holes are aligned with one of the three body axes, and the rails and avionics module will be machinable from those axes as well. The only surface that requires rotation is the nozzle exit plane, angled 29º from the X and Y faces. A four axis mill will be sufficient for all machining operations.

3.4.5 Structural Coating

After the structure is machined, protective coatings will be applied. In order to meet the CubeSat spec, the rails must be hard anodized to prevent marring when it is ejected from the rail pod. This coating can be applied to the AlSi10Mg alloy with the exact same process as any other aluminum alloy. A gold chromate alodine coating will be applied to the remainder of the structure for corrosion resistance, to protect it both in the humid pre-launch environment and against atomic oxygen damage in LEO. The chromate conversion coating is applied in a bath before any components are installed, so all internal faces will be coated as well. A typical alodine coating is less than 1 μm thick, so it will not change the tank

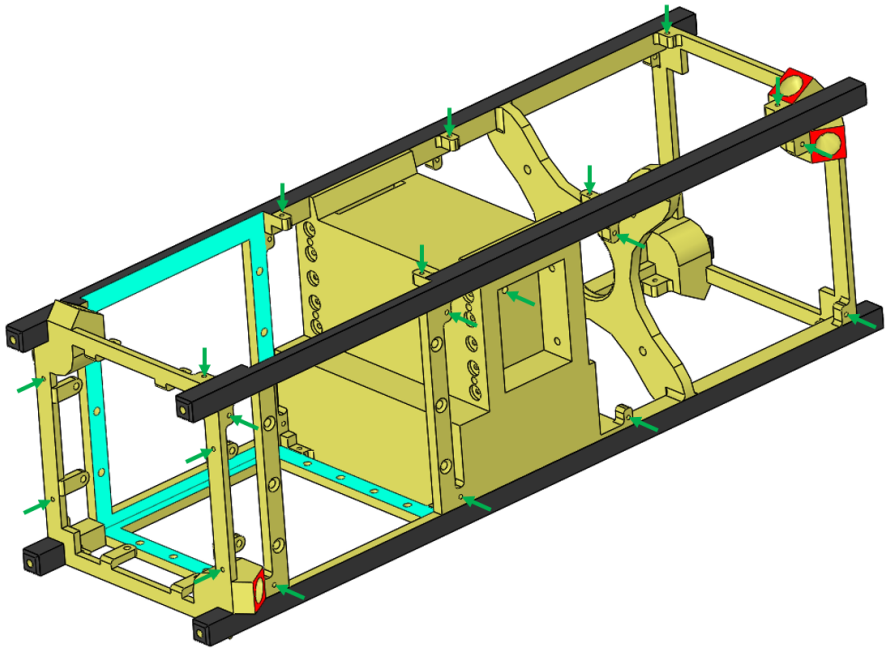

Figure 3.14: Required machining surfaces on SPUD.

volume or nozzle properties, and it is nonreactive with R-236fa.

3.5 Propulsion System Optimization

The nozzle geometry of SPUD is easily modified during the design process, which allows it to be optimized for a specific mission. As a case study, an inspector satellite mission was chosen, where SPUD must maneuver around a target object to specified points and take observations. The nozzle angles were optimized to reduce propellant consumption in this hypothetical mission. The nozzles were allowed to rotate through two angles, called the nozzle pitch (ϑ) and nozzle azimuth (φ), shown in Figure 3.15.

3.5.1 Trajectory

A representative inspector satellite trajectory was created for the optimization, in which SPUD must inspect exterior components of a small space station or crew capsule in low Earth orbit. In this scenario, SPUD must inspect the target from seven randomly chosen directions, 30 meters away from the target, then return to its starting position. SPUD was

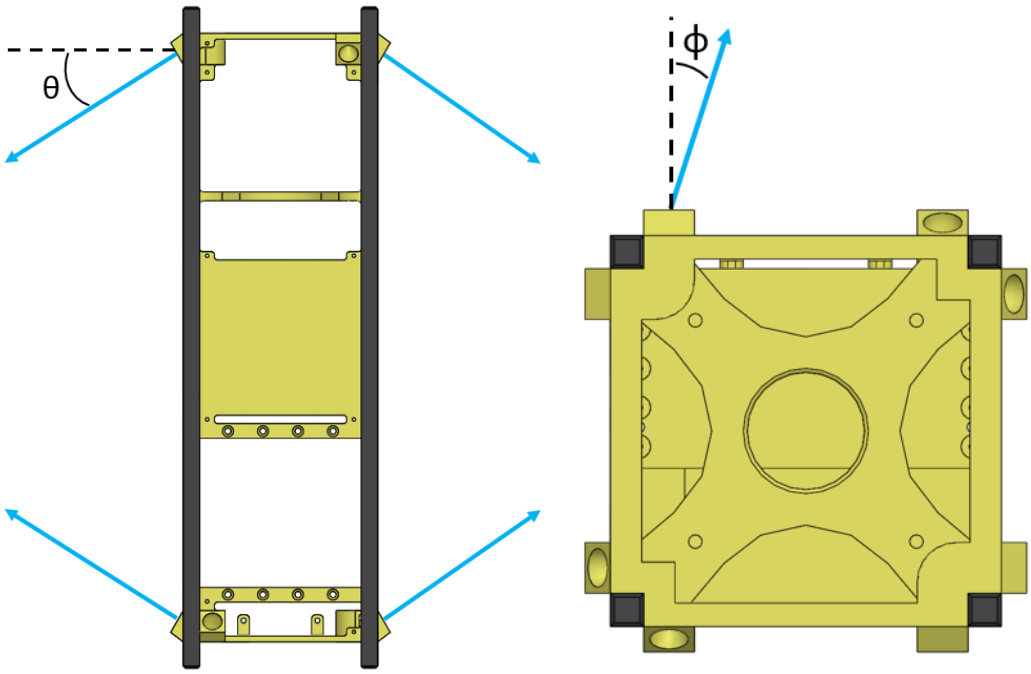

Figure 3.15: SPUD nozzle geometry to be optimized.

required to remain 30 meters from the target at all times and to maintain its z axis pointing towards the target at all times, since the reference design has an imaging system pointed in the z direction. SPUD was given 10 minutes to move between each observation location, and required to hold position at each location for 5 minutes. Position deviation was required to be less than 1 cm from the reference trajectory, and pointing deviation was required to be less than 0.5 degrees. The GPS unit baselined on SPUD is not capable of cm-level position fixing, and the sun sensors are not capable of sub-degree pointing. However, the mission only requires precise relative position and pointing, not absolute. Many algorithms exist to determine range and pose of a target of known geometry [65, 66], so a sufficiently detailed imager pointed at the target object can be used for relative attitude and position estimation.

The reference trajectory begins at the target location, with SPUD either docked or berthed to the target vehicle. SPUD travels directly away from the target towards the first observation point for 30 meters, then stops and holds that position for five minutes. Then SPUD follows a circular arc (centered on the target) to the next observation point, where

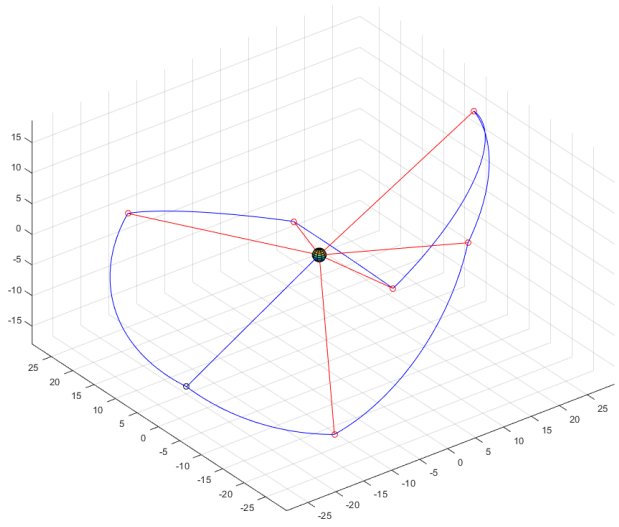

Figure 3.16: SPUD reference trajectory (blue) about a target object, represented here by a sphere at the origin. Red lines indicate observation angles, and circles indicate locations where SPUD must hold position and observe the target.

it waits for 5 minutes, repeating this for all seven observation points. Finally, it returns to the first observation point, then returns to the target location where it is captured by the larger vehicle. The 1-cm position accuracy of SPUD in this scenario is likely insufficient for docking with a CubeSat-scale mechanism, so the capture would have to be controlled by the target vehicle.

One example trajectory is shown in Figure 3.16. The blue lines show the trajectory of SPUD: departing the target, moving around it to the seven observation points, and returning to it. The red lines show the observation angles from the hold positions to the target. The true trajectory was allowed to deviate from the one shown in the figure by 0.01 meters, which is visually indistinguishable on this scale.

In this scenario, SPUD will need to perform inspection flights multiple times throughout the mission. Since the mission planners will not know ahead of time which locations must be inspected, the simulation was performed ten thousand times using randomly generated observation locations each time. Each set of observation points generated a different

trajectory, which generated different linear and angular impulse requirements. Optimizing SPUD to reduce the average mass required to carry out each of the ten thousand trajectories produces a nozzle configuration that is best able to efficiently carry out any observation mission, without being tailored to a specific set of observation points.

This scenario is somewhat unrealistic, since the reference trajectory is rigid and unable to take advantage of the natural relative motion of nearby objects in LEO to move between the observation positions more efficiently. It also ignores the likelihood that some locations will be of more interest than others and will be observed more often than others, although this is not expected to significantly change the final result. Finally it assumes perfect knowledge of relative position and attitude. However, the goal was simply to design a trajectory that exercised all six degrees of freedom of SPUD to demonstrate how the geometry of the structure can be tailored to a specific mission profile, and this trajectory was sufficient for that purpose.

3.5.2 Nozzle Efficiency

In order to optimize the nozzle angle, a nozzle efficiency metric was developed. Since the nozzles are angled, some component of the thrust vectors is "wasted", since it is directed opposite to some component of a different thrust vector. This is illustrated in Figure 3.17. In the figure, SPUD is performing a +Y translational maneuver using nozzles 3 and 8. Since the nozzles are angled towards each other, a component of each is lost (shown in red). Clearly, if θ is less than 45º, X and Y translational maneuvers will be favored over Z translational maneuvers, and vice versa.

This efficiency is expressed for translational maneuvers in Eq 3.1.

$$\eta_t = \frac{1}{n} \sum_{i}^{n} \hat{u}_{goal} \cdot \hat{u}_i \tag{3.1}$$

where η_t is the translational efficiency, n is the number of nozzles involved in the maneuvers, $\hat{u}_{goal}$ is the unit vector in the direction of desired thrust, and $\hat{u}_i$ is the unit vector

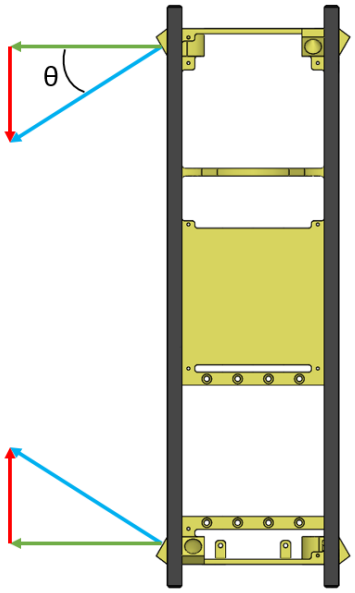

Figure 3.17: Illustration of nozzle inefficiency, SPUD is performing a +Y maneuver with two nozzles. Thrust vectors are shown in blue, with lost component of thrust in red.

in the thrust direction of nozzle i. The sum in Eq 3.1 is performed on every nozzle that is used for a given maneuver: 2 each for X and Y translations, and 4 for Z translations. An efficiency of 1 would represent nozzles that are perfectly aligned with the intended thrust direction.

A rotational efficiency can be similarly defined. This also depends on the location of the nozzles with respect to the center of mass. That efficiency is expressed in Eq 3.2.

$$\eta_r = \frac{1}{n} \sum_{i}^{n} (\hat{v}_i \times \hat{u}_i) \cdot \hat{u}_{goal} \tag{3.2}$$

where η_r is the rotational efficiency, and $\hat{v}_i$ is the unit vector from the center of mass towards the center of the nozzle exit plane. As before, this is summed over all nozzles used in the maneuver, 2 for X and Y rotations and 4 for Z rotations. An efficiency of 1 here represents nozzles that are aligned at a right angles to the vector from the center of mass to the nozzle. Note that this does not take into account the distance from the nozzle to the center of mass. Nozzles placed farther from the CM generate larger torque for the same propellant consumption, and in a sense they are more efficient. The η_r efficiency, however,

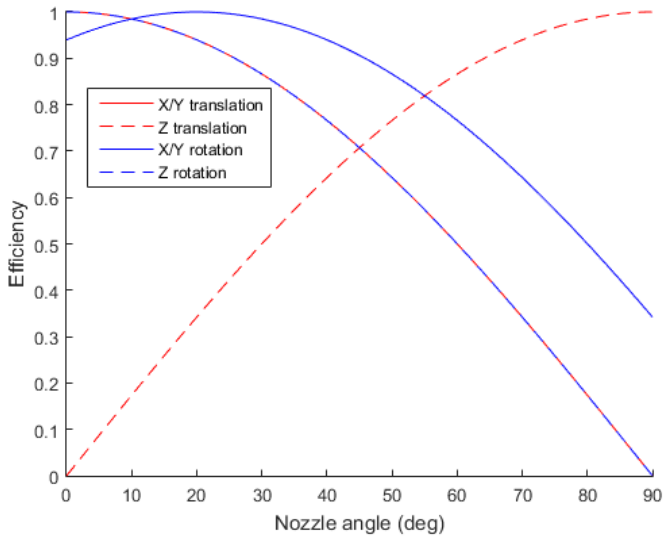

Figure 3.18: SPUD nozzle efficiencies against nozzle angle, note that the lines for X/Y translation and Z rotation are coincident.

is only designed to capture the efficiency due to angle, not location, so this is omitted.

The values of η_r and η_t using SPUD's nozzle locations are shown in Figure 3.18 for a nozzle pitch range of 0º to 90º with an azimuth of 0º, although pitch angles are only mechanically feasible from 0º to ~60º. The translational efficiency trades off relatively simply between X/Y and Z, crossing at 45º. The rotational efficiencies of X/Y and Z are closer, Z efficiency peaks at 0º and X/Y efficiency peaks at 20º. At large angles, X/Y translation and all rotations are relatively inefficient, and only Z translation is improved, so an angle below 45º is likely to the optimum.

3.5.3 Minimum Impulse Bit

The second important parameter of the propulsion system is the minimum impulse bit that it is capable of generating. Using data from BioSentinel and the thruster performance model, this was estimated to be 100 μN-s per nozzle when using R-236fa. Note that minimum impulse bit is not the same as the impulse resolution of the system. A single nozzle is not capable of producing less than 100 μN-s, but does not have to produce impulse in 100 μN-s increments, for example, it could produce a 120 μN-s impulse. This does raise the

possibility of generating a net impulse smaller than the minimum impulse bit by using opposing nozzles generating different impulses. Using the previous example, if the +X nozzles generated 100 μN-s and the -X nozzles generated 120 μN-s, the net impulse would be 20 μN-s. However, this is a highly inefficient way to generate impulse, and was not considered in this optimization.

A lower minimum impulse bit allows more precise maneuvers to be conducted. This is especially relevant for maintaining precise pointing. In the simple bang-bang controller implemented, SPUD is allowed to rotate within a cone centered on the SPUD-target vector with a half angle of 0.5º. The thrusters are used to prevent the Z axis from leaving this cone, so the ability to generate small impulses dictates the rate at which the thrusters must operate. A large minimum impulse bit would lead to faster movement within the cone as the thrusters overcorrect for drift. The minimum impulse bit for each axis can be found using the nozzle efficiencies above and the nozzle locations. These are:

$$J_{min} = \sum_{i}^{n} J_{min,nozzle}\eta_{t,i} \tag{3.3}$$

$$\Delta L_{min} = \sum_{i}^{n} J_{min,nozzle} r_i \eta_{r,i} \tag{3.4}$$

for translation and rotation, respectively. Here, J_{min} is the minimum impulse bit for a specific axis, $J_{min,nozzle}$ is the minimum impulse bit for an individual nozzle (100 μN-s), $\eta_{t,u}$ is the translational nozzle efficiency of nozzle i, r_i is the distance from nozzle i to the center of mass, and $\eta_{r,i}$ is the rotational efficiency of nozzle i. Note that the J r product in Eq 3.4 is scalar, not cross, since the misalignment term is already accounted for in η_r.

3.5.4 Propellant Consumption

Once a trajectory has been generated, the <X, Y, Z> components of linear impulse and angular impulse can be calculated simply as the sum of all translational and rotational

maneuvers multiplied by the mass and mass moment of inertia, respectively. These can be converted into propellant consumption using the efficiencies discussed above as well as specific impulse. For translational maneuvers, the propellant consumed is:

$$m_{prop} = \frac{J}{I_{sp} g \eta_t} \tag{3.5}$$

where J is the impulse required from that axis (sum of absolute values, counting positive and negative maneuvers), I_{sp} is the specific impulse, g is the standard sea level acceleration due to gravity, and η_t is the translational efficiency defined above. Rotational maneuver consumption is calculated with:

$$m_{prop} = \frac{\Delta L}{I_{sp} g \eta_r r} \tag{3.6}$$

where ΔL is the angular impulse (change in angular momentum L), η_r is the rotational efficiency defined above, and r is the distance from the CM to the nozzle. Note that this is a scalar product rather than a vector product, since the loss due to misalignment of the nozzle with the vector from the CM is already captured in η_r. Since $I_{sp} g$ is a uniform scale factor in both of these, the value used for I_{sp} will not affect the optimum nozzle angle. It is, however, necessary for estimating total propellant consumption for a reference mission. A conservative estimate of 40 seconds was used, based on BioSentinel results.

3.5.5 Angle Optimization

Ten thousand trajectories were generated, and each one was evaluated to determine the total fuel consumption for a range of nozzle pitches from 15º to 55º, and nozzle azimuth angles from -15º to 15º. The average propellant consumption was computed for each combination of pitch and azimuth, plotted in Figure 3.19.

The optimal nozzle angle was found to be a pitch of 29º and an azimuth of 3º. Since the azimuth found was close to 0º (i.e. nearly normal to the face of the spacecraft) the azimuth

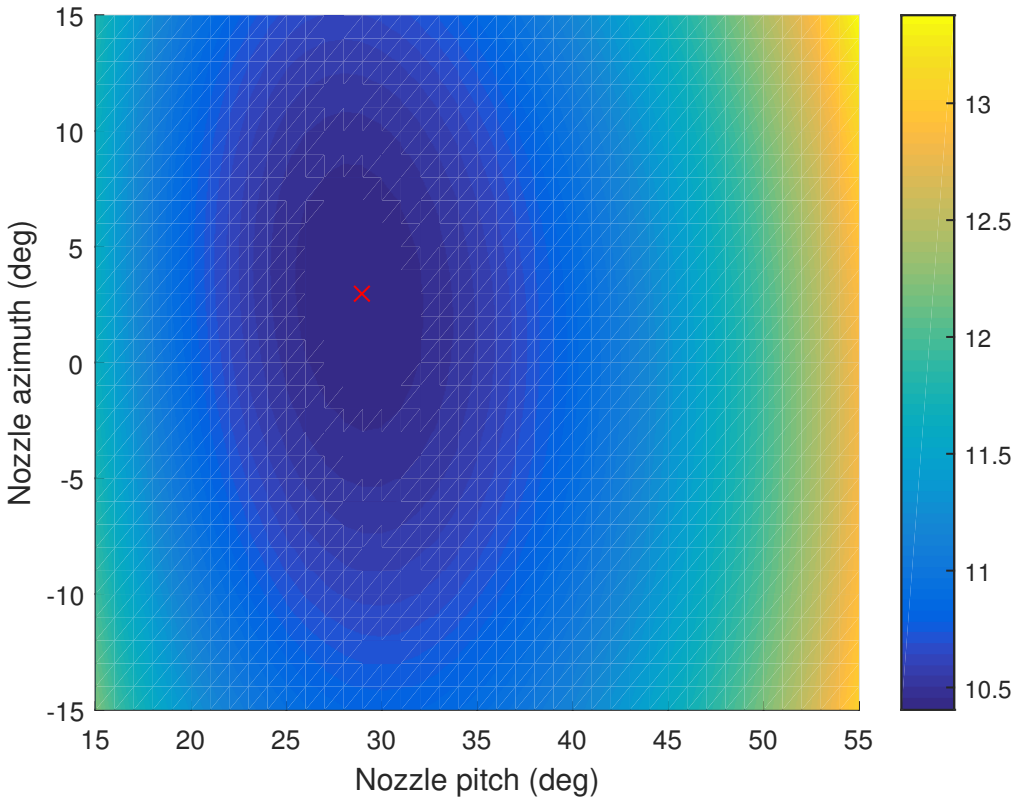

Figure 3.19: Plot of propellant consumption in grams for a range of nozzle pitch and azimuth angles, the red x indicates the minimum.

was reduced to zero. This was done in part to simplify post-process machining, since the tool must only be rotated about one axis to mill the nozzle exit face and expansion bell. With azimuth set to zero, the optimal pitch was still 29º, this change caused an increase in estimated propellant consumption from to 10.405 to 10.416 grams, a 0.11% increase, which was deemed acceptable.

3.5.6 Position Optimization

The position of the nozzles can also be optimized for a specific mission. The nozzle locations do not impact translational performance, as long as they are balanced about the center of mass, but they do affect rotation. Nozzles placed farther from the center of mass generate higher torque for the same propellant consumption. However, they also have a larger minimum angular impulse bit, which leads to a faster impulse rate during stationkeeping and thus a higher propellant consumption. Missions with tight pointing requirements and relatively few slew maneuvers could therefore benefit from nozzles placed closer to the center of mass, since stationkeeping propellant consumption would be greater than maneuvering consumption. At the opposite extreme, if a mission included miniature reaction wheels that could be used for fine pointing, the nozzles should be placed as far from the CM as possible.

In this simulation, SPUD only operated for 125 minutes, with a relatively relaxed pointing requirement of 0.5º, so stationkeeping propellant consumption was less than 1% of the total impulse requirements. The optimal nozzle location was therefore the maximum permissible distance from the CM, imposed by mechanical limits.

3.5.7 Maneuverability

With a completed CAD of SPUD, including fasteners and other hardware, as well as estimates for cables, the mass properties can be estimated with reasonable accuracy. Using performance estimates based on BioSentinel thruster data, the thruster was conservatively

Table 3.2: SPUD rotational maneuverability characteristics.

Axis	Torque (mN-m)	Accel. (rad/s^2)	Min Bit (mrad/s)	Momentum (N-m-s)
X	6.15	0.218	1.09	19.29
Y	6.15	0.220	1.10	19.29
Z	2.45	0.366	1.83	3.84

estimated to have a steady state thrust of 20 mN, a minimum impulse bit of 100 μN-s, and a specific impulse of 40s.

3.5.7 Rotation

Table 3.2 shows four important rotational maneuvering characteristics for each of the three axes. Torque and acceleration values given are the maximum possible with the nozzles operating at 100% duty cycle, which can only be sustained for roughly 4 seconds. Minimum bit refers to the smallest change in angular rate that can be achieved, and is most relevant when using the thrusters to hold a precise pointing vector, as discussed above. Total momentum refers to the total angular momentum that can be imparted if all propellant was consumed. This is most relevant if the thruster is being used to desaturate reaction wheels. A typical CubeSat reaction wheel is the 10 mN-m-s wheel from Sinclair Interplanetary [67], this could be desaturated roughly 1900 times in X or Y, and 380 times in Z. The shorter moment arm of the nozzles to the Z axis leads to substantially lower torque and total momentum than in X or Y, but the smaller Z axis moment of inertia, as well as the use of 4 nozzles instead of 2, leads to higher maximum acceleration and a larger minimum impulse bit.

The higher minimum bit in the Z axis means that with equal angular constraints applied to all 3 axes, the Z axis thrusters will need to operate more frequently. However, since the field of view of the camera is only controlled by the X and Y axis pointing (Z is rotation around the boresight), pointing requirements could potentially be relaxed for the Z axis without compromising observation ability. Sun sensor coverage is also symmetric about the Z axis, so coarse pointing ability is independent of Z. Although this scenario applied 0.5º

Table 3.3: SPUD translational maneuverability characteristics.

Axis	Thrust (mN)	Accel. (mm/s^2)	Min Velocity Bit ($\mu m/s$)	Total ΔV (m/s)
X	35.0	9.8	53.5	32.1
Y	35.0	9.8	53.5	32.1
Z	38.8	10.8	59.4	17.8

equally to all axes, an inspector satellite could potentially have no pointing requirements on Z at all, and simply have a maximum angular rate requirement to prevent streaking in the images.

3.5.7 Translation

Table 3.3 shows the corresponding parameters for translational maneuvers. As above, thrust and acceleration use a 100% duty cycle. Minimum velocity bit uses the dry mass (worst case for minimum impulse bit), while acceleration uses wet mass (also worst case). Total ΔV accounts for the changing mass of the spacecraft as propellant is consumed, and as above assumes all propellant is consumed to perform the maneuver.

Thrust, acceleration, and minimum velocity bit are similar in all three axes, indicating that stationkeeping ability is not strongly dependent on orientation. The X and Y axis translational efficiencies are slightly under twice the efficiency in Z, but four nozzles are used for Z, giving it slightly higher thrust. However, the lower Z efficiency leads to a lower ΔV, so large translational maneuvers should be aligned to take place in X or Y.

3.6 Conclusions

The multifunctional structure designed for SPUD offers many advantages for CubeSats requiring 6-DOF maneuverability within restrictive volume constraints. It was shown to have superior volumetric efficiency compared to a range of comparable propulsion systems, including the BioSentinel thruster, which was explicitly designed for volumetric efficiency. By routing piping through the rails, the maneuverability of the spacecraft can also be increased by locating the nozzles anywhere on the outside of the structure. Another advantage

of the 3D printed structure is the ease of tailoring the exact nozzle geometry to a specific task. SPUD was optimized for a set of inspector satellite trajectories, and the nozzle thrust vectors were aligned to minimize propellant consumption. The efficient use of the available CubeSat volume and the flexibility of its design give SPUD an advantage over more conventional structures by allowing more propellant to be stored in the same volume, as well as more efficient use of that propellant in a given mission.

CHAPTER 4

CUPID'S ARROW: VENUS PROBE WITH MULTIFUNCTIONAL STRUCTURE

The multifunctional structure technology has been extended to design a Venus atmospheric probe, called Cupid's Arrow. The probe is designed to fly through the atmosphere of Venus and perform in situ mass spectrometry to measure noble gas concentrations. In order to reduce the cost of the mission, it is designed to operate as a secondary payload, either on a dedicated Venus orbiter or a flyby mission. The spacecraft will use miniaturized electronics developed for deep space CubeSats and a miniaturized mass spectrometer. Volumetric efficiency is critical for secondary payloads, so a multifunctional structure was used to incorporate a propulsion system and atmospheric sampling system into the structure of the probe. This was used to reduce the overall size of the probe and improve its feasibility as a secondary payload.

4.1 Design Study

The Cupid's Arrow design study was done with the JPL Atelier design team. The author's specific contributions to the design study were in the design of the ACS propulsion systems, the atmospheric sampling system, and the design for additive manufacturing for the printed structural pieces.

4.2 Science Goals

Studying the differences in the evolution of Venus and Earth is crucial to understanding the evolution of the inner planets. Of particular interest is the history of the atmospheres of the two planets and their various sources and sinks, such as atmosphere escape, volcanism, and impacts. The concentrations of the volatile elements of the atmosphere are

governed by chemical processes that are difficult to observe. However, noble gases are unaffected by these chemical processes and can act as tracers for the physical processes that also govern the volatiles. Since these physical processes govern the addition and loss of mass into the atmosphere, noble gases can be used to build an atmospheric budget of sources and sinks. The isotopes of xenon are particularly useful in determining the relative importance of external sources such as solar input, comets, and chondritic asteroids [68]. By precisely measuring the concentrations of these isotopes, the physical processes can be better constrained and the history of Venus' atmosphere better understood.

The sample must be taken from below the homopause in order to ensure that it is representative of the atmosphere as a whole. The homopause is the altitude below which the atmosphere is well mixed, where diffusion processes are more significant than density-based fractionation. Below this altitude the different constituent gases all have roughly the same scale height, so their relative concentrations are approximately constant with altitude. Above the homopause, the scale heights of each gas become a function of density, so heavier gases will become depleted relative to lighter gases as altitude increases. Sampling above the homopause would thus yield a somewhat higher concentration of lighter isotopes than a well mixed sample. On Venus the homopause occurs at a minimum altitude of 119 km; Cupid's Arrow targets a sampling altitude of 110 km (roughly two scale heights below the homopause) in order to ensure a well mixed sample. Since the probe will be hypersonic throughout the flythrough, the atmospheric sample will be taken from the plasma sheath around the probe. This would prevent molecular concentrations from being measured, but does not affect the isotope ratios of noble gases.

4.2.1 Mass spectrometer

The noble gas measurements will be made with a miniaturized Quadrupole Ion Trap Mass Spectrometer (QITMS) developed at the Jet Propulsion Laboratory to measure noble gas isotopes ratios [69]. In particular, QITMS will measure the relative abundance of Neon,

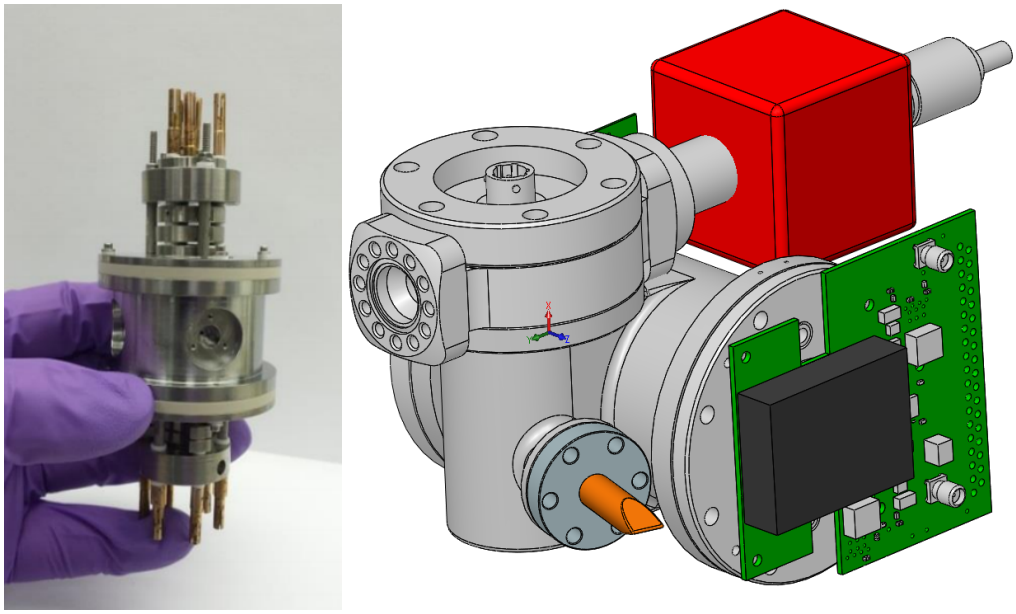

Figure 4.1: QITMS alone (left), and shown with supporting electronics, sample chamber, and ion trap (right).

Krypton, and Xenon isotopes with respect to ^{40}Argon. QITMS has a sealed chamber surrounding the mass spectrometer to contain the gas sample as it is being analyzed. This chamber can be filled in approximately 3 seconds, although the instrument requires roughly 1 hour to analyze the sample. The mass spectrometer is shown in Figure 4.1, both alone and with all of its supporting components. Together with the tank, ion trap, and electronics, the entire instrument is roughly 22.5 x 15 x 12 cm.

Because the miniaturized QITMS is not yet flight-proven, it is important to take several measurements of Venus's atmosphere in order to better characterize the instrument's noise level in flight. The mission is designed to maximize the number of samples that can be analyzed by conducting multiple atmospheric flythroughs and collecting multiple samples on each pass.

4.3 Trajectory

There are two possible mission profiles for Cupid's Arrow: freeflyer and secondary payload. In the freeflyer configuration, the spacecraft will perform the Earth-to-Venus cruise

alone. Launch can either be as a primary payload on a small launch vehicle, such as a Pegasus XL, or as a secondary payload on a geostationary transfer launch and perform its own Earth escape burn. After arriving at Venus, the spacecraft will perform its own insertion burn with a solid motor.

The same probe can be used in both configurations, with a detachable solid rocket motor used in the freeflyer configuration to perform the Venus insertion burn. In the secondary payload configuration the probe will fly to Venus attached to a larger Venus orbiter such as the proposed VOX mission [70]. The probe would be powered down for the cruise, and would be deployed by the orbiter once Venus insertion had been achieved. However, since no space agency has selected a suitable Venus orbiter that could deploy Cupid's Arrow, freeflyer is the nominal configuration. In both configurations, the probe must be capable of operating independently after arriving at Venus, so it must be a fully self-contained spacecraft with attitude control, power generation, propulsion, and communications.

In the freeflyer configuration the spacecraft will operate during the 430 day cruise to Venus in a low power standby mode. The trajectory was designed to minimize the ΔV required for orbit insertion. The probe will be spin stabilized during the cruise, with the backshell and solar panels pointed at the Sun and the spin axis precessing as it orbits to remain Sun-pointed. Periodic contact with the Deep Space Network will be used to verify spacecraft health, but no science will be performed during cruise.

4.3.1 Venus Orbit

Figure 4.2 shows the trajectory of the probe in freeflyer configuration after arrival at Venus. The probe begins on a hyperbolic trajectory (1) with an excess velocity of 2.7 km/s, and a 393 m/s Venus orbit insertion (VOI) burn is performed (2) to place Cupid's Arrow into a highly elliptical orbit (3) with a nominal period of 30 days and an inclination of 98°, chosen to minimize the amount of time the probe spends in Venus eclipse. Using a 3σ VOI ΔV error of ±6 m/s, the initial orbit period is expected to be between 580 and 915 hours, or 24.2

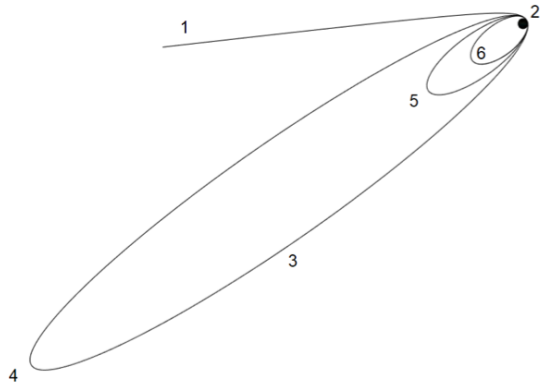

Figure 4.2: Cupid's Arrow trajectory after arriving at Venus.

to 38.1 days. In the secondary payload configuration, the VOI burn would be performed by the orbiter (e.g. VOX), and Cupid's Arrow would be deployed after the 30 day orbit was established. After this point, the two configurations would follow roughly the same trajectory.

At apoapsis (4), the cold gas thrusters are used to lower the periapsis from 250 km to 110 km, below the Venus homopause, with a maximum required ΔV of 0.90 m/s. The probe then performs its first flythrough (2) at a latitude of approximately 30° and collects four samples of the atmosphere. The velocity lost to drag results in a shorter period orbit of 13.3 to 240.5 hours. The large uncertainty in the orbit period is largely due to the uncertainty in the Venus atmosphere density at high altitudes [71]. A higher upper atmosphere density will lead to greater velocity losses during the pass, and thus a shorter final orbit.

At apoapsis (5), the thrusters are used to raise periapsis out of the atmosphere to 200 km, requiring a maximum ΔV of 9.10 m/s. Cupid's Arrow will remain in this orbit while it processes the collected samples, transmits the data to Earth, and recharges its batteries. Once this is complete, the probe again lowers its periapsis to 110 km and performs a second flythrough. The orbit is again reduced by atmospheric drag, with a final period between 5 and 27 hours. The periapsis is raised out of the atmosphere to 200 km (6) requiring a maximum ΔV of 18.12 m/s. As before, the probe will remain in this orbit to process and downlink the data from the second aeropass.

In the highest atmospheric density case (maximum velocity loss in the passes), there will not be sufficient propellant for a third aeropass, so the nominal mission will end after the data from the second pass has been downlinked. In the lowest density case the orbits will be longer and less ΔV will be required for the periapsis raise/lower maneuvers, so the spacecraft could potentially have enough propellant remaining for up to five total aeropasses. Since the probe has little science value after the aeropasses are complete and the data have been relayed to Earth, even a relatively risky flythrough could be attempted, such as one that might result in enough velocity loss to deorbit completely.

4.3.2 Venus Aeropass

Figure 4.3 shows a plot of probe altitude versus time during the first aeropass. The upper and lower bounds of the homopause are shown; the boundary varies from 119 to 138 km above ground level [71]. Since the probe will not have precise enough navigation during the aeropass to determine altitude, it will determine that it is at periapsis using the onboard accelerometer. Periapsis corresponds to the maximum atmospheric density, and thus maximum drag force. This measurement will likely be noisy due to turbulence around the heatshield, so the probe will need to spend enough time below the homopause for its navigation filter to determine that the periapsis has been reached, and give the command to begin sampling. In the shortest flythrough case with the minimum homopause altitude, the probe will spend approximately 95 seconds below the lower bound of the homopause (119 km). A total of 12 seconds are needed to collect all of the required gas samples, so even at the minimum homopause altitude there is sufficient time for all samples to be collected before the probe crosses back above 119 km.

4.4 System Architecture

Although it is not constrained by a deployment container, Cupid's Arrow shares with CubeSats a need to be as volumetrically efficient as possible. One of the possible mission pro-

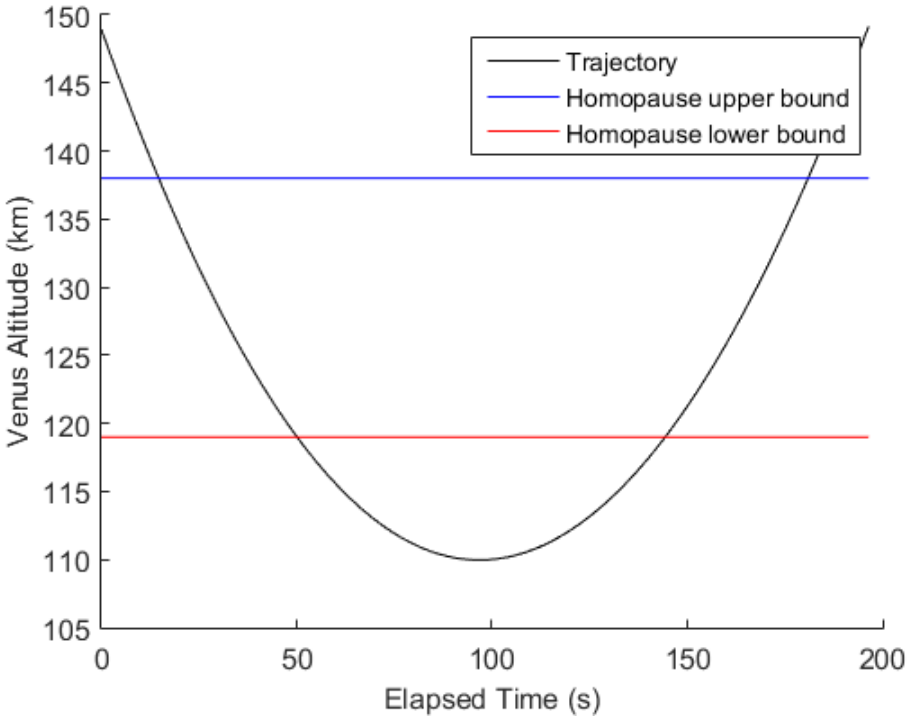

Figure 4.3: Plot of Cupid's Arrow altitude vs time with upper and lower bounds of homopause altitude.

files of the probe, discussed above, is to travel to Venus attached to a larger orbiter. A small probe has a greater chance of selection in this role, since it will be less of a burden on the primary mission. Additionally, if the probe's cross sectional area is reduced relative to its mass, the probe will experience less acceleration due to drag during the atmospheric flythrough. This will mean a loss of less orbital specific energy, and will reduce the ΔV required to raise and lower the periapsis.

In order to achieve this goal of a compact planetary probe, the majority of the structure of the probe will be 3D printed to take advantage of the more variable geometries that additive manufacturing allows. There are two printed metal pieces in the probe that together make up the internal structure, these pieces are called the "outer structure" and the "instrument tray". The probe was initially designed with a single printed piece forming the internal structure, but the post-processing and spacecraft integration procedures would have been far more complicated. The two printed components were designed to only interface mechanically and electrically with no pressure seals to simplify integration as much as possible. In addition to the two printed structural pieces there is a backshell made of a thin aluminum sheet which supports the antenna, solar cells, and attitude determination sensors. The major components of the spacecraft are shown in a horizontal exploded view in Figure 4.4.

Figure 4.5 shows a division of components between these structural pieces. The avionics and the mass spectrometer are attached to the instrument tray. These components, particularly the batteries, represent the highest density parts in the probe, so the instrument tray is located near the nose of the heatshield. This moves the CG towards the nose, which improves stability and allows the heatshield to be smaller. Placing all of the avionics on the instrument tray also allows the majority of the bus components to be integrated and tested on the instrument tray separate from the main structure. This is advantageous, since the electronics will be more difficult to access once the tray is inside the structure. Once testing is complete, the tray and avionics can be integrated into the outer structure as a single

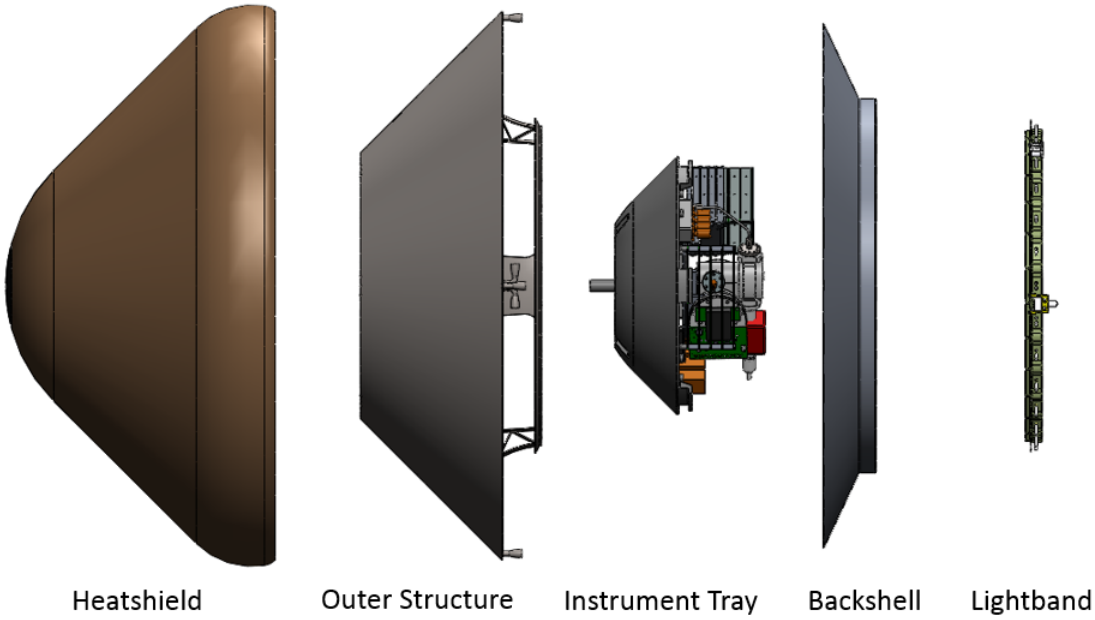

Figure 4.4: Exploded view of Cupid's Arrow, showing the heatshield, outer structure, instrument tray, backshell, and Lightband separation ring. The outer structure and instrument tray are 3D printed and multifunctional.

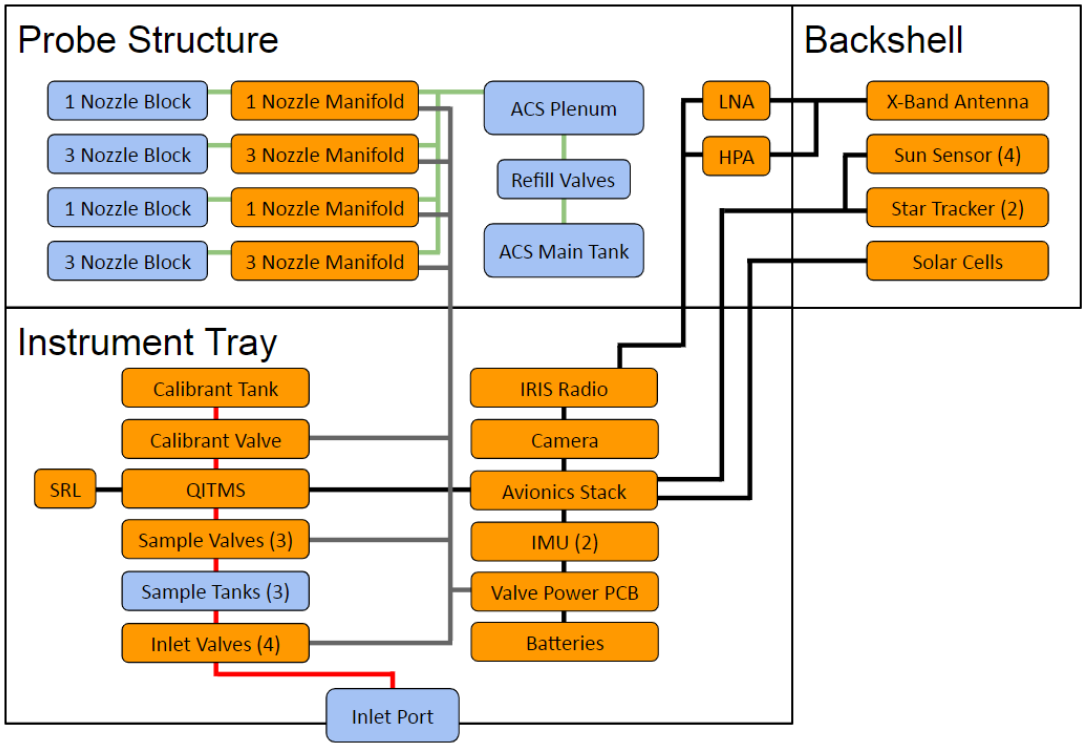

Figure 4.5: Cupid's Arrow component block diagram.

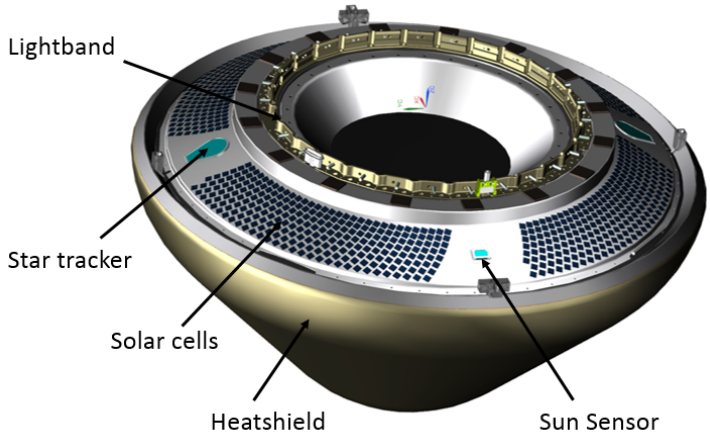

Figure 4.6: Cupid's Arrow exterior view, showing the backshell, Lightband, and attitude sensors.

piece.

There are two independent fluid paths within the probe: the ACS propellant and the atmospheric samples. These connections are shown in Figure 4.5 as green and red lines, respectively. Each fluid path is contained within a single structural component; the ACS propellant path is entirely within the outer structure, and the sample path is entirely within the instrument tray. This was done to simplify integration and testing, allowing each system to be tested individually for performance and leak rate before final integration.

The probe has an 18.25" Lightband separation ring at the aft end. In the nominal mission this would separate the probe from a "cruise stage" propulsion system after the propulsion system was used to perform the VOI burn. If Cupid's Arrow was instead carried to Venus as a secondary payload, it would be used to separate the probe from the mothership. Lightband was chosen because of its extensive heritage in secondary payload deployment and low remaining mass after deployment.

Figure 4.6 shows an exterior CAD rendering of the assembled spacecraft, showing the backshell with the solar cells and sensors, as well as the Lightband separation ring and heatshield. A section view is shown in 4.7.

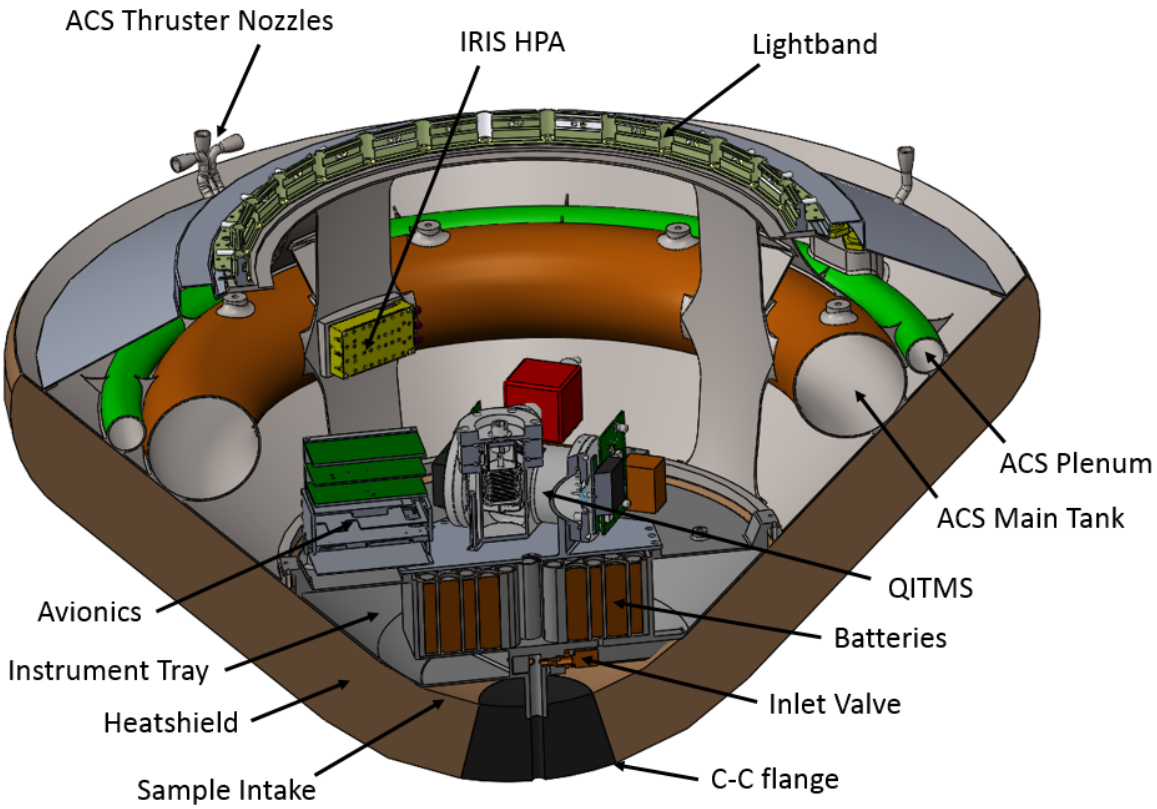

Figure 4.7: Cupid's Arrow cutaway view through plane of symmetry.

4.4.1 Heatshield

The heatshield is a 67 mm thick 45° sphere-cone bonded to the outer structure. The heatshield is made of PICA (Phenolic-Impregnated Carbon Ablator), an ablative ceramic that has been used in many reentry systems [72]. The heatshield has an overall diameter of 84 cm, and a nose radius of 25 cm. To ensure aerodynamic stability during the flythrough, the center of mass of the probe must be no farther than 3/8 of the overall diameter from the nose of the heatshield. In this case, it means that the CG must be within 31.5 cm of the nose. This requirement drove many design decisions, such as the placement of the batteries, as well as the overall size of the probe. A larger diameter probe can have a center of mass farther from the nose, since the CG requirement is based on overall diameter. The thickness of the heatshield was sized to allow a minimum of five passes through the atmosphere before erosion thinned the shield enough that the internal temperature would be too high for the electronics to survive. This was done to ensure sufficient heatshield thickness even in the most favorable case with five possible flythroughs.

The nose of the heatshield has a 10 mm hole for atmospheric sampling. The heatshield around this hole is not made from PICA, but instead is a carbon-carbon insert. Carbon-carbon, unlike PICA, is not ablative, so soot and debris from the eroding heatshield will not be swept into the inlet where it could contaminate the sample. The C-C insert is large enough that the stagnation point of the flow will be over the insert, and not PICA, as long as the probe's axis is within 10° of the flow direction. If possible, arcjet testing will be conducted on a model of the heatshield to verify that the flange is appropriately sized. The sample intake is part of the instrument tray and nests within the C-C insert. This setup is shown in Figure 4.8.

4.4.2 Backshell

The backshell is constructed from formed sheet metal rather than additive manufacturing. This is because the geometry is relatively simple, and the backshell only needs to support

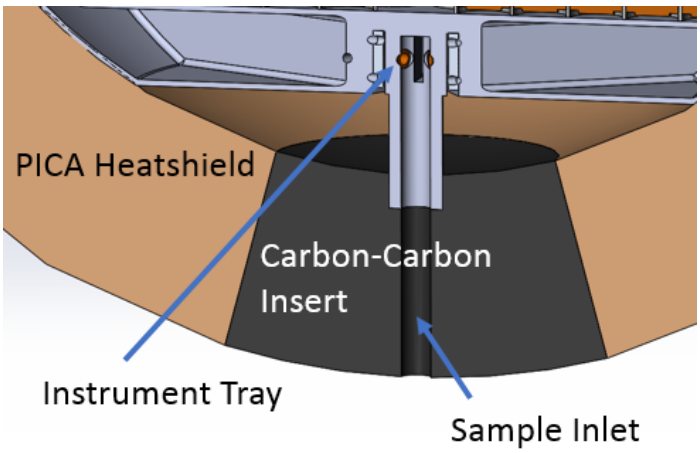

Figure 4.8: Cross section view of the sample intake, showing PICA heatshield (brown), C-C nose insert (black), and the base of the instrument tray (gray).

the solar cells and protect the internal subsystems from radiant heat during the flythrough. The shape of the backshell is a simple revolved membrane covering the aft section. This allows a thinner membrane than is possible to achieve with current additive technology, which reduces structural mass. This mass reduction is especially important for the backshell, since it is far from the nose of the probe. Mass on the backshell therefore has a relatively large impact on CG location, and reducing backshell mass improves stability.

The backshell carries the probe's solar cells and ADCS sensors: two sun sensors and one star tracker, protected behind IR-absorbing windows to reduce heat flux into the sensors. Finally, the backshell holds the X-band antennas, a circular array of patch antennas surrounding the Lightband ring. A close view of the backshell is shown in Figure 4.9.

4.4.3 Avionics

Cupid's Arrow will use the Sphinx CDH electronics developed by JPL for its interplanetary CubeSats. These are radiation tolerant electronics designed to survive deep space missions, fit within a CubeSat form factor, and have relatively low power consumption, making them ideal for the project. The Iris X band radio was chosen for similar reasons, it was also developed by JPL for interplanetary CubeSats and is the smallest available radio

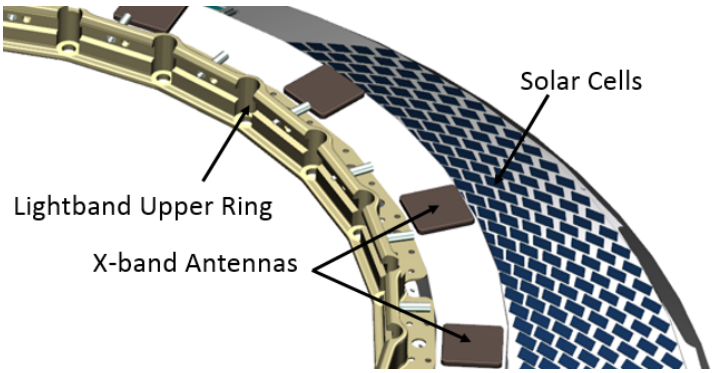

Figure 4.9: Close up view of backshell, showing solar cells and the X-band antennas surrounding the Lightband ring.

that can communicate to Earth from Venus. The low data rate available to the Iris (2500 bits per second) was a limiting factor in the trajectory design. The spacecraft will require roughly 13 hours to downlink the data from a single pass (4 samples). Since the DSN only allows communication for 8 hours, this means at least two DSN passes will be necessary to downlink the data from a single flythrough. The trajectory was therefore designed to include non-aeropass orbits between each aeropass, raising and lowering periapsis as described previously. This allows the probe to spend as much time between passes as required by DSN scheduling constraints.

Attitude determination is performed by two star trackers, two sun sensors, and an IMU. To eliminate the need for reaction wheels, the probe will be spin-stabilized for the majority of the mission, with the backshell and solar cells pointed towards the Sun. Attitude control will be provided by cold gas ACS thrusters, which will maintain the spin-stabilization and provide three axis control when not spin-stabilized. Three axis control consumes propellant at a higher rate than spin-stabilization, so this will only be used when the probe is reorienting itself, for example when conducting trajectory correction.

4.4.4 Power

Power is provided by solar panels on the backshell of the probe, capable of generating 54 Watts at 1 AU and 102 Watts at 0.782 AU, the aphelion distance of Venus. Ninety

rechargeable lithium-ion 18650 batteries provide 732 W-hr of usable energy, for use when the solar panels are not facing the Sun. Unlike most Earth-orbiting missions, the power storage requirement was not driven by eclipse time, as the probe will spend a maximum of six minutes in Venus eclipse due to the chosen orbit geometry. Instead it is driven by the data downlinks and atmospheric flythroughs. During flythrough the probe must orient itself and spin stabilize in the velocity direction. In this orientation the backshell will not be pointed towards the Sun, and the probe will run on battery power alone. Data downlinks to the DSN require the probe to point the backshell towards Earth. In some phases of the cruise, this could potentially cause the backshell to be completely shadowed by the rest of the probe. DSN passes can last up to 8 hours, and the Iris radio requires approximately 30 Watts when transmitting. Total expected power draw is 59.7 W while transmitting, potentially requiring 478 W-hr from the batteries.

The batteries are arranged in six packs of fifteen batteries each, wired in parallel sets of five to produce a nominally 18.5 V battery supply. The batteries are relatively dense compared to other components, so they are located near the nose of the spacecraft to help move the CG forward for stability. An electrical power system has been roughly sized to supply the maximum expected power draw, although components have not yet been selected.

4.5 Instrument Tray

The instrument tray is the first printed structural piece of Cupid's Arrow. It is printed from AlSi10Mg, an aluminum alloy optimized for additive manufacturing. The instrument tray experiences relatively light loads during launch, and the sample tanks will be stored at relatively low pressure, well below 1 atmosphere. Because of these light loads, the thickness of the instrument tray walls and other features is more limited by the minimum feature size of the printer than by the expected loads, and a strong material is not necessary. Aluminum was chosen for its low density to reduce the structural mass of the probe as well

as to reduce launch loads on the rest of the structure.

The instrument tray carries the probe electronics and the mass spectrometer, and also incorporates the atmospheric sampling system. It is designed to be integrated with the instrument and electronics outside of the main structure for ease of access during integration testing. Once this testing is complete it will be integrated into the outer structure with 18 machine screws, placed to ensure accessibility from the outside. The printed structure of the instrument tray is 2.74 kg, and the assembled tray including the instrument, batteries, and all avionics is 15.09 kg. The largest contributor to the instrument tray mass is the mass of the 90 lithium batteries.

Most of the electronics attach to the top of the instrument tray, where they will be easily accessible during integration and testing. The batteries are located in a "well" in the center of the instrument tray, covered by a machined metal plate that also supports the mass spectrometer. This arrangement puts the batteries, the densest components on the probe, as close to the nose as possible to improve stability. There are holes in the battery pack lid as well as the bottom of the instrument tray to allow wiring to reach the valves on the bottom of the tray. The avionics are attached to raised studs on the instrument tray as well as holes in the battery pack lid. An exploded view of the instrument tray is shown in Figure 4.10.

4.5.1 Sample Handling System

The atmospheric sampling system is incorporated into the structure of the instrument tray. Hollow spaces printed into the tray are used to store atmospheric gas trapped during the flythrough, which is then piped into the QITMS. This allows the QITMS to process a larger volume of gas than it can store in its own chamber, which allows better characterization of the noise level of the instrument and improves the science value of the mission. The sample handling system, including the inlet, valves, tanks, piping, QITMS, and calibrant gas tank, is completely contained within the instrument tray. All pressure seals that must be made as part of the sample system can be made before integrating the instrument tray into the outer

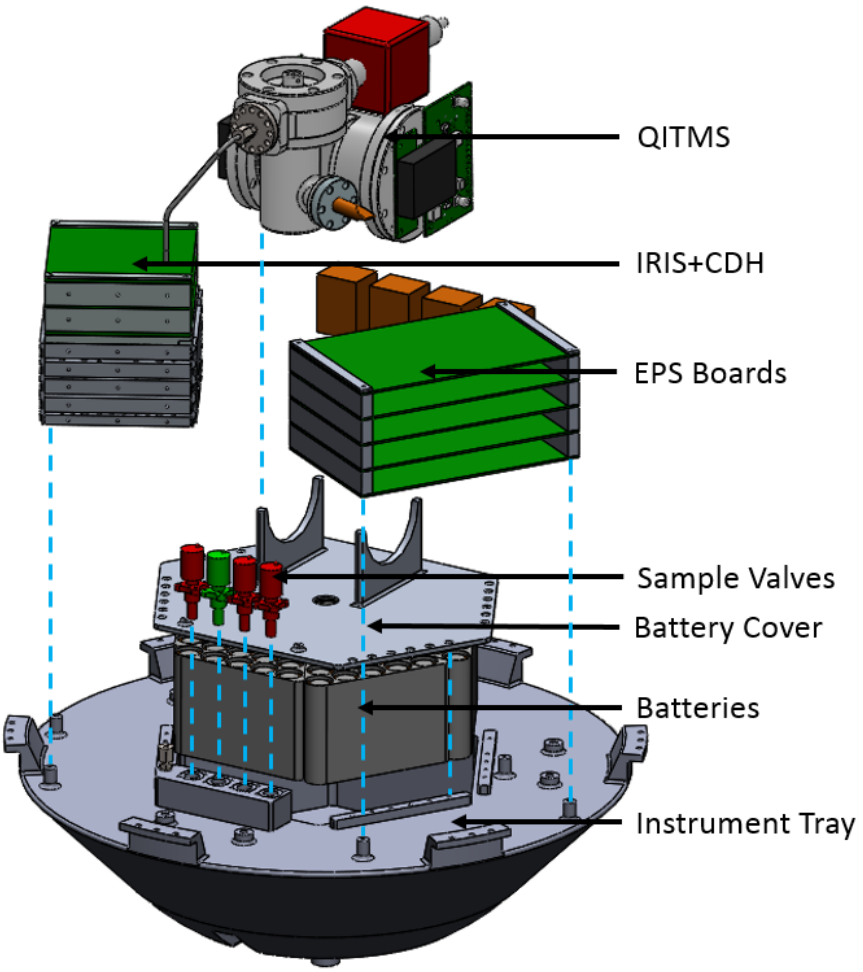

Figure 4.10: Z-axis exploded view of instrument tray components, dotted lines show connection locations.

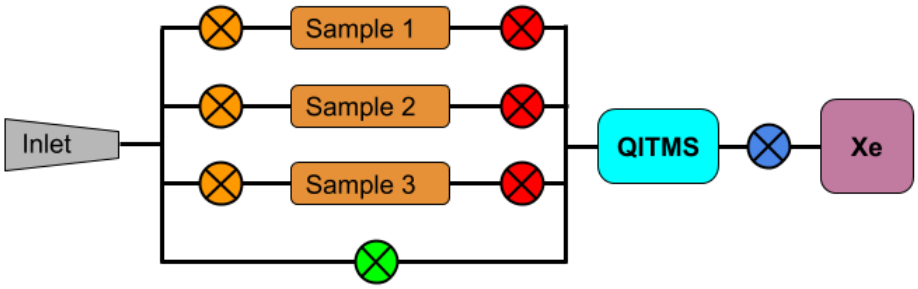

Figure 4.11: Cupid's Arrow sample handling schematic.

structure. This allows the leak checks and instrument testing to be conducted in parallel to the work on the outer structure, and allows easier access than a system inside the structure. Finally, there are no pressure seals that must be made between the instrument tray and the outer structure, which simplifies final spacecraft integration.

The inside of the tray is partitioned into three sealed compartments with a volume of 1 liter each, connected by printed piping and solenoid valves to the QITMS. A schematic of the tank arrangement is shown in Figure 4.11.

The accelerometer is monitored during the flythrough, and at the point of maximum acceleration (minimum altitude), the green and orange valves are opened in sequence for three seconds each to fill the QITMS and the three sample tanks. Once the probe has exited the atmosphere, it will spin stabilize with the backshell solar panels facing the Sun, to ensure the probe is power positive while the high power mass spectrometer is operating. The QITMS will then process the sample that it collected in its own chamber, which will then be vented to space through the green valve. A small amount of Xenon calibration gas will be injected into the instrument through the blue valve, then vented through the green valve once the calibration cycle is complete. The red valves are then used to refill the QITMS with the additional atmospheric samples from the instrument tray tanks. After each sample is processed, the QITMS is vented, then undergoes another calibration cycle. This allows the instrument to obtain four times as many samples compared to using the QITMS alone, with eight samples collected in the nominal mission of two flythroughs.

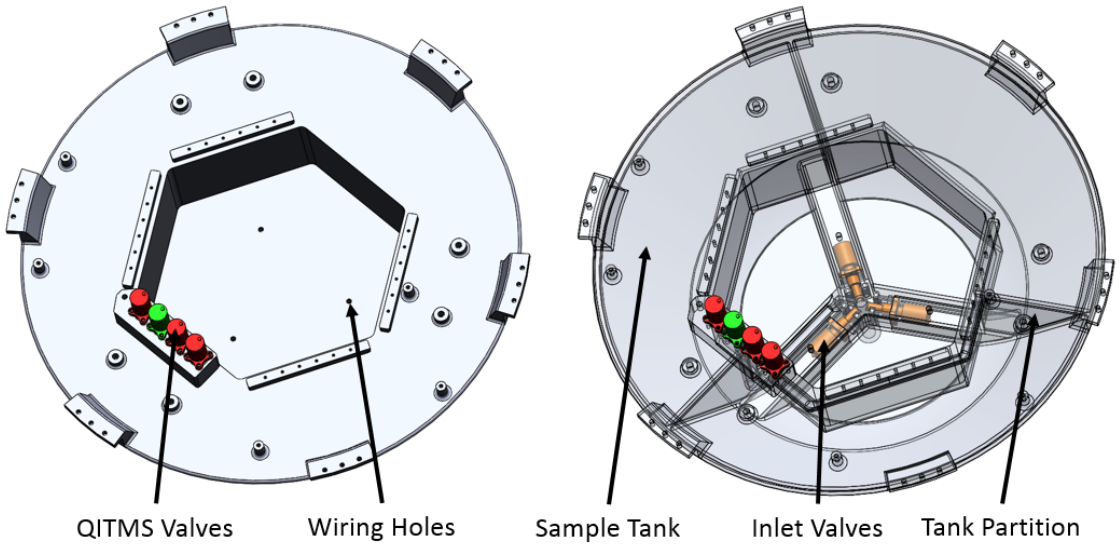

Figure 4.12: Sample handling system shown in a transparent tray (opaque view for reference). Valve coloration matches sample handling schematic.

The tank inlet valves (orange) are located on the bottom of the instrument tray, closest to the nose, arranged radially around the inlet itself. Each tank is also connected to the output valve manifold (red and green valves), which connects to the QITMS. Both manifolds are part of the printed structure of the instrument tray and are not integrated separately. The inlet is connected via internal piping to the three inlet valves, and also has a direct connection to the output manifold to allow the instrument to sample from the inlet directly via the green valve. This arrangement is shown in Figure 4.12. All components aside from the valves have been hidden for clarity, and the instrument tray itself has been made transparent. The valve coloration follows the same convention as the schematic.

An effort was made to minimize the complexity of the piping that the sample gas must flow through. The sampling valves are adjacent to their associated tanks, so the output of each valve goes directly into its tank. The output manifold is placed such that it covers two of the three tanks, so that two of the output valves can draw directly from their corresponding tank without a long printed pipe. The third tank has a pipe connecting it to the output manifold, located along the corner of its adjacent tank to minimize the amount of material needed to form the pipe walls. A second pipe directly connects the inlet to the output valve

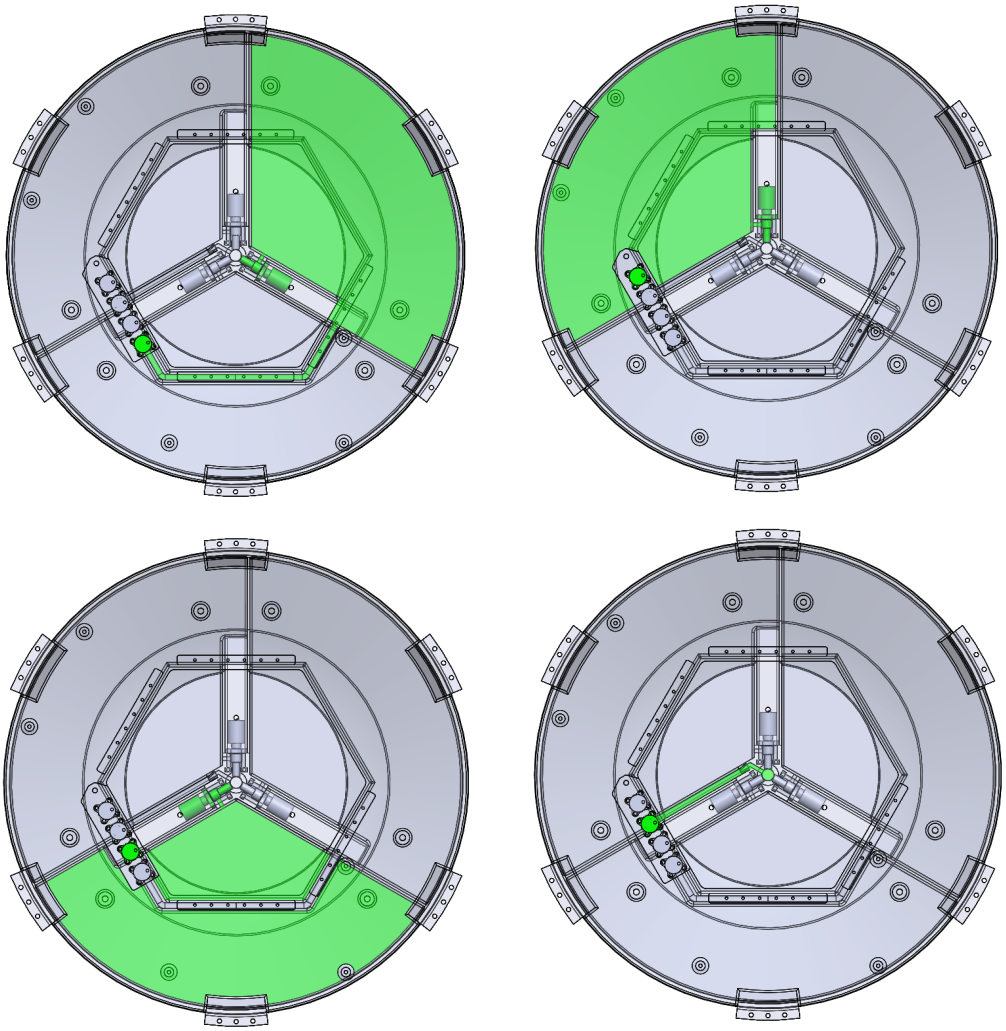

Figure 4.13: Tank filling diagrams, highlighting the tank area, associated valves, and piping. Lower right quadrant shows direct sampling into the QITMS.

manifold, also located along the corner of a tank. The tank geometries are illustrated in Figure 4.13, showing four top down views of the instrument tray. The first three views highlight the different tanks as well as their associated valves and piping. The fourth shows the direct QITMS sampling valve and its piping.

Using the hollow space in the instrument tray allows the tanks to store more volume of sample gas than would be realistic with conventionally produced parts. The instrument tray conforms to the inside shape of the heatshield, occupying the entire available volume in the nose of the probe. The placement of the tanks in the volumes around the batteries

allows this volume to be used efficiently, since it takes up space that would otherwise be unused due to packing inefficiency.

4.5.2 Avionics Attachment

The avionics are attached to the instrument tray via raised studs with internal threads. These studs are printed onto the top face of the instrument tray, but they are not printed with holes since the tolerance on hole location is likely to be tighter than what can be achieved by printing. The studs will be drilled with blind holes and tapped so that the PCB stacks can be attached to them via standoffs. Both of the PCB stacks overlap the battery tray lid, so they are connected both directly to the instrument tray and to the battery lid. The battery lid is a simple hexagonal plate to cover the battery well, and will be machined from aluminum stock.

4.5.3 Outer Structure Attachment

The instrument tray is attached to the outer structure via six tabs at the perimeter of the tray. Each tab has holes for 3 6-32 UNC fasteners, which thread into holes in the outer structure. The tabs are sized to give the instrument tray an outer diameter of 410 mm. The outer structure has an upper ring inner diameter of 414 mm, giving 2 mm of clearance around the instrument tray when it is lowered into the structure. Since it is installed from the aft end of the outer structure, the instrument tray can be installed or removed even after the heatshield is bonded onto the outer structure. The heatshield will be difficult or impossible to remove after installation, so the ability to remove the instrument tray (for example, to investigate avionics issues) after heatshield installation is necessary for integration troubleshooting.

The fasteners are MilSpec A286 high strength steel, each rated for 1250 lbs (5560 N). The eighteen fasteners were sized based on expected vibration loads during launch. The location of the fasteners was chosen to ensure that they would be accessible for a torque wrench with a long ball-end bit from the aft ring of the outer structure. The holes in the

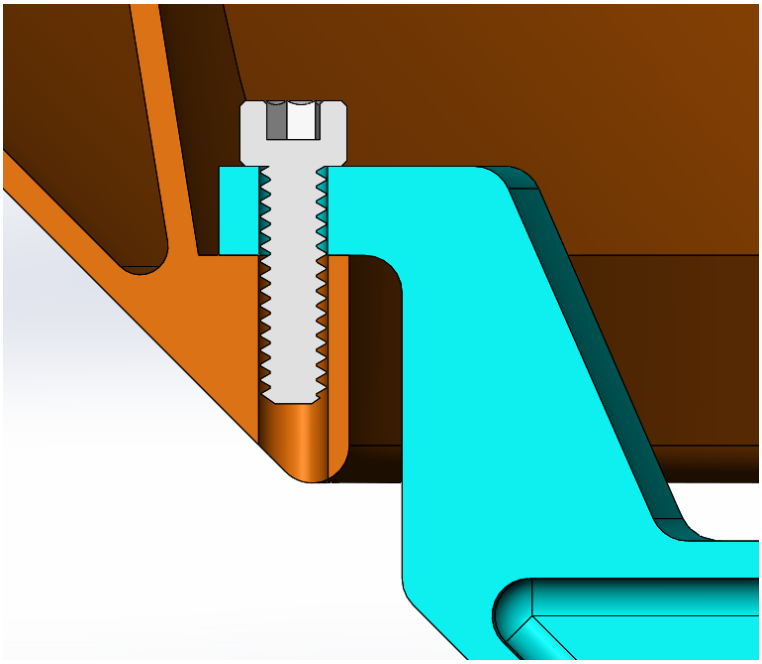

Figure 4.14: Cross section of mounting system between the instrument tray (cyan) and outer structure (orange).

outer structure will be tapped through from below to accept a locking helical insert for the fasteners to thread into. A cross section of the mounting scheme is shown in Figure 4.14.

4.5.4 Inspectibility

An important factor in the design of the two AM components was ensuring that they could be inspected for defects after printing. As an interplanetary probe, all components onboard Cupid's Arrow will be subject to detailed inspection and verification campaigns, and the printed metal parts will require even more verification [64]. Machined metal parts are inherently easier to inspect than printed parts, since all machined faces must necessarily be exposed from some direction in order to be machined. A printed part, on the other hand, can easily have features that are partially or almost fully enclosed. Since the part cannot be easily inspected during the build process, some method must be devised to inspect these features after printing. In addition, the printing process can introduce voids and other flaws inside the material. This is most commonly the result of shallow angle features, discussed

below, and can also occur when the geometry of the part disrupts the process of laying down more powder in the print volume.

Since locating voids in a metal part is also a necessary inspection step for welding, printed parts can be inspected in the same way. CT scanning has been successfully used to locate defects in printed metal parts for spacecraft [25], and will be used to inspect the interior features of the Cupid's Arrow structure, such as the instrument tray sample tanks. In addition, the sample tanks were designed to be observable through an endoscope via the six powder removal holes. This will allow a cursory visual inspection before the CT scanning, which is comparatively more expensive and time-consuming. If serious flaws are detected in the visual inspection, the CT scanning will be unnecessary.

4.5.5 Print orientation

The instrument tray was designed to avoid shallow overhanging angles to reduce roughness caused by downskin and to reduce the number of supports needed. As a rule of thumb, no structure can overhang at a shallower angle than 45° without requiring supporting structure. Exterior faces, even at steeper angles than 45°, will still have periodic supports printed for thermal relief to reduce warping in the final part. The instrument tray will be printed with the top face inclined at a 45° angle to the build plane. This orientation, along with the internal geometry of the tanks, avoids any interior faces at shallower angles than 45°, which reduces the interior roughness caused by downskin and greatly reduces the number of support structures in the interior of the tanks. The curved exterior face on the bottom of the instrument tray does have a large region that will be printed shallower than 45°, requiring machining to smooth the surface, as discussed below.

Since the battery tray sinks into the instrument tray tanks, there will be one location inside the structure that is a local minimum, and thus requires internal support structure. As the part is built up layer by layer, any local minima in the part would appear isolated in the first layer in which it exists, which is not possible with current additive manufacturing

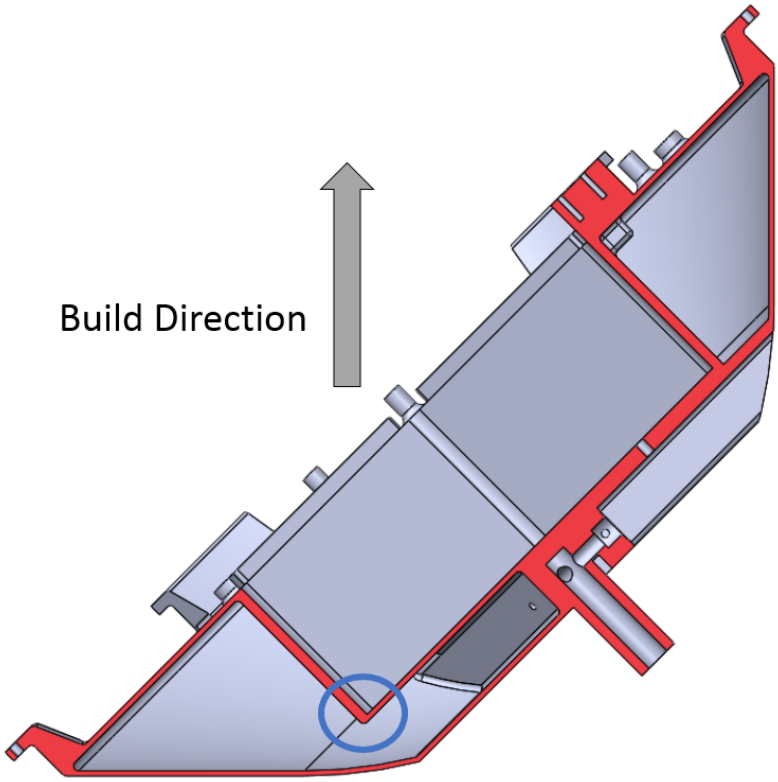

Figure 4.15: Cross section of the instrument tray, showing build orientation. Red highlighted areas show the cross sectioned areas, blue circle shows the local minimum that requires support.

technology. Support structures must be printed to join the local minimum to the structure below. Since this is enclosed and cannot be machined away, it will be left within the tank, which causes a small reduction in the available volume. Two of the sample tanks have pipes running along their edges to feed the sample valves, so the part orientation was chosen such that the tank without any piping will have the local minimum and its supporting structure. This prevents any single tank from having multiple reductions in volume, however small. Since the support material size and pattern will be dependent on the final printer selection, it is not modeled in the design. A cross section of the instrument tray in the build orientation is shown in Figure 4.15 with the local minimum highlighted. All other minima in the design are accessible from the outside to machine away supports.

4.5.6 Powder Removal

As discussed previously, all internal features must have openings for powder removal. Even if a DED system is used, unfused powder will still be present in the final part even if it is not completely filled, as in a PBF system. While the sample handling system does have several "built-in" openings, including the stagnation point intake, the valve seats, and the instrument inlet, these openings are all relatively small and are accessed through long channels. Powder removal through these holes would be challenging, and if even a small amount of powder was missed it could potentially contaminate the sample if ingested into the QITMS.

To facilitate powder removal from the tanks, six additional holes were added to the top of the instrument tray, two in each sample tank. The holes are located on opposite ends of each tank so that a cleaning solvent such as isopropyl alcohol can be flushed through the tank and reach a larger portion of the interior. The holes are roughly 5 mm in diameter, large enough to introduce an endoscope to visually examine the inside of the tank. Once the part is cleaned and inspected, the holes will need to be sealed. To facilitate this, they are set into studs that protrude from the surface of the instrument tray. This is highlighted in Figure 4.16.

The studs give the holes enough depth to be tapped for 1/4-20 UNC or metric M6. This allows the holes to function as sensor ports into the tanks, for example, to collect temperature and pressure data. Pressure sensors in the tanks would allow the valves to operate closed-loop, only staying open long enough to raise the tank pressure above some minimum value. There are currently no plans to instrument the tanks, in which case the holes would simply be plugged.

4.5.7 Machinability

The surface roughness and dimensional tolerance of metal AM parts are considerably worse than those produced by conventional machining. While in many cases this is acceptable,

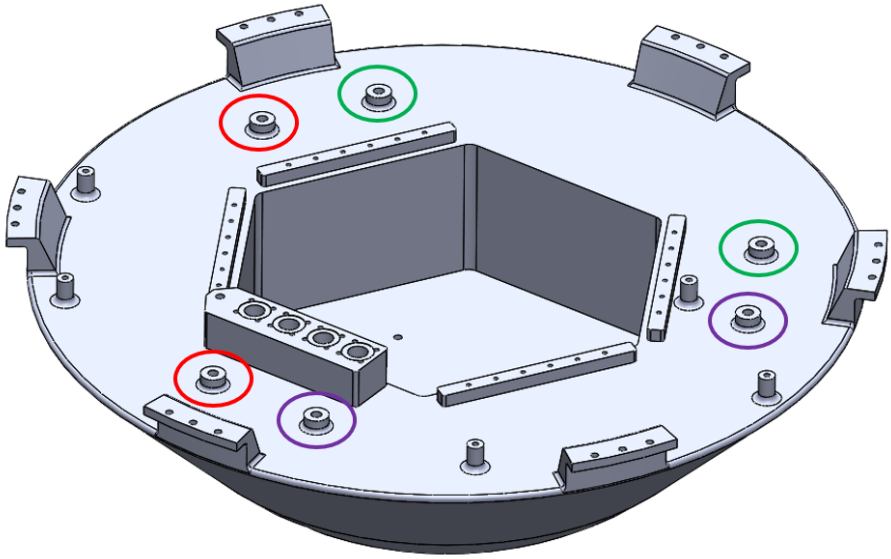

Figure 4.16: Instrument tray powder removal holes, set into studs to allow the holes to be tapped. Studs circled with the same color are set into the same tank. The five other studs visible on the top are not used for powder removal.

some features require post-print machining to achieve the required surface finish or tolerances, and care must be taken to ensure that these features will be accessible to machine tools. In the case of the Cupid's Arrow instrument tray, several such locations were identified. All of the valve interfaces must be machined to meet the tight tolerances specified by the valve manufacturer in order to ensure a leak-free seal against the copper gasket. Threaded holes must be drilled and tapped after printing, since the screw threads are too small to accurately print. Finally, any important mating surfaces must be machined to ensure proper flatness for mating.

Most of the post-print machined features are on the top of the instrument tray, shown in Figure 4.17. The red arrows indicate threaded holes that must be drilled and tapped after the print. Other than the powder removal holes, these are blind holes that will not be printed, and will be drilled and tapped to improve tolerances. The blue arrows indicate the valve locations. These require four tapped holes for the holding screws and two concentric recessed cylinders that must be machined flat to create a leak-free seal against the gasket. Finally, the green surfaces in the figure must be machined flat to provide a good mating

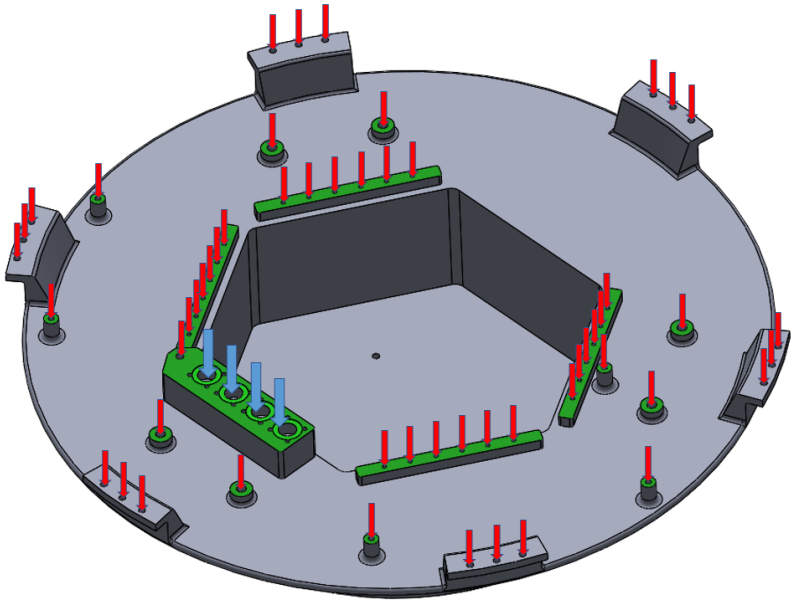

Figure 4.17: Top view of the instrument tray, showing machined surfaces. Red arrows show tapped hole locations, blue arrows show valve locations, and green surfaces show critical mating features that must be milled flat.

surface for other components. For aesthetic reasons, all of the exterior surfaces will have some form of post-processing, either milling or simple polishing, but the indicated surfaces also have tight dimensional requirements.

These milled surfaces not only need to be smooth to avoid wearing away the surface of attached parts, but they must be milled to consistent heights. The four raised brackets that attach to the battery lid must be the same height, or else the battery lid will be tilted. The maximum expected deviation in the "raw" part due to warping and printing tolerances is 0.6 mm, so these features will be printed 1 mm taller than required to ensure that they are higher than required in the raw part and can be milled down to the correct height.

There are fewer features on the bottom of the instrument tray that require machining. All six of the mating brackets must be milled on the bottom where they will attach to the outer structure, shown in green in Figure 4.18. The entire outer surface, which must align with the heatshield, will be turned on a lathe to the correct profile, this surface is shown in orange. Finally, the three intake valve are indicated with blue arrows, each one requires the

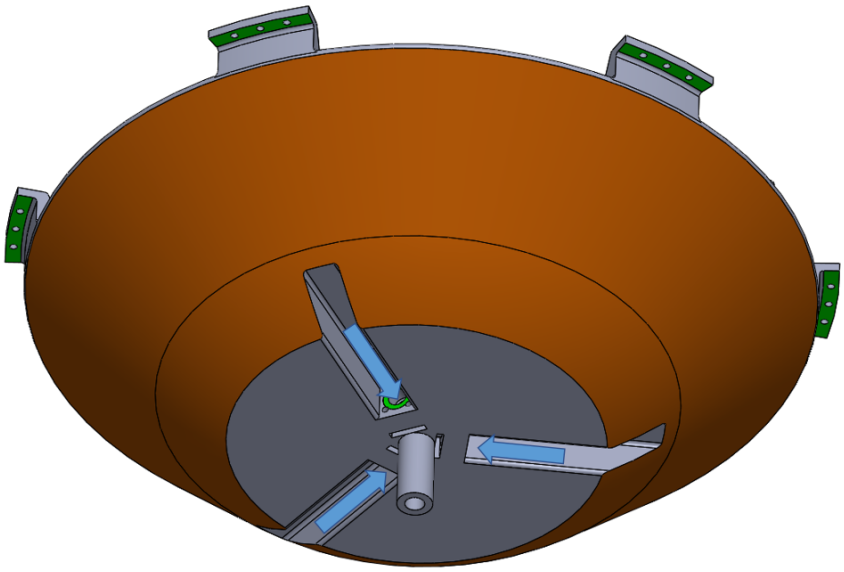

Figure 4.18: Bottom view of the instrument tray, showing machined surfaces in green and orange, and valve access channels in blue.

same post-processing as the tank valves. Channels were designed into the bottom of the instrument tray to allow access for this machining.

4.6 Outer Structure

The outer structure is the larger of the two printed structural pieces. It provides a bonding surface for the heatshield, holds the Lightband separation ring, and incorporates the ACS propulsion system. The outer structure will be printed from Ti-6Al-4V, a titanium alloy, and has a mass of 12.90 kg. Titanium was chosen for its superior strength to weight ratio compared to aluminum. The outer structure experiences higher loads than the instrument tray, since all of the launch loads will be transmitted through the outer structure via the Lightband. In addition, the cold gas propellant is stored under high pressure, causing high stress in the tank walls. The combination of tank internal pressure and structural loads meant that many of the features of the outer structure were limited by structural strength, not minimum printing feature size, so a high strength-to-weight ratio material was chosen to reduce structural mass.

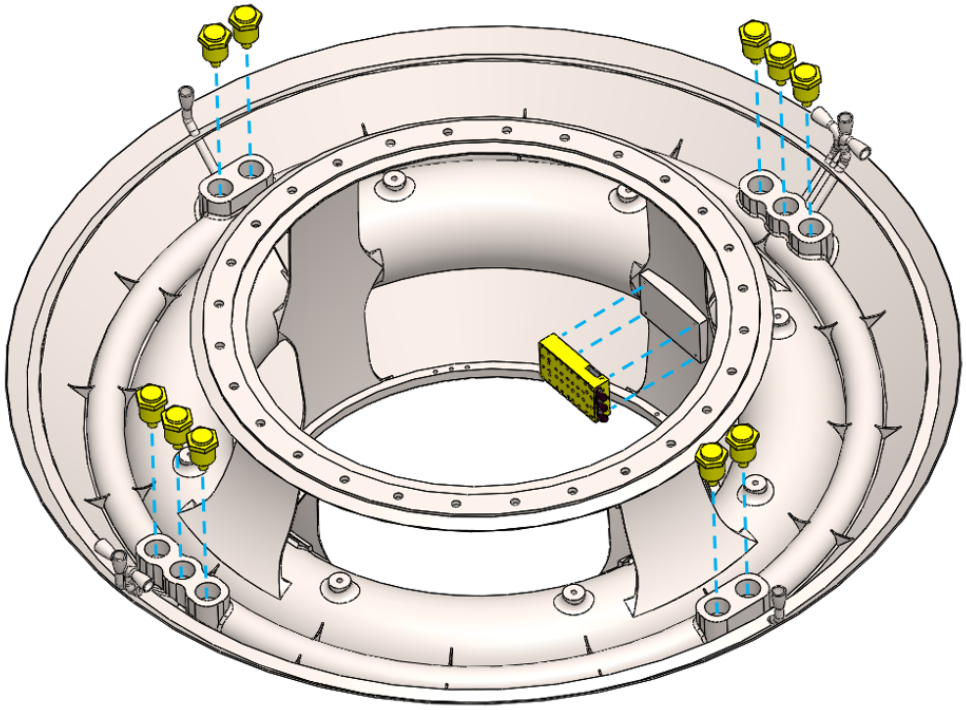

Figure 4.19: Exploded view of the outer structure, showing the ten ACS propellant valves and the Iris high power amplifier.

Like the instrument tray, the outer structure is designed to be tested alone before being integrated with the instrument tray. There are fewer components attached directly to the outer structure, which reduces the number of interfaces that must be created between the instrument tray and the structure. The ACS thrusters are the most complex system on the outer structure and will likely require the most testing time. The thrusters can be completely tested with the outer structure alone, so the system can be tested for leaks and performance in parallel with avionics testing on the instrument tray.

An exploded view of the outer structure and its attached components is shown in Figure 4.19.

4.6.1 Cold Gas Thrusters

The cold gas thrusters are the second fluid handling system incorporated into the Cupid's Arrow structure, and draw heavily on heritage from the BioSentinel thruster project. The

thrusters will be used for attitude control, trajectory correction, flythrough targeting, and the periapsis raise/lower maneuvers. Incorporating the propulsion system into the outer structure allows the propellant tanks and pipes to be blended into the support structure for the Lightband antenna. The hollow space inside the supporting truss is used for propellant storage, allowing the storage to be more compact than a modular system would allow.

The system uses ammonia, which has a high specific impulse of 101 seconds and a relatively high liquid density of 0.554 kg/L at 55°C [43]. This gives the propellant a volumetric impulse of 549 N-s/L, which is superior to the other cold gas propellants considered, and allows the propellant tanks to be relatively small. Note that the density given here is different than the one in Table 2.2, the densities in the table are given at 50°C, and Cupid's Arrow must operate up to 55°C. While a monopropellant or bipropellant system would have higher volumetric and specific impulse, this cold gas system was chosen for its simplicity, higher TRL, and lower risk to the primary payload.

The system has eight nozzles placed around the outer edge of the structure in four locations, with two blocks of three nozzles and two individual nozzles. This arrangement allows for spin/despin, precession of the spin axis, and limited ΔV. In addition to attitude control, the cold gas thrusters will be used for trajectory correction maneuvers, flythrough altitude targeting, and periapsis raise/lower maneuvers. The nozzle arrangement is shown in Figure 4.20. Note that all eight nozzles are located on the backshell to protect them during the atmospheric flythrough. Because of this, the precession and ΔV nozzles are uncoupled, so precession control will result in a small amount of unwanted ΔV capable, and trajectory correction maneuvers must take this into account.

Each nozzle has an expected thrust of 122 mN. Operating a coupled pair of spin nozzles on a 50% duty cycle to allow the plenum to periodically refill, the probe will require approximately 66 seconds to reach its nominal 5 rpm spin rate.

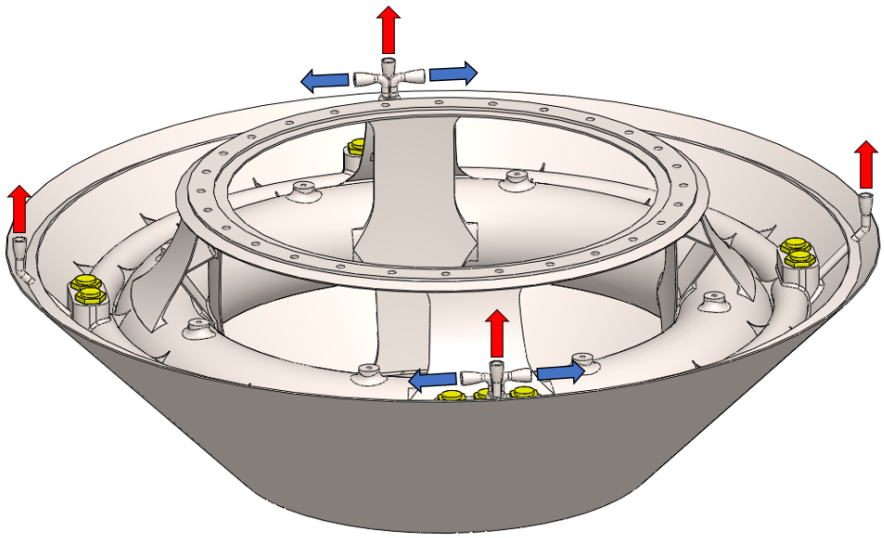

Figure 4.20: Cold gas thruster nozzle arrangement, showing exhaust directions for spin/despin (blue) and ΔV/precession (red) nozzles.

4.6.2 Propellant Tanks

As described previously, storing the propellant as a saturated liquid/vapor mixture allows a high storage density but requires two tanks: a main tank with a liquid/vapor mixture and a plenum with vapor alone. Both tanks must be able to withstand the saturation pressure of ammonia at the maximum internal operating temperature of 55°C: 2.311 MPa. While there are not yet formal guidelines for interplanetary secondary payloads, NASA requires pressure vessel safety factors of 2.5X on all secondary payloads for SLS or the ISS, so a 2.5X safety factor was chosen for tank sizing. In order to minimize tank wall thickness (and structure mass), both tanks were designed as toroids, which are inherently strong shapes that also leave the center of the probe available for the instrument tray. The main tank has a usable volume of 10.71 Liters and can store 5.93 kg of propellant, and the plenum has a volume of 1.48 L. Figure 4.21 shows a cutaway of the two tanks, along with a block of three nozzles and their corresponding valves.

Toroidal propellant tanks were chosen due to the inherent strength of the torus against internal pressure. While more geometrically complex shapes such as those seen in the

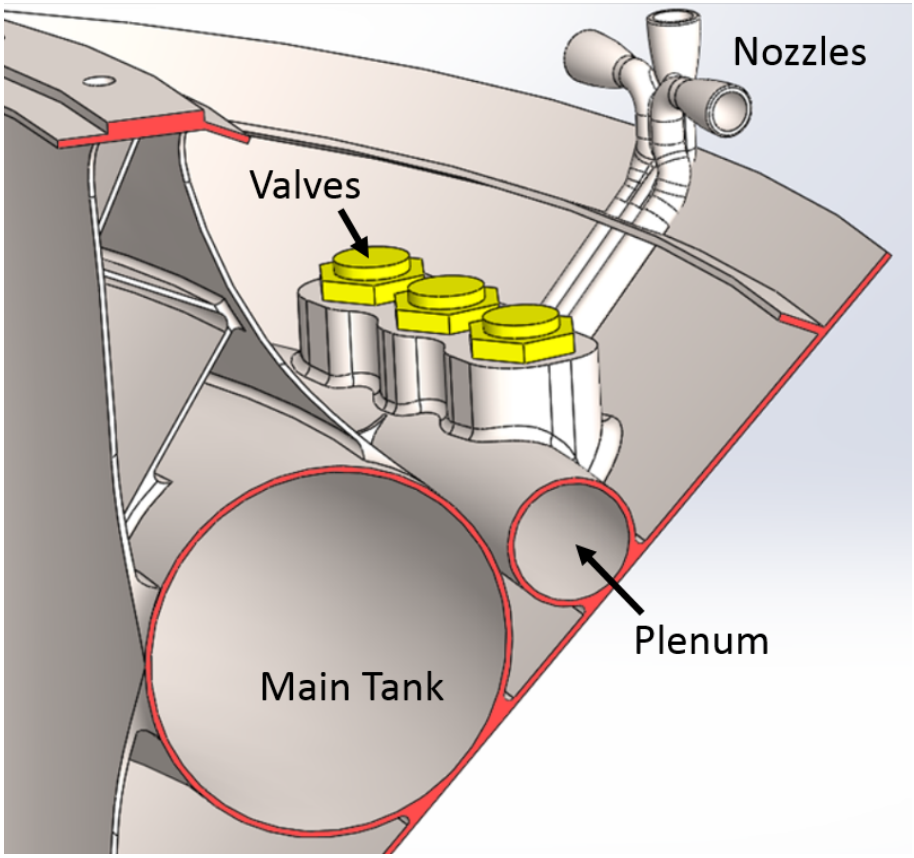

Figure 4.21: Cutaway of the outer structure, showing main tank, plenum, three-nozzle block, and nozzle valves. Red indicates faces on the section plane.

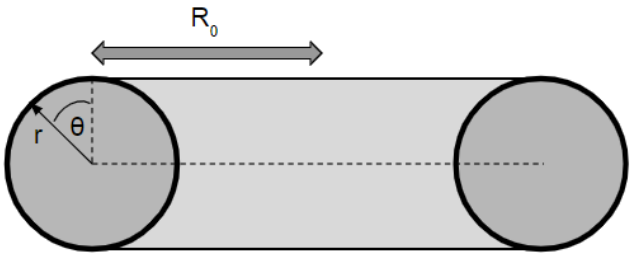

Figure 4.22: Torus geometric notation.

instrument tray would be possible with 3D printing, the additional wall thickness required to withstand the internal pressure was not desirable. The stresses in a thin walled torus experiencing uniform internal pressure are [73]:

$$\sigma_1 = \frac{Pr}{2h} \tag{4.1}$$

$$\sigma_2 = \frac{Pr}{2h}\frac{2R_0 + rsin\theta}{R_0 + rsin\theta} \tag{4.2}$$

where σ_1 is longitudinal stress, σ_2 is the hoop stress, P is the internal pressure, r is the minor radius, h is the wall thickness, R_0 is the major radius, and θ is the angle of the point where stress is being computed from the axis of the torus. Note that the longitudinal stress is the same as the longitudinal stress of a thin-walled cylinder. This geometry is illustrated in Figure 4.22.

The torus hoop stress is at its maximum when $\theta = 3\pi/2$, the inside ring of the torus where the radius of curvature is smallest. At that point, Eq 4.2 becomes:

$$\sigma_2 = \frac{Pr}{2h}\frac{2R_0 - r}{R_0 - r} \tag{4.3}$$

The tank must be designed to survive 2.5 times maximum expected operating pressure: 5.778 MPa. The major radius was chosen to be 270 mm, and the tank inner diameter was chosen to be 92 mm, giving a minimum wall thickness of 0.7 mm of Ti6Al4V, or 2.5

mm AlSi10Mg. The surfaces of printed parts are not fully dense, so a thickness factor must be applied. Rawal et al recommend a factor of 0.83[24], leading to a minimum wall thickness of 0.85 mm in Ti and 3.0 mm in Al. The wall was thickened to 1.5 mm in Ti to ensure all points would meet the minimum feature requirement. This also meets the "thin walled" approximation made in Eq 4.2, which generally requires $r/h > 10$, in this case the thickness ratio is 30.7. An aluminum torus of sufficient thickness would have a mass of 5.52 kg, compared to a titanium torus of 3.31 kg. The plenum wall thickness requirement was substantially less than the main tank, due to its smaller radius.

Initial sizing was done with the torus stress equations and finite element analysis was performed on the final model to validate this approximation. Maximum stress was found in the regions around the powder removal holes, since the addition of holes reduces the shape strength of the torus. The maximum stress near these points was 280 MPa, well below the expected yield strength of titanium of 820 MPa. The stress on the interior ring of the tank was 184 MPa, only slightly below the prediction from Eq 4.2 of 195 MPa. These results do not take into account the surface properties of the materials or imperfections in the manufacturing process, however, so actual stresses are expected to be somewhat larger.

4.6.3 Valves

The valves used in this system are larger than the ones used in BioSentinel and SPUD, to allow a higher mass flow rate and thus produce higher thrust. The valves are installed into printed manifolds that are built into the propellant tanks to reduce the length of piping the propellant must flow through. The valves are located around the perimeter of the outer structure, each one located close to its corresponding nozzle block to further reduce piping length. The effort to reduce pipe length is motivated by the anticipated pressure losses caused by the roughness of the interior of the pipes. Since the interior surfaces of the pipes cannot be machined, it will have the characteristic roughness of "raw" printed parts.

There are ten valves grouped into four manifolds, similar to the arrangement of the

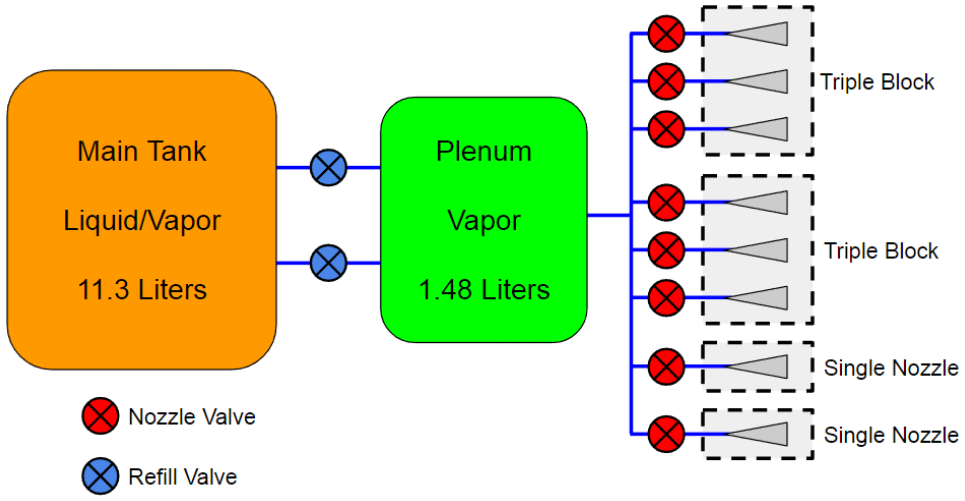

Figure 4.23: Schematic diagram of Cupid's Arrow ACS thrusters, showing main tank, plenum, valves, and nozzles.

nozzles. Two of the manifolds are located near the three-nozzle blocks and contain the three valves to control those nozzles. The other two manifolds are located near the single nozzles and contain two valves, one to drive the nearby nozzle and one to refill the plenum from the main tank. The use of two refilling valves increases the maximum duty cycle of the thrusters by allowing the plenum to be repressurized more quickly. A schematic of the thruster propellant tanks, valves, and nozzles is shown in Figure 4.23. The same components are highlighted in a top down CAD view of the outer structure in Figure 4.24.

4.6.4 Lightband Attachment

The 18.25" Lightband separation ring is attached to the top of the outer structure with 28 1/4-20 UNC fasteners held in place from below by locknuts. The Lightband was chosen because of its extensive heritage in small satellite deployments as well as the low overall mass of the system. After separation, the Lightband upper ring will remain with the probe, an additional mass of 1.83 kg. Since this upper ring is the aft-most component of the probe, minimizing its mass was crucial for stability.

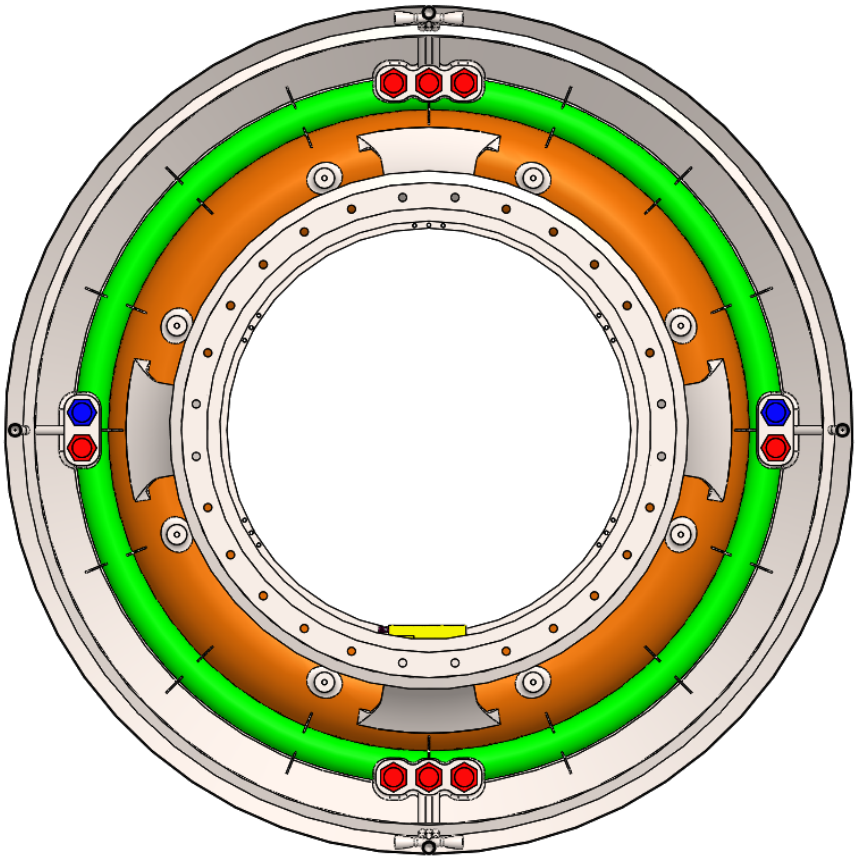

Figure 4.24: Top view of outer structure, showing the tanks and valves, coloration is the same as in Figure 4.23.

4.6.5 Iris Amplifier Attachment

The Iris radio power amplifier consumes an estimated 35 Watts when transmitting at 4 Watts RF, with a heat dissipation of 31 Watts. The majority of that heat dissipation (20 Watts) occurs in the high power amplifier (HPA). The HPA is not a large component, at 76 x 43 x 17 mm, and overheating of the HPA is an issue, especially when the probe is in Venus orbit with a relatively high solar thermal load. To mitigate this, the HPA was moved from the instrument tray to the outer structure, and was attached directly to the ACS main tank. This moves the HPA away from other heat dissipating electronics and allows it to more directly use the high thermal capacity of the propellant as a heat sink. Even if the propellant were completely isolated and unable to radiate heat, a 20 Watt input for 8 hours (the maximum duration of a DSN pass) would only be sufficient to heat the 6.26 kg of propellant from 20°C to 39°C [43]. In contrast, the 12.9 kg titanium structure alone would be raised to 126°C under the same conditions [74]. As propellant is consumed, the heat sinking ability of the main tank will decrease, so communications passes near the end of the missions could be cut short to prevent overheating.

The Iris attachment point is shown in Figure 4.25. The mount was designed to maximize surface area contact between the HPA and the structure. A thermally conductive epoxy will be applied to the bottom of the HPA immediately before the fasteners are installed to further improve the thermal path.

4.6.6 Inspectibility

Like the instrument tray, the outer structure was designed to be inspectible after printing. Both tanks have openings large enough to introduce endoscopes for visual inspection of the interior; the plenum has the ten valve openings, and the main tank has the eight powder removal holes. After endoscope inspection, the outer structure will be subject to CT scans to locate any voids.

NASA safety standards for pressure vessels require a 2.5X factor of safety in design

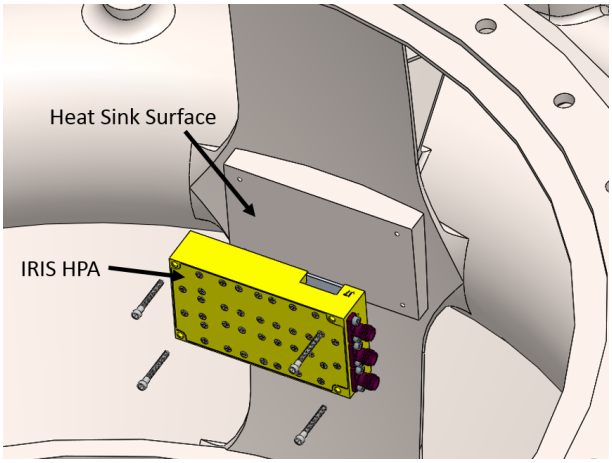

Figure 4.25: Exploded view of Iris High Power Amplifier attachment location.

above maximum expected operating pressure (MEOP) [30]. In this case, MEOP is the saturation pressure of ammonia at 55°C: 2.311 MPa [43], so the tank is designed to withstand 5.778 MPa. In addition, after CT scanning verifies that the tank walls are free of voids, the flight unit will undergo a proof pressure test at 1.5X MEOP (3.437 MPa) to demonstrate structural integrity. Finally, a spare structure, identical to the flight unit, will be destructively tested after CT scanning. While this test is not required by secondary payload rules, a burst test will increase confidence in the printed structure and will be used to validate the finite element analysis used in the design of the tank.

4.6.7 Print Orientation

Since the two propellant tanks are toroidal, there are no orientations that can avoid shallow printing angles of internal features. Non-toroidal shapes were investigated, such as rhombus cross-sections, but the inherent strength of the toroid allowed the walls to be substantially thinner and ultimately saved more mass than the estimated extra mass of the support material. The supports will also contribute to the tank's structural integrity, but the structural load model was made conservatively assuming that they do not contribute, since their exact geometry is unknown and cannot be relied upon. The support material will also act as baffling for the liquid propellant, reducing liquid slosh. This will be particularly

important during spin-up/spin-down maneuvers, since without baffling the propellant will continue to spin within the toroidal main tank around the probe's axis until slowed (or accelerated) by viscous forces. This will increase the amount of time required to spin and despin, and could result in unusual precession torques if the spacecraft attempts to rotate while the propellant is still spinning. Baffles will enhance the effect of the viscous forces by increasing the surface area contacting the propellant, and reduce the time required to change the spin rate. Based on previous printed systems, the structural elements inside the tank will occupy no more than 5% of the tank volume. Without supports, the torus has an internal volume of 11.27 L, giving it a usable volume of 10.71 L. Because the propellant is stored as a saturated liquid-vapor mixture, there is no concern about liquid adhering to the high internal surface area, since it will evaporate as the pressure is lowered.

Since the top of the structure will be more accessible to milling and turning tools, the part will be printed upside down, ensuring that the majority of the support material can be machined away. This orientation allows the Lightband support ring to be supported only from below (aft side), the side that will already be machined flat, rather than the nose end, which would be difficult to access. The propellant tanks will both require support material to connect them to the build plate, but since these supports will connect them directly with the base they can be removed by a vertical mill. The outer surface of the structure will be inclined at a 45° angle, allowing it to be self-supporting. The instrument tray support ring will most likely require some form of support material, but since the ring is already designed to be accessed from below by lathe tools, those supports can be removed. The most difficult features to post-process will be the nozzles. The four horizontal nozzles will most likely require some form of support to avoid deformation, and will require finishing to remove the roughness on the interior. This will require delicate milling, and any damage to the nozzle will require the structure to be reprinted. A cross section of the structure is shown in Figure 4.26, with the build direction marked.

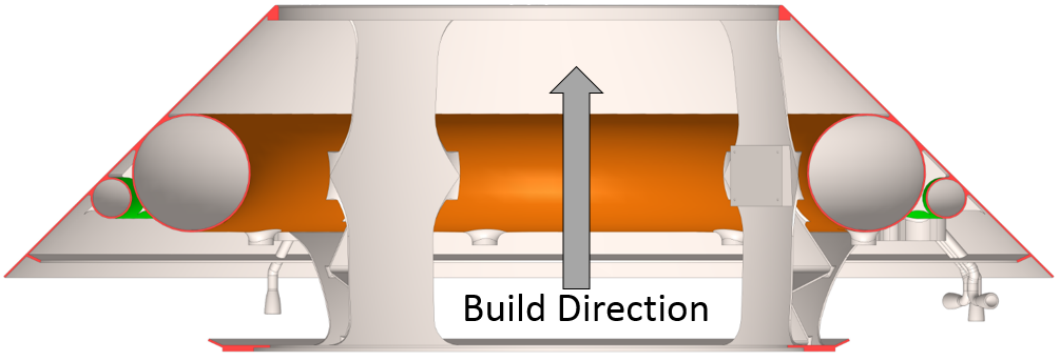

Figure 4.26: Cross section view showing the outer structure's build direction, red highlighted areas show where the section view intersects the part.

4.6.8 Powder Removal

As with the instrument tray sample tanks, holes were required to remove unmelted powder from the propellant tanks. The solenoid valves connect directly to the plenum, so those holes can be used to remove powder from the plenum. Eight holes are designed into the top of the main tank, printed into raised studs, allowing them to be tapped for a 1/4-20 UNC or metric M6, similar to the instrument tray. After the powder is removed, the holes will be tapped and sensors installed to allow the propellant state to be monitored. Four pressure sensors and four thermisters are currently planned for redundancy. If the additional sensors are not necessary, the unused holes can simply be plugged. These eight studs are shown in Figure 4.27, also highlighting the locations of the plenum and main tank.

4.6.9 Machining

Like the instrument tray, the outer structure has a large number of features that require post-printing machining, although for aesthetic reasons all exposed surfaces will have some form of finishing. These features are shown in Figure 4.28.

The ten ACS thruster valves (indicated with blue arrows in the figure) have threads that must be tapped, as well as precise geometric requirements for their manifolds, with a ±13μm diameter tolerance on the sealing hole. This is unachievable with any existing

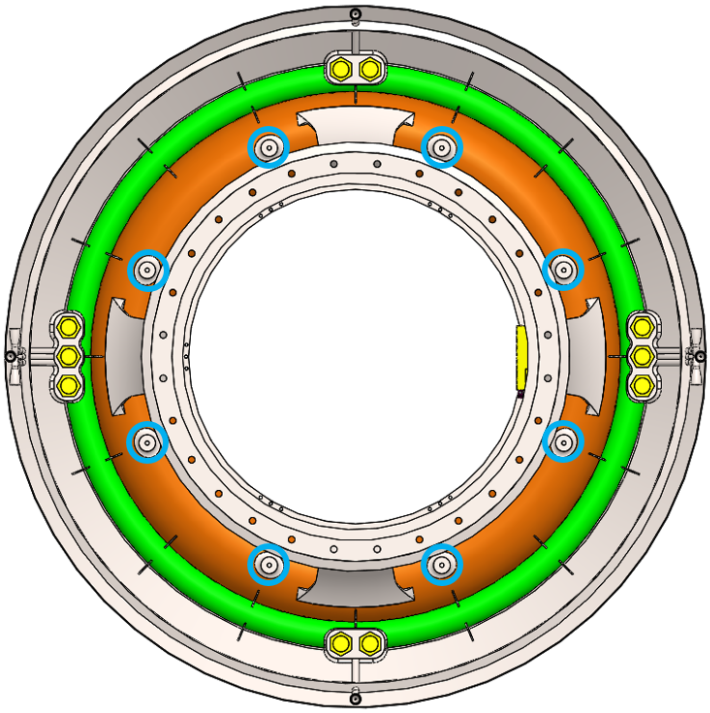

Figure 4.27: Top view of the outer structure, showing the main tank (orange), plenum (green), and main tank powder removal holes (circled blue).

additive manufacturing technology, so the holes are designed undersized, to be drilled and reamed to the correct final diameter. The undersized holes are still large enough to serve their dual purpose of powder removal and endoscope inspection. The eight main tank powder removal holes must be drilled and tapped to accept sensors, these are indicated with red arrows, although some are obscured by the Lightband ring.

The Lightband ring must be machined flat (shown in green) to provide a good mating surface for the separation ring, and the 24 bolt holes will be printed undersized and drilled to their final 8 mm diameter. These are not tapped holes, since the bolts will be secured by locknuts. The backshell attaches to the outer structure along two flanges, both highlighted in orange. Both will be turned on a lathe to achieve the required angle and surface finish for backshell attachment. These features are all accessible from the top of the outer structure, and all drill/tap/ream operations were designed to be aligned with the z axis of the probe to simplify the post-processing.

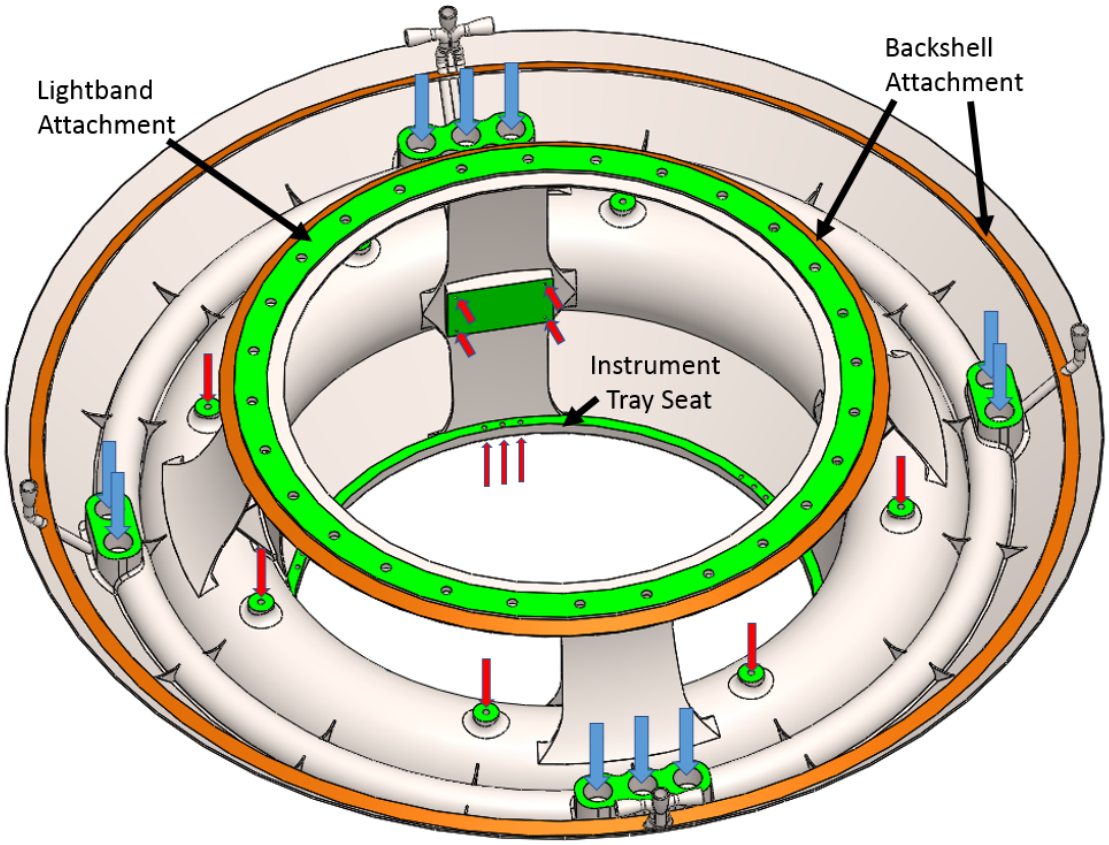

Figure 4.28: Cupid's Arrow outer structure with post-print machining locations highlighted. Blue arrows indicate ACS valves, red arrows indicate drill and tap locations (some are obscured). Orange and green surfaces must be machined flat.

The Iris power amplifier attachment point also requires post-print machining, and will be more difficult to access. A large end mill will be sufficient to machine the mounting surface (green) flat, but a five axis drill will be necessary to drill and tap the attachment holes.

The seating ring for the instrument tray (shown in green in the figure) must also be machined to provide an even surface for the tray to attach, but it is too far inside the outer structure to be reasonably accessible. Instead it will be accessed from the bottom, with a right angle boring tool on a lathe. The 18 threaded holes for attaching the instrument tray will also be tapped from below to accept locking helical inserts. Finally, the entire outer surface of the structure will be turned on a lathe to provide a smooth surface for the heatshield.

4.7 Conclusion

The Cupid's Arrow mission concept utilizes miniaturized electronics and an additively manufactured structure to perform in situ measurements of the atmosphere of Venus with a small, low-cost mission. Like SPUD, the probe contains an integrated propulsion system to improve its volumetric efficiency and reduce structure part counts. However, Cupid's Arrow shows how multifunctional structures can also be applied to increase scientific returns of a planetary probe. The instrument tray was designed to augment the mass spectrometer by capturing additional atmospheric gas samples in otherwise unused volumes within the structure. The result is a smaller, more capable probe. The volume savings and increased science returns made possible by the multifunctional structure are especially important for small planetary probes, given the extremely limited interplanetary secondary payload opportunities.

CHAPTER 5
CONCLUSION

5.1 Future Work

The BioSentinel thruster project is complete, and the flight unit is at NASA Ames awaiting integration with the spacecraft. The 3U SPUD design is also complete, and is optimized for an inspector satellite demonstration mission. In the future, the optimization program will be used with the NASA Goddard "42" software to generate trajectories for a wider range of potential missions, including rendezvous and docking. The SPUD design will also be adapted to a 1U form factor to further reduce the cost of a potential demonstration mission.

5.2 Publications

The publications related to this work are listed below, separated by type.

5.2.1 Conference Publications

- M. Sorgenfrei, T. Stevenson, and G. Lightsey, "Considerations for Operation of a Deep Space Nanosatellite Propulsion System", in Proceedings of AAS Guidance, Navigation, and Control Conference, Breckenridge, Colorado, 2016.
- M. Sorgenfrei, T. Stevenson, and G. Lightsey, "Performance Characterization of a Cold Gas Propulsion System for a Deep Space CubeSat", in Proceedings of AAS Guidance, Navigation, and Control Conference, Breckenridge, Colorado, 2017, pp. 835–849.
- T. Stevenson and G. Lightsey, "Design and Characterization of a 3D-Printed Attitude Control Thruster for an Interplanetary 6U CubeSat", in 30th Annual AIAA/USU Conference on Small Satellites, Logan, UT, 2016.
- T. Stevenson and G. Lightsey, "Design and Operation of a Thrust Test Stand for University Small Satellite Thrusters", in AIAA SciTech Forum, Kissimmee, Florida, 2018.

- C. Sotin, N. Arora, G. Avice, J. Baker, M. Darrach, A. Freeman, G. Lightsey, S. Madzunkov, B. Marty, S. Peet, T. Stevenson, "Cupid's Arrow: a small satellite to measure noble gases in the atmosphere of Venus and Titan", in 12th Low-Cost Planetary Missions Conference, Pasadena, CA, 2017.

5.2.2 Peer-Reviewed Journal Publications

- T. K. Imken, T. H. Stevenson, and E. G. Lightsey, "Design and Testing of a Cold Gas Thruster for an Interplanetary CubeSat Mission", Journal of Small Satellites, vol. 4, no. 2, pp. 371–386, 2015.
- G. Lightsey, T. Stevenson, and M. Sorgenfrei, "Development and Testing of a 3D-Printed Cold Gas Thruster for an Interplanetary CubeSat", Proceedings of IEEE, vol. 106, no. 3, pp. 379–390, 2018.

5.2.3 Future Journal Publications

- T. Stevenson, G. Lightsey, J. Baker, C. Sotin, and T. Freeman, "Design of a Venus Atmospheric Probe Using Additive Manufacturing", Journal of Spacecraft and Rockets, planned submission Nov 2018.
- T. Stevenson, G. Lightsey, "Optimization of a 3D-Printed Structure for Inspector CubeSats", Acta Astronautica, planned submission end 2018.

5.3 Conclusions

The contributions outlined in this proposal represent an improvement to the state of the art for CubeSat structural design and propulsive attitude control. The first contribution to improving small satellite volume efficiency was the design of a compact, 3D printed ACS thruster for an interplanetary CubeSat. The use of 3D printing allowed the design to use the limited available volume more efficiently than a conventionally manufactured thruster. The propulsion system was tested extensively both at Glenn Research Center and at Georgia Tech on a custom, low-cost thrust test stand. A total of three thrusters were built and tested, and the flight unit has been delivered to NASA, where it is awaiting integration into the spacecraft. This project demonstrated how additive manufacturing can be used to produce small satellite components in volume-saving form factors that would be otherwise impossible to achieve.

This work was then extended to design a multifunctional CubeSat structure (SPUD) that not only provides structural support, but also functions as a propulsion system. The structure is designed to provide six independent degrees of freedom to the spacecraft to support missions with high maneuverability requirements, such as inspector satellites and docking missions. The thruster geometry can be easily adapted to tailor the propulsion system to a specific mission without altering the basic design. This was demonstrated with SPUD by tailoring the nozzle thrust directions to minimize average propellant consumption needed to follow a set of inspection trajectories. In addition to being adaptable to different trajectories, SPUD's integrated propulsion system is more volumetrically efficient than an equivalent structure with a modular thruster.

Finally, the multifunctional structure concept was extended to produce a design of an all-printed structure for a Venus atmospheric probe, the result of a concept study with the Jet Propulsion Laboratory called Cupid's Arrow. This design incorporates a propulsion system based on the design developed for SPUD, and also augments its scientific instrument, a mass spectrometer, by storing atmospheric samples in otherwise unused volume. The application of multifunctional structures to interplanetary probes has a particularly large impact, due to their even more restrictive volume and mass constraints. This design produced a probe that is more attractive as a secondary payload than it would have otherwise been, with a more compact structure and increased science return.

This work represents a potential improvement in small satellite design by demonstrating how recent improvements in additive manufacturing can be applied to produce multifunctional structures that are more compact than the sum of their systems. The system designs presented here serve as both case studies of the possible applications of multifunctional structures and as potential low-cost demonstration missions.

APPENDIX A

ACRONYMS AND ABBREVIATIONS

ADCS	Attitude Determination and Control System
AM	Additive Manufacturing
AU	Astronomical Unit
CAD	Computer Aided Design
CCSDS	Consultative Committee for Space Data Systems
CDH	Command and Data Handling
CFD	Computational Fluid Dynamics
CM	Center of Mass
COTS	Commercial Off The Shelf
CT	Computed Tomography
DED	Directed Energy Deposition
DSN	Deep Space Network
EDU	Engineering Development Unit
EM-1	Exploration Mission 1
EPS	Electrical Power System
FEA	Finite Element Analysis
GPIO	General Purpose Input/Output
HPA	High Power Amplifier
ISP	Specific Impulse
LVDT	Linear Variable Differential Transformer
MEOP	Maximum Expected Operating Pressure
MOI	Moment of Inertia

PBF	Powder Bed Fusion
PCB	Printed Circuit Board
PICA	Phenolic-Impregnated Carbon Ablator
QITMS	Quadrupole Ion Trap Mass Spectrometer
SLA	Stereolithography
SLS	Space Launch System, or Selective Laser Sintering
SPUD	Structural Propulsion Unit Demonstrator
SSDL	Space Systems Design Lab
VOI	Venus Orbit Insertion

APPENDIX B

BIOSENTINEL THRUSTER REQUIREMENTS

B.1 Physical Requirements

Req ID	Title	Description	Verification
Prop-1	Reference Frame	The Freeflyer propulsion system shall perform all requirements and analyses referenced to the spacecraft body frame.	Inspection
Prop-2	Subsystem Mass	The Freeflyer propulsion system shall not exceed a total mass of 1.4 kg.	Testing
Prop-3	Subsystem Volume	The Freeflyer propulsion system shall not exceed a total volume envelope of 235 mm x 110 mm x 40.25 mm. The main body of the Freeflyer propulsion system shall have a maximum z-axis dimension of 210 mm.	Inspection
Prop-4	Diagnostic Port	The Freeflyer propulsion system volume shall accommodate a cut-out as described in the Propulsion System ICD (A9SP-1404- XR018) for a data/power diagnostic port.	Inspection
Prop-5	Propellant Capacity	The Freeflyer propulsion system shall be capable of storing 200 g of propellant in the main tank.	Testing

B.2 SMA Requirements

Req ID	Title	Description	Verification
Prop-6	Operating Life	The Freeflyer propulsion system shall be designed for 12 months of nominal operations, with an 18 month stretch operating goal.	Analysis
Prop-7	Operating Pressure	The Freeflyer propulsion system maximum operating pressure shall be less than 100 PSI.	Testing
Prop-8	Pressure Safety Factor	The Freeflyer propulsion system maximum operating pressure shall carry a safety factor of 2.5x.	Analysis
Prop-9	Fluid Compatibility	The 3D-printed portion of the Freeflyer propulsion system shall be compatible with ethanol and alcohol wipes.	Inspection
Prop-10	Main Tank Pressure Cycles	The Freeflyer propulsion system shall be capable of experiencing 5 pressurization/depressurization cycles of the main tank over its lifetime.	Testing
Prop-11	Plenum Pressure Cycles	The Freeflyer propulsion system shall be capable of experiencing 150 pressurization/depressurization cycles of the plenum over its lifetime.	Testing

B.3 Environmental Requirements

Req ID	Title	Description	Verification
Prop-12	EM Compatibility	The Freeflyer propulsion system shall function without degradation when operated in an electromagnetic environment induced by the Freeflyer.	Testing
Prop-13	Radiation Environment	The Freeflyer propulsion system shall be capable of tolerating a total ionizing dose of 10 kRad over the life of the mission.	Analysis
Prop-14	Mechanical Environment	The Freeflyer propulsion system shall function nominally after exposure to the launch mechanical environment.	Testing
Prop-15	Maximum Temperature	The Freeflyer propulsion system shall be capable of operating at a maximum ambient external temperature of 50°C.	Testing
Prop-16	Minimum Operating Temperature	The Freeflyer propulsion system shall be capable of operating at a minimum ambient external temperature of 0°C.	Testing
Prop-17	Minimum Survival Temperature	The Freeflyer propulsion system shall be capable of surviving a minimum ambient external temperature of -15°C.	Testing
Prop-18	Storage Life	The Freeflyer propulsion system shall be designed for 8 months of storage in the loaded and pressurized configuration without greater than 10% loss of propellant mass.	Testing

B.4 Functional/Mission Requirements

Req ID	Title	Description	Verification
Prop-19	Thrust Directions	The Freeflyer propulsion system shall be capable of producing thrust in all three body-fixed axis directions, as documented in the Propulsion System ICD (A9SP-1404- XR018).	Testing
Prop-20	Thrust Direction Accuracy	The Freeflyer propulsion system shall generate thrust in the body-fixed axis directions to an accuracy of ±10 ° with respect to each body-fixed axis.	Inspection
Prop-21	Nominal Thrust	The Freeflyer propulsion system shall be capable of generating a nominal thrust of 40 mN ± 5 mN from each nozzle at the nominal spacecraft operating temperature.	Testing
Prop-22	Total Impulse	The Freeflyer propulsion system shall provide a total impulse over the life of the mission of at least 36 N-sec.	Testing
Prop-23	Minimum Impulse Bit	The Freeflyer propulsion system shall be capable of generating a minimum impulse bit of 120 microN-sec from all thrusters.	Testing

B.5 Electrical/Power/Comm Requirements

Req ID	Title	Description	Verification
Prop-24	Regulated Power	The Freeflyer propulsion system shall operate on regulated 5 ± 0.25 V while drawing no more than 1 A.	Testing
Prop-25	Unregulated Power	The Freeflyer propulsion system shall operate on unregulated 8-18.5 V while drawing an average of 1 A, not to exceed 2 A.	Testing
Prop-26	Serial Communication	The Freeflyer propulsion system shall communicate with the C&DH processor using RS-422 protocol at 5 Hz.	Testing
Prop-27	Propulsion Telemetry	The Freeflyer propulsion system shall be capable of generating telemetry as specified in the Propulsion System ICD (A9SP-1404- XR018).	Testing
Prop-28	Telemetry Format	The Freeflyer propulsion system shall use the CCSDS Space Packet format when sending telemetry to the C&DH processor.	Testing
Prop-29	Power Cycling	The Freeflyer propulsion system shall functional nominally after being powered off.	Testing

APPENDIX C

SPUD MASS BUDGET

The contigencies in the mass budget below use the following convention:

- Components obtained and weighed: 3%
- Datasheet mass or structure CAD mass: 5%
- Fasteners and custom PCBs: 10%
- Wires and cables: 30%

	Component			Subsystem
	CBE (g)	Contingency	Allocated (g)	Allocated (g)
Payload				521.8
Camera	469.3	5%	492.7	
Fasteners	2.8	10%	3.1	
Cables	20	30%	26.0	
Navigation				136.7
D60 Sun Sensor (4)	24.8	5%	26.0	
Ancom GPS Antenna	62	3%	63.9	
Novatel GPS Receiver	21.5	5%	22.6	
Fasteners	7.8	10%	8.6	
Cables	12.0	30%	15.6	
CDH				78.8
Nanodock	51.0	5%	53.6	
Nanomind A3200	24.0	5%	25.2	
EPS				883.3
BP4 Battery Pack	262.0	3%	269.9	
P31us Power Board	98.5	3%	101.5	
Solar Panels (4)	340.0	5%	357.0	
Solar Cells (21)	84.0	5%	88.2	
Separation Switches (4)	8.0	3%	8.2	
Cables	45.0	30%	58.5	

	Component			Subsystem
	CBE (g)	Contingency	Allocated (g)	Allocated (g)
Propulsion				400.0
Valve Manifolds (4)	166.7	3%	171.7	
Manifold Backplates (4)	16.4	3%	16.9	
Lee IEP Valves (10)	48.0	3%	49.4	
Compression Fittings (20)	81.6	3%	84.0	
Filters (10)	25.0	3%	25.8	
Fill Valves (2)	7.6	3%	7.8	
Pressure Sensors (2)	4.0	3%	4.1	
Thermister Probes (2)	4.4	3%	4.5	
Manifold Fasteners	6.5	10%	7.2	
Control Boards	26.0	10%	28.6	
COM				136.6
AX100 Radio	24.5	3%	25.2	
UHF Dipole Antenna	86.5	3%	89.1	
Cables	15.0	30%	19.5	
Fasteners	2.5	10%	2.8	
Structure				1107.8
Printed Structure	860.5	5%	903.5	
Avionics Upper Bracket	51.3	5%	53.9	
Avionics Lower Bracket	51.3	5%	53.9	
Avionics Standoffs	74.6	10%	82.1	
Avionics Fasteners	13.2	10%	14.5	
			Allocated Total Mass	3264.9
			Mass Limit (PPOD)	4000.0
			Mass Margin	22.5%

APPENDIX D

SPUD POWER BUDGET

	CBE (W)	Duty Cycle	Contingency	Allocated (W)
Payload				
Camera	1.00	100%	10%	1.10
Navigation				
D60 Sun Sensor (4)	0.28	100%	5%	0.28
Antcom GPS Antenna	0.05	20%	3%	0.01
Novatel GPS Receiver	1.10	20%	3%	0.22
CDH				
Nanodock	0.08	100%	3%	0.08
Nanomind A3200	0.17	100%	5%	0.17
EPS				
BP4 Battery Pack	0.15	100%	3%	0.15
P31us Power Board	0.26	100%	3%	0.26
Propulsion				
Lee IEP Valves (10)	0.56	1%	3%	0.00
Pressure Sensors (2)	0.02	100%	3%	0.02
Thermister Probes (2)	0.005	100%	3%	0.01
Control Boards	0.06	100%	10%	0.06
COM				
AX100 Radio	2.60	5%	3%	0.13
			Total Allocated (W)	2.48

REFERENCES

[1] G. Bonin, N. Roth, S. Armitage, J. Newman, B. Risi, and R. E. Zee, "CanX-4 and CanX-5 Precision Formation Flight: Mission Accomplished!", in 29th Annual AIAA/USU Conference on Small Satellites, Logan, UT, 2015.

[2] A. Klesh and J. Krajewski, "MarCO : CubeSats to Mars in 2016", in 29th Annual AIAA/USU Conference on Small Satellites, Logan, UT, 2015.

[3] C. R. Boshuizen, J. Mason, P. Klupar, and S. Spanhake, "Results from the Planet Labs Flock Constellation", in 28th Annual AIAA/USU Conference on Small Satellites, Logan, UT, 2014.

[4] California Polytechnic State University, "Poly Picosatellite Orbital Deployer Mk . III Rev E User Guide", CalPoly, San Luis Obispo, CA, Tech. Rep., 2014.

[5] Innovative Solutions in Space, "ISIPOD CubeSat Deployer", Delft, The Netherlands, Tech. Rep., 2014, pp. 11–12.

[6] Planetary Systems Corp, "Payload Specifications for 3U, 6U, 12U AND 27U", Silver Spring, MD, Tech. Rep., 2016.

[7] E. Kulu, Nanosatellites by types, 2018.

[8] K. F. Robinson and G. Norris, "NASA Space Launch System : Deep-Space Delivery for Smallsats", in 31st Annual AIAA/USU Conference on Small Satellites, Logan, UT, 2017.

[9] B Burgett, J Long, P Whaley, A Raz, R Herrick, D Thorsen, and P Delamere, "Mini-MAGGIE: CubeSat MAGnetism and Gravity Investigation at Europa", in 47th Lunar and Planetary Science Conference, vol. 99775, 2016, pp. 2–3.

[10] NanoRacks, "NanoRacks CubeSat Deployer Interface Definition Document", Houston, TX, Tech. Rep., 2018.

[11] Space and Missile Systems Center, "Evolved Expendable Launch Vehicle Rideshare User Guide", El Segundo, CA, Tech. Rep., 2016.

[12] SpaceX, "Falcon 9 Launch Vehicle Payload User Guide Rev 2", Hawthorne, CA, Tech. Rep., 2015.

[13] A. Freeman, “Exploring our Solar System with Cubesats and Smallsats : a NASA / JPL Perspective”, in The 4S Symposium 2018, Sorrento, Italy, 2018.

[14] J. Mueller, J. Ziemer, and R. Hofer, “A survey of micro-thrust propulsion options for microspacecraft and formation flying missions”, in 5th Annual CubeSat . . . , 2008, pp. 1–19.

[15] S.-J. Chung, S. Bandyopadhyay, R. Foust, and G. Subramanian, “Review of Formation Flying and Constellation Missions Using Nanosatellites”, Journal of Spacecraft and Rockets, vol. 53, no. 3, 2016.

[16] C. D. Norton, S. Pellegrino, and M. Johnson, “Findings of the KECK Institute for Space Studies Program on Small Satellites : A Revolution in Space Science”, in 27th Annual AIAA/USU Conference on Small Satellites, Logan, UT, 2013.

[17] F. P. W. Melchels, J. Feijen, and D. W. Grijpma, “Biomaterials A review on stereolithography and its applications in biomedical engineering”, Biomaterials, vol. 31, no. 24, pp. 6121–6130, 2010.

[18] B. Asberg, G. Blanco, P. Bose, J. Garcia-Lopez, M. Overmars, G. Toussaint, G. Wilfong, and B. Zhu, “Feasibility of Design in Stereolithography”, Algorithmica, pp. 61–83, 1997.

[19] W King, A Anderson, R Ferencz, N Hodge, C Kamath, S Khairallah, and A Rubenchik, “Laser powder bed fusion additive manufacturing of metals; physics, computational, and materials challenges”, Applied Physics Review, 2015.

[20] Metal Solutions, “EOS M 290”, Tech. Rep., 2018.

[21] Loughborough University, Directed Energy Deposition, 2018.

[22] B. E. Carroll, R. A. Otis, J. Paul, J.-o. Suh, R. P. Dillon, A. A. Shapiro, D. C. Hofmann, Z.-k. Liu, and A. M. Beese, “Functionally graded material of 304L stainless steel and inconel 625 fabricated by directed energy deposition : Characterization and thermodynamic modeling”, Acta Materialia, vol. 108, pp. 46–54, 2016.

[23] E. Zapata, “The State of Play US Space Systems Competitiveness”, in Future In-Space Operations Seminar, 2017.

[24] S. Rawal, J. Brantley, and N. Karabudak, “Additive Manufacturing of Ti-6Al-4V Alloy Components for Spacecraft Applications”, in 6th International Conference on Recent Advances in Space Technologies, Istanbul, Turkey, 2013.

[25] M. E. Orme, M. Gschweitl, M. Ferrari, R. Vernon, I. Madera, R. Yancey, and F. Mouriaux, "Additive Manufacturing of Lightweight , Optimized , Metallic Components Suitable for Space Flight", Journal of Spacecraft and Rockets, vol. 54, no. 5, pp. 1050–1059, 2017.

[26] Aerojet, Additive Manufacturing, 2018.

[27] SpaceX, SpaceX Launches 3D Printed Part to Space, Creates Printed Engine Chamber, 2014.

[28] G. Lightsey, T. Stevenson, and M. Sorgenfrei, "Development and Testing of a 3D-Printed Cold Gas Thruster for an Interplanetary CubeSat", Proceedings of IEEE, vol. 106, no. 3, pp. 379–390, 2018.

[29] J. R. Wertz and W. J. Larson, Space Mission Analysis and Design, 3rd. Springer Netherlands, 1999.

[30] NASA, "NASA-STD-5019A Change 1", Tech. Rep., 2016.

[31] D. Hinkley, "SSC08-VII-7 A Novel Cold Gas Propulsion System for Nanosatellites and Picosatellites", 2003.

[32] G. Manzoni and Y. L. Brama, "SSC15-IV-5 Cubesat Micropropulsion Characterization in Low Earth Orbit", in 29th Annual AIAA/USU Conference on Small Satellites, Logan, UT, 2015.

[33] N. G. Orr, J. K. Eyer, B. P. Larouche, and R. E. Zee, "Precision Formation Flight: The CanX-4 and CanX-5 Duel Nanosatellite Mission", in 21st Annual AIAA/USU Conference on Small Satellites, Logan, UT, 2007.

[34] T. K. Imken, T. H. Stevenson, and E. G. Lightsey, "Design and Testing of a Cold Gas Thruster for an Interplanetary CubeSat Mission", Journal of Small Satellites, vol. 4, no. 2, pp. 371–386, 2015.

[35] B. Lewis, R. Hanel, S. Bhattacharya, A. J. Ricco, E. Agasid, D. Reiss-bubenheim, T. Straume, M. Parra, T. Boone, S. S. Maria, M. Tan, R. Bowman, M. Sorgenfrei, M. Nehrenz, M. Gandlin, T. Lusby, V. Kuroda, C. Pires, A. Rademacher, S. Wu, B. Klamm, C. Friedericks, C. Hake, B. G. Swan, E. Semones, S. Wheeler, C. M. Ott, S. Gavalas, and S. Castro, "SSC14-VII-3 BioSentinel : Monitoring DNA Damage Repair Beyond Low Earth Orbit on a 6U Nanosatellite", in 28th Annual AIAA/USU Conference on Small Satellites, Logan, UT, 2014, pp. 1–10.

[36] M. Sorgenfrei, T. Stevenson, and G. Lightsey, "Considerations for Operation of a Deep Space Nanosatellite Propulsion System", in

Proceedings of AAS Guidance, Navigation, and Control Conference, Breckenridge, Colorado, 2016.

[37] DuPont, "Thermodynamic Properties of DuPont Suva R-236fa", Wilmington, DE, Tech. Rep., 2005.

[38] B. Keramati and C. H. Wolgemuth, "Thermodynamic Properties of Liquid Sulfur Hexafluoride from 0 to 50 Â° C to 200 Bars", Journal of Chemical and Engineering Data, vol. 21, no. 4, pp. 423–428, 1976.

[39] NIST, Sulfur Hexafluoride, 2017.

[40] ——, Norflurane, 2017.

[41] ——, Butane, 2017.

[42] ——, Carbon Dioxide, 2017.

[43] BOC, "Ammonia R717", Tech. Rep., 2010.

[44] NIST, Nitrogen, 2017.

[45] 3D Systems Corporation, "Accura Bluestone", Rock Hill, SC, Tech. Rep., 2015, p. 1.

[46] The Lee Company, IEP Series Solenoid Valves, 2015.

[47] J. Anderson, "Quasi-One-Dimensional Flow: Nozzles", in Modern Compressible Flow: With Historical Perspectives, 3rd, New York: McGraw-Hill, 2002, ch. 5, pp. 202–218, ISBN: 0-07-242443-5.

[48] P. Hill and C. Peterson, Mechanics and Thermodynamics of Propulsion. Pearson, 1991.

[49] The Lee Company, "Lohm Laws", in Technical Hydraulic Handbook, 2009.

[50] T. Stevenson and G. Lightsey, "Design and Operation of a Thrust Test Stand for University Small Satellite Thrusters", in 2018 AIAA Aerospace Sciences Meeting, AIAA SciTech Forum, Kissimmee, Florida, 2018.

[51] A. Pancotti, T. Haag, S. King, and M. Walker, "Recommended Practices in Thrust Measurements", in 33rd International Electric Propulsion Conference, Fairview Park: Electric Rocket Propulsion Society, 2013, pp. 1–24.

[52] T. W. Haag, "PPT Thrust Stand", in 31st Joint Propulsion Conference, San Diego, CA, 1995.

[53] I. C-Flex Bearing Company, "Pivot Bearing Design Guide", Frankfort, NY, Tech. Rep., 2016.

[54] T. Stevenson and G. Lightsey, "Design and Characterization of a 3D-Printed Attitude Control Thruster for an Interplanetary 6U CubeSat", in 30th Annual AIAA/USU Conference on Small Satellites, Logan, UT, 2016.

[55] Vacco Industries, "VACCO Micro Propulsion Systems", El Monte, CA, Tech. Rep., 2014, pp. 1–4.

[56] B. W. Risi, "Propulsion System Development for the CanX-4 and CanX-5 Dual Nanosatellite Formation Flying Mission", PhD thesis, University of Toronto, 2014.

[57] GomSpace, "NanoProp 6U", Aalborg, Denmark, Tech. Rep., 2017.

[58] NASA, AERCam Sprint, 2003.

[59] C. Lorenzen, M. Stich, and S. K. Robinson, "Low-Risk Spacecraft-Inspection CubeSat", in 30th Annual AIAA/USU Conference on Small Satellites (Poster), Logan, UT, 2016.

[60] Ames Research Center, "Cubesat Proximity Operations Demonstration", NASA, Moffett Field, CA, Tech. Rep., 2018, pp. 3–4.

[61] J. Pei, L. Murchison, A. Benshabat, V. Stewart, J. Rosenthal, M. Banchy, D. Sellers, R. Elandt, D. S. Elliott, and A. Weber, "Autonomous Rendezvous and Docking of Two 3U Cubesats Using a Novel Permanent-Magnet Docking Mechanism", in 54th AIAA Aerospace Sciences Meeting, San Diego, CA, 2016, pp. 1–14.

[62] K. P. Doyle and M. A. Peck, "Safe, Failure-Tolerant CubeSat Docking Using Passive Magnetic Mechanisms", in 55th AIAA Aerospace Sciences Meeting, Grapevine, TX, 2017, pp. 1–24.

[63] K Kempen, L Thijs, J. V. Humbeeck, and J Kruth, "Mechanical properties of AlSi10Mg produced by Selective Laser Melting", Physics Procedia, vol. 39, pp. 439–446, 2012.

[64] Marshall Space Flight Center, "STANDARD FOR ADDITIVELY MANUFACTURED SPACEFLIGHT HARDWARE BY LASER POWDER BED FUSION", Huntsville, AL, Tech. Rep., 2017.

[65] D. C. Wof and D. K. Geller, "Relative Angles-Only Navigation and Pose Estimation for Autonomous Orbital Rendezvous", Journal of Guidance, Control, and Dynamics, vol. 30, no. 5, 2007.

[66] S. Sharma, C. Beierle, and S. D. Amico, "Pose Estimation for Non-Cooperative Spacecraft Rendezvous Using Convolutional Neural Networks", in 2018 IEEE Aerospace Conference, Big Sky, Montana, 2018, ISBN: 9781538620144.

[67] D Sinclair, "Picosatellite Reaction Wheels (RW-0.01)", Tech. Rep., 2017, pp. 0–1.

[68] B Marty, K Altwegg, H Balsiger, A Bieler, C Briois, U Calmonte, M Combi, J. D. Keyser, B Fiethe, S. A. Fuselier, S Gasc, T. I. Gombosi, K. C. Hansen, E Kopp, A Korth, L. L. Roy, U Mall, O Mousis, T Owen, M Rubin, J. H. Waite, and P Wurz, "Xenon isotopes in 67P/Churyumov- Gerasimenko show that comets contributed to Earths atmosphere", Science, no. June, pp. 1069–1072, 2017.

[69] B. Bienstock, M. Darrach, S. Madzunkov, and C. Sotin, "Cupids Arrow : An Innovative Nanosat to Sample Venus Upper Atmosphere", in 2016 IEEE Aerospace Conference, Big Sky, Montana, 2016.

[70] S. Smrekar, S. Hensley, M. S. Wallace, M. E. Lisano, M. R. Darrach, C. Sotin, D. Lehman, and M. D. Dyar, "Venus Origins Explorer (VOX) Concept : A Proposed New Frontiers Mission", in 2018 IEEE Aerospace Conference, Big Sky, Montana, 2018.

[71] A Mahieux, A. C. Vandaele, S Robert, V Wilquet, R Drummond, F Montmessin, and J. L. Bertaux, "Densities and temperatures in the Venus mesosphere and lower thermosphere retrieved from SOIR on board Venus Express : Carbon dioxide measurements at the Venus terminator", Journal of Geophysical Research, vol. 117, pp. 1–15, 2012.

[72] H. K. Tran, C. E. Johnson, D. J. Rasky, F. C. L. Hui, M.-T. Hsu, and Y. K. Chen, "Phenolic Impregnated Carbon Ablators (PICA) for Discovery class missions", in 31st AIAA Thermophysics Conference, New Orleans, Louisiana, 1996.

[73] D. Fryer and J. Harvey, High Pressure Vessels, 1st. Springer US, 1998, p. 216.

[74] NIST, Titanium, 2017.